POLITECNICO DI TORINO
Repository ISTITUZIONALE

Ion acceleration driven by intense laser pulses

Original
Ion acceleration driven by intense laser pulses / Boella, Elisabetta. - (2014).

Availability:
This version is available at: 11583/2560337 since:

Publisher:
Politecnico di Torino

Published
DOI:10.6092/polito/porto/2560337

Terms of use:
openAccess

This article is made available under terms and conditions as specified in the corresponding bibliographic description in the repository

Publisher copyright

(Article begins on next page)

04 August 2020

POLITECNICO DI TORINO

INSTITUTO SUPERIOR TÉCNICO
UNIVERSIDADE DE LISBOA

Ph.D. in Energetics

Ion acceleration driven by intense laser pulses

Elisabetta BOELLA

Advisors
Prof. Gianni COPPA
Prof. Luís SILVA

Presidents of the PhD program
Prof. Roberto ZANINO
Prof. Vitor VIEIRA

May 2014

Abstract

Laser pulses incident on plasma targets are capable of exciting very intense accelerating fields, that allow the acceleration of ions to high energies in very short distances. This is why a lot of interest has been developed on the topic of laser-driven ion acceleration over the past twenty years. Such a compact and affordable ion source would have many potential applications in physics and medicine, but several requirements are still far from being fulfilled.

In this thesis two mechanisms of ion acceleration are investigated: shock wave acceleration and Coulomb explosion.

Ultraintense lasers shot on plasma targets are capable of driving strong electrostatic shock waves that accelerate the plasma ions to high energies with a narrow energy spectrum. In the present work, the mechanism of shock formation and propagation in near-critical density plasmas is studied in detail. An idealized scenario where shock waves arise from the interpenetration of plasma slabs is studied. A theoretical kinetic model is derived and compared with simulation results. The conditions to accelerate ions to high energies with low energy spread are derived. The role of the laser in exciting shock waves is analyzed. The factors leading to high energy ion beams with narrow energy spectrum obtained in the simpler configuration are verified in this more complex and realistic scenario. A scaling for the ion energy with the pulse intensity is inferred for the ideal case of a plane wave and for a more realistic case of a finite size laser spot.

The second mechanism of ion acceleration that has been considered is the Coulomb explosion of pure ion nanoplasmas, an important subject in the field of laser-cluster interaction. In this thesis, a detailed study of Coulomb explosion in hetero-nuclear clusters consisting of different atomic species is carried out. Numerical results indicate that, in the presence of different ion species, lighter ions are accelerated in a quasi-monoenergetic way, in contrast with the well known results on Coulomb explosion of clusters composed by a single ion species, where the energy spectrum is much broader. A study on the formation of shock shells, nonlinear structures that arises during Coulomb explosion of homo-clusters when the initial density exhibits radial non-uniformity, is also presented. The analysis is carried out comparing N-body simulation results, that represent the exact solution since no approximations have been made, to the collisionless kinetic theory. The study shows that there are consistent differences between the real dynamics and the model based on the Vlasov-Poisson equations.

Keywords:
Plasma-Based Accelerators; Electrostatic shock waves; Coulomb explosion.

CONTENTS

1 Introduction **1**
  1.1 Target Normal Sheath Acceleration 2
  1.2 Radiation Pressure Acceleration 3
    1.2.1 Thick target: hole boring regime 4
    1.2.2 Thin target: light sail regime 4
  1.3 Breakout afterburner 5
  1.4 Shock wave acceleration 6
  1.5 Coulomb explosion 7
  1.6 Laser driven ion acceleration: overview 8
  1.7 Current and future applications 8
    1.7.1 Proton radiography 10
    1.7.2 Production of warm dense matter 11
    1.7.3 Fast ignition of fusion targets 12
    1.7.4 Biomedical applications 13
  1.8 Original contributions 14

2 Numerical methods for shock wave acceleration and Coulomb explosion **17**
  2.1 Particle In Cell technique 17
    2.1.1 Osiris framework 20
  2.2 Shell model 22
    2.2.1 Spherical geometry 24
    2.2.2 Plane geometry 24

2.2.3 Implementation details 25
2.3 N-body simulation technique 26
2.3.1 Implementation details 27

I Ion Shock Wave Acceleration 29

3 Theory of Electrostatic shock waves 31
3.1 Ion Acoustic Soliton 31
3.2 Solitary solution considering electron distribution functions . . 36
3.2.1 Classical theory 36
3.2.2 Relativistic theory 39
3.2.3 Mach number 41
3.3 Ion acoustic shock wave 45

4 Electrostatic shock formation and ion acceleration in plasmas 49
4.1 Shock formation and ion reflection in infinite plasma slabs . . . 50
4.2 Shock formation and ion reflection in finite plasmas 54
4.3 Shock formation and ion reflection in multilayer plasmas 59

5 Laser-driven electrostatic shocks 63
5.1 Shock formation and ion reflection in laser-plasma interaction . 64
5.1.1 Target decaying length impact on laser-driven ion shock wave acceleration 65
5.1.2 Laser polarization impact on laser-driven ion shock wave acceleration 68
5.1.3 Electron heating and ion energy scalings with a_0 70

II Ion acceleration in Coulomb explosion 75

6 Coulomb explosion of hetero-nuclear clusters 77
6.1 Coulomb explosion of a cluster composed by two ion species . . 78
6.1.1 Shell model simulations 78

6.1.2 Analytical model 81
6.2 Coulomb explosion of a cluster composed by three ion species . 88

7 N-body simulations of shock shells in Coulomb explosion 91
7.1 Theoretical model 92
7.2 Kinetic simulations of shock shell formation 94
7.3 N-body simulations of shock shell formation 96

8 Conclusions 101

Bibliography 104

LIST OF FIGURES

1.1 Laser driven ion acceleration: possible regimes 2
1.2 Schematic description of target normal sheath acceleration . . . 3
1.3 Schematic description of radiation pressure acceleration 4
1.4 Schematic description of the light sail regime 5
1.5 Relative dose versus radiation range in water 9
1.6 Proton radiography: general setup for laser-plasma experiments 11

2.1 Relation between Vlasov and a macro-particle approach 19
2.2 Typical Particle In Cell loop 21
2.3 Shell model (sketch) 23
2.4 Shell algorithm loop 23
2.5 Shell model for spherical geometry: from 3D to 2D 25

3.1 Soliton wave (sketch) 32
3.2 Soliton Sagdeev potential 34
3.3 Soliton maximum and minimum Mach number 35
3.4 Electrostatic shock (sketch) 36
3.5 Upstream and downstream electron distribution function 39
3.6 Sagdeev potential considering different electron temperatures . 41
3.7 Maximum Mach number versus density ratio 42
3.8 Different types of Sagdeev potential 43
3.9 Minimum and maximum Mach number: comparison between approximated and exact solution 44
3.10 Sagdeev potential due to ion reflection 46

3.11 Shock and soliton electrostatic potential 47
3.12 Electron and ion phase space in the shock wave 47
3.13 Ion and electron density 48

4.1 Shock formation and ion reflection in the interaction between two semi-infinite plasma slabs 51
4.2 Shock position versus time 51
4.3 Infinite plasma slabs interaction: ion phase space for different Γ 52
4.4 Infinite plasma slabs interaction: ion phase space for different v_{d1} 53
4.5 M_{max} versus Γ 54
4.6 Sharp transition plasma-vacuum: initial density and electric field 55
4.7 Smooth transition plasma-vacuum: initial density and electric field 55
4.8 Ion phase space: comparison between abrupt plasma-vacuum transition and exponentially decaying profile 56
4.9 Upstream ion distribution function: comparison between abrupt plasma-vacuum transition and exponentially decaying profile . 56
4.10 Upstream ion energy spread and percentage of reflected upstream ions versus L_g at different times 58
4.11 Shock speed versus time for different L_g 59
4.12 Upstream ion energy spread and percentage of reflected upstream ions versus L_g for different initial electron temperatures 60
4.13 Multilayer plasma (sketch) 60
4.14 Multi-layer plasmas: ion phase space 61
4.15 Multi-layer plasmas: ion distribution 62

5.1 Shock formation and ion reflection driven by an intense laser pulse 66
5.2 Laser-driven electrostatic shock: electron distribution function and ion energy spectrum 67
5.3 Shock speed 67
5.4 Ion phase space for different L_g 69
5.5 Laser polarization: electron distribution function and ion energy distribution 69

5.6 Electron temperature and ion energy versus a_0 71
5.7 Laser plasma interaction region 72
5.8 Ion phase space due to a shock wave driven by a finite spot size laser 72
5.9 Electron temperature scaling with a_0 for a finite spot size laser . 73
5.10 Ion energy scaling with a_0 for a finite spot size laser 73

6.1 Density and phase space due to Coulomb explosion 79
6.2 Radial electric field due to Coulomb explosion 80
6.3 Ion energy spectrum due to Coulomb explosion 80
6.4 Radial electric field and Hydrogen phase space and energy spectrum for different values of $\alpha = N_H/N_0$ 81
6.5 Hydrogen energy spread, percentage of monoenergetic ions, average energy and maximum energy versus α 82
6.6 Radial electric field and Hydrogen phase space and energy spectrum for different ionization levels of the heavy species 82
6.7 Hydrogen energy spread for different ionization levels of the heavy species 83
6.8 Concentric spheres of the heavy and light ions (sketch) 83
6.9 Light and heavy ions frontline versus time 86
6.10 Coulomb explosion of a multi-species cluster: density and phase space evolution 87
6.11 Coulomb explosion of a multi-species cluster: electric field evolution 88
6.12 Coulomb explosion of a multi-species cluster: energy spectrum evolution 88

7.1 Shock shells in CE: density and phase space evolution (non collisional model) 95
7.2 Kinetic simulations of shock shells: numerical comparison . . . 96
7.3 Schematic description of the calculation of ensemble averages according to classical statistical mechanics 97
7.4 Coulomb explosion: density and phase space evolution (N-body simulation) 98

7.5 Coulomb explosion phase space: ensemble average and single calculations 98
7.6 Shock shells in Coulomb explosion: density and phase space evolution (N-body simulation) 99
7.7 Standard deviation of the peak of the ion density 99

LIST OF TABLES

1.1 Summary of the features of some laser driven ion acceleration mechanisms. 9

CHAPTER 1

INTRODUCTION

Nowadays, ion acceleration driven by super intense laser pulses is a vivid field of investigation, attracting an impressive and steadily increasing research interest. Intense laser pulses shined on plasma targets are capable of exciting very strong electric and magnetic fields capable of accelerating ions to high energies over very short distances (the acceleration gradients obtained in plasmas are $100-1000\,\mathrm{GeV/m}$, orders of magnitude higher than $10-100\,\mathrm{MeV/m}$ typical values of conventional accelerators), allowing for what is normally referred to as a table-top ion accelerator [1]. Such compact and affordable high energy ion sources would have many possible potential applications in science and medicine, which have been limited until now by the cost, the size and the technological issues connected to conventional accelerator devices. However, despite of these incredible features, there are still several difficulties that need to be addressed and overcome (such as increasing the particle energy, spectral and angular control of the beam, conversion efficiency from laser energy into the ion beam, stability of the acceleration parameters, etc.) in order to consider laser driven ion acceleration a mature technology. This has motivated a significant theoretical, numerical and experimental effort devoted to understand and optimize the physics behind the process of ion acceleration.

The continuous progress in high-power laser technology and in target manufacturing and engineering has been leading to the proposal and demonstration of different acceleration mechanisms. Figure 1.1 shows the most common regimes depending on the pulse duration and intensity. It is worth noticing that these two parameters are important, but these are not the only param-

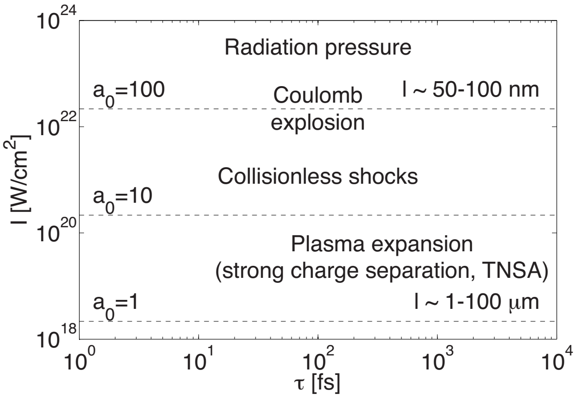

FIGURE 1.1: Ion acceleration mechanisms depending on laser duration and intensity. Values of the normalized vector potential a_0 have been computed considering a pulse with wavelength $\lambda_0 = 800\,\mathrm{nm}$. Adapted from [2].

eters that determine the prevailing acceleration process and also that there is no a real sharp separation between the different occurring scenarios. The first part of this chapter provides an overview over some of the most studied laser driven acceleration mechanisms, i.e. target normal sheath acceleration, radiation pressure acceleration and break out after burner acceleration. The concepts of shock wave acceleration and Coulomb explosion, subjects of this thesis work, are then introduced. Afterwards, a comparison among the different processes is also reported. Some possible applications for laser accelerated ions are then illustrated.

1.1 TARGET NORMAL SHEATH ACCELERATION

When a linearly polarized laser pulse with intensity $I > 10^{18}\,\mathrm{W/cm^2}$ and normalized vector potential $a_0 = 8.5 \times 10^{-10}\sqrt{I_{[\mathrm{W/cm^2}]}\lambda^2_{[\mu\mathrm{m}]}} \geq 1$ is incident into a several microns thick solid target ($L_{target} > 1\,\mu\mathrm{m}$), the laser pre-pulse ionizes the front side of the target forming an expanding plasma. When the main pulse reaches the target, it is partially absorbed at the plasma critical density (i.e. density at which laser and plasma frequencies are the same), heating up the surface electrons to temperatures of several MeV. Hot electrons recirculate inside the target and eventually leave it at the back surface, creating a strong charge separation electric field directed along the normal to the surface.

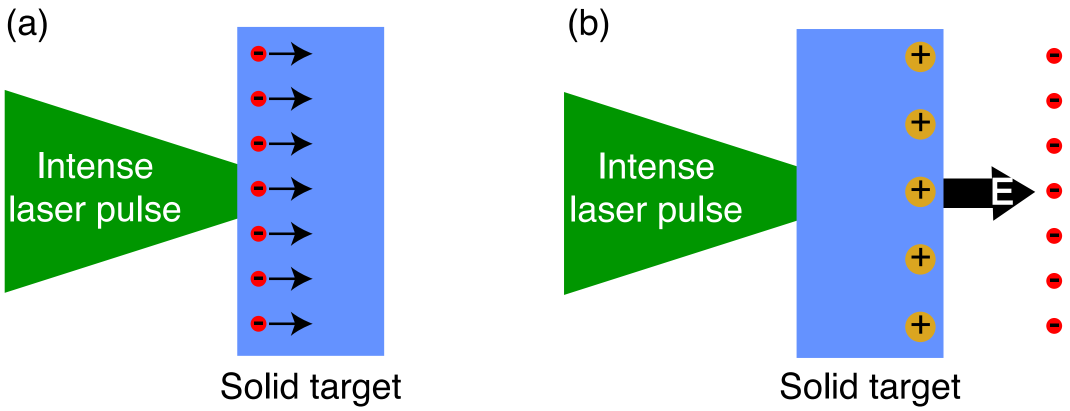

FIGURE 1.2: Schematic description of target normal sheath acceleration. The intense laser pulse heats the electrons on the front side of the target (a). The hot electrons penetrate the target and leave it at the back surface creating a sheath field that accelerates ions to several MeVs (b).

As a consequence of the sheath field, ions are accelerated perpendicularly to the surface (see figure 1.2), via a mechanism called Target Normal Sheath Acceleration (TNSA) [3, 4]. The acceleration is most effective on protons, always present in solid targets in the form of impurities. Heavier positive ions with more inertia contribute in creating the charge separation field and are only accelerated on longer time scales, when the proton charge is not enough to balance the escaping hot electrons. The ion energy spectrum is usually broad (the energy spread $\Delta\varepsilon/\varepsilon$ is about 100%) with a sharp cutoff at a maximum energy, representing a limitation for applications requiring a monoenergetic beam [5]. The highest proton energy measured in TNSA experiments has been 70 MeV [4].

1.2 RADIATION PRESSURE ACCELERATION

When the laser intensity increases up to $10^{20}\,\mathrm{W/cm^2}$, a different acceleration mechanism starts to dominate over TNSA. It is the so called Radiation Pressure Acceleration (RPA) regime (figure 1.3). It is strictly connected with the pressure that an electromagnetic wave exercises over a nontransparent medium. Depending on the thickness of the target, two different scenarios can take place: hole boring, if the target is thick and light sail, if the target is

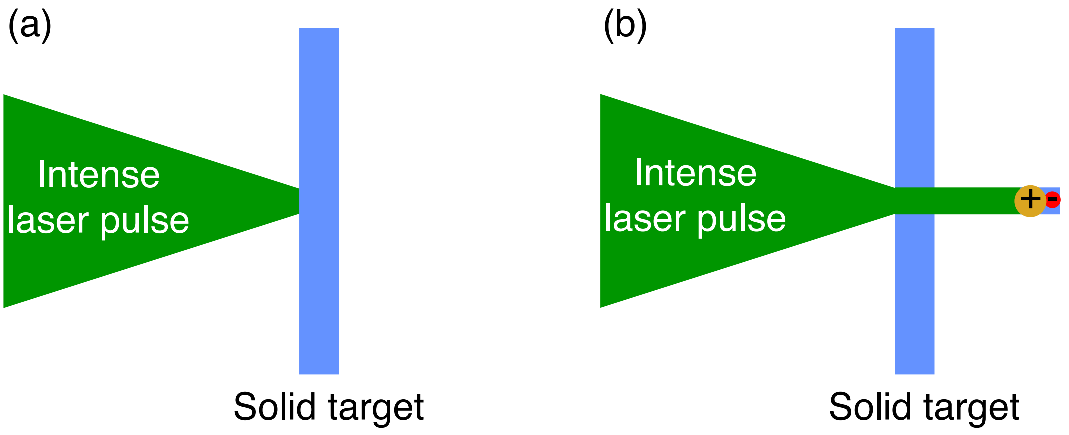

FIGURE 1.3: Schematic description of radiation pressure acceleration.

thin.

1.2.1 THICK TARGET: HOLE BORING REGIME

The intense radiation pressure of the laser pushes the surface electrons of an overdense plasma inside the target. Since, in this early phase, the ions are immobile, a positively charged region, in which the electron density is depleted, and a cloud of compressed electrons are formed. The charge imbalance gives rise to a quasistatic field, with a peak located at the border between the depletion and the compression area. The field accelerates the ions, that cross the compressed electron region and pile up at the end of it producing a sharp density spike and causing the hydrodynamical collapse of the electron equilibrium. This process leads to the production of a narrow bunch of fast ions which penetrates further into the plasma bulk. Eventually, the quasiequilibrium is restored again and the process keeps on repeating as long as the laser is turned on [6,7].

1.2.2 THIN TARGET: LIGHT SAIL REGIME

When the target is thin ($\sim$ plasma skin depth), the situation changes. All the ions get accelerated before the end of the laser pulse. They cannot pile up to a singular density because they constitute practically the whole target. The laser pulse can then push the electrons further and the acceleration stage is

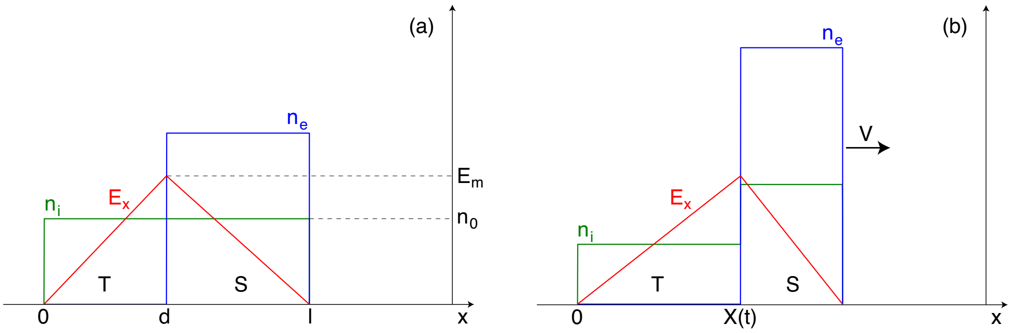

FIGURE 1.4: Schematic description of the light sail regime. Ion (green) and electron (blue) density profiles and electric field (red) are shown. (a) Electrons have piled up in the "sail" region S ($d < x < l$) leaving behind a depleted area called "tail" region ($0 < x < d$). The ion density is still unperturbed. (b) At later times ions move under their own space charge field towards S and their density in T decreases. Ions in S ($x > X(t)$) gets accelerated and move with electrons at velocity V. Adapted from [9].

repeated. Since the target is thin, ion motion is strictly bound to the electrons and the target behaves as a rigid object [8] (see figure 1.4). Ion acceleration is more efficient in this case because ions are not screened by the background plasma, as they would be in the hole boring regime.

After this scheme was proposed by Esirkepov *et al.* [8], it has been realized that a similar regime could be accessed using less intense circularly polarized laser pulses. The use of a circular polarized laser inhibits the $\mathbf{j} \times \mathbf{B}$ heating mechanism [10], because the electric field component perpendicular to the target surface is absent. This avoids that the thin target heats up and starts to expand becoming underdense and therefore transparent to the laser. Since the heating is suppressed, the target preserves its non-transparency; the energy of the laser is largely reflected and the pulse acts like a piston driven by the pressure of the radiation [11, 12].

1.3 BREAKOUT AFTERBURNER

When ultrathin foils are used as targets and the intensity of the laser is smaller than in the RPA case, the foil expands, becoming progressively transparent to the laser during the short-pulse interaction. Another mechanism of ion acceleration is excited at this point, called breakout afterburner (BOA) [13]. The electron heating is enhanced as the target becomes transparent. Electrons reach relativistic temperatures and create a strong field that accelerates the ions in a solitary bunch. The high drift between electrons and ions triggers the relativistic Buneman instability [14, 15]. The phase speed of the instability is resonant with the ion speed, benefiting ion acceleration.

1.4 SHOCK WAVE ACCELERATION

Particle acceleration by shock waves is a problem of great interest for astrophysics [16]. The existence of an ion component reflected by the shock front is a fundamental prerequisite in the basic fluid theory of collisionless electrostatic shocks [17]. In the frame moving at the shock speed, ions are reflected by the shock when their kinetic energy is higher than the potential energy associated to the wave. Ions, initially at rest, are then accelerated to velocities up to twice the shock speed.

Shock wave acceleration was proposed as a mechanism of ion acceleration by Denavit [18] and Silva *et al.* [19]. In these previous works, the conditions under which shocks are generated in solid targets were studied. The use of an ultra-intense laser ($I \geq 10^{20}\,\mathrm{W/cm^2}$) is required in order to achieve an efficient electron heating. Moreover, in these simulations the narrow energy spectrum of the ions is smeared out by the strong charge separation field at the back of the target.

Recently, electrostatic shocks have been identified as the physical phenomenon responsible for the acceleration of monoenergetic ions ($\varepsilon \simeq 20\,\mathrm{MeV}$ and $\Delta\varepsilon/\varepsilon \simeq 1\%$) in the interaction between a CO_2 laser pulse of moderate intensity ($I \simeq 10^{16}\,\mathrm{W/cm^2}$) and a hydrogen gas jet [20]. The experimental work motivated the theoretical and numerical study on shock wave acceleration presented in this thesis. In fact, despite of the great experimental results, several aspects regarding the physics of shock generation in plasmas still need to be addressed. Moreover, optimal conditions to obtain ion beams suitable for practical applications has to be fully understood. Therefore, theoretical and numerical studies have been carried out in order to obtain a deeper insight of the physics of shock waves in plasmas. In particular, the existing theoretical model on electrostatic shocks [21] has been generalized to include relativistic electron temperatures and ion reflection; calculations are shown in chapter 3. Numerical simulations carried out with particle-based codes presented in detail in chapter 2 have been performed. An idealized scenario where shock waves arise in the interaction between plasmas with different characteristics has been examined in chapter 4. After the analysis of this configuration, that despite of its simplicity allowed for identifying some optimal conditions for shock formation and ion acceleration, the role of the laser in driving the shock has been studied and results are presented in chapter 5. Numerical simulations indicate that high-quality proton beams required for practical applications can be obtained with existing laser systems.

1.5 COULOMB EXPLOSION

Coulomb explosion of pure ion nanoplasmas is an important problem in the field of ultra intense laser-cluster interaction with relevance for plasma physics, fusion research [22, 23] and imaging by “diffraction before destruction” [24].

Clusters are aggregates of atoms or molecules. They are formed in the supersonic expansion of a gas through a conical nozzle. During the adiabatic expansion, the gas vapor cools down and the gas enters in a supersaturated state. At this point gas particle collisions, present during the whole process, lead to the formation of dimers that work as nucleation sites for the clusters [25].

A great interest developed during the past years around the topic of laser-cluster interaction. The main motivation is represented by the efficient coupling between cluster media and laser radiation. Nearly 100% of the total laser energy is deposited within a few millimeters propagation length [26]. This can be explained observing that clustered targets combine gas and solid target features. The laser pulse propagates through the medium (clusters are usually sparse in a gas jet) strongly interacting with the individual clusters, which can be seen as solid targets with extremely high surface-to-volume ratios [27]. The high energy absorption results in different experimental evidences, such as bright x-ray emission [28,29], production of highly ionized matters [30] and generation of energetic electrons and ions [31–33] . The acceleration of ions due to Coulomb explosion of small clusters is the phenomenon analyzed in the second part of this thesis.

Depending on the laser and cluster parameters, several scenarios can take place. Coulomb explosion occurs when all the cluster electrons are instantaneously swept away by the laser pulse, leaving behind a pure positive ion cloud, that undergoes a violent explosion driven by the Coulomb repulsive forces.

In chapter 6 the ion dynamics in the explosion of hetero-nuclear clusters (i.e. clusters composed of different atom species) is studied. Numerical results obtained by using the shell model (see chapter 2) are presented; simulations indicate that, in the presence of different ion species, lighter ions are accelerated in a quasi-monoenergetic way, in contrast with the well known results about Coulomb explosion of clusters composed by single ion species, where the energy spectrum is much wider. A theoretical model, useful for a deep comprehension of the explosion dynamics, has been developed for the case of a two-species pure ion spherical plasma; results of the theoretical model have been compared with numerical simulations showing a perfect agreement. In chapter 7, the formation of shock shells during the explosion of small clusters is examined. In particular, a rigorous analysis carried out using the N-body simulation method, whose details are described in chapter 2, is presented. Results are then compared with reference solutions for the collisionless kinetic equations, normally utilized to study these phenomena, showing that kinetic models based on the Vlasov-Maxwell system of equations fail when attempting to capture the physics of shock shells formation. Direct interactions between particles are not negligible and therefore the mean field theory of the collisionless model does not provide the correct results.

1.6 LASER DRIVEN ION ACCELERATION: OVERVIEW

As seen in the previous sections, depending on the laser and target characteristics, several ion acceleration mechanisms can be excited. Table 1.1 reports a brief summary of the laser and target requirements necessary to excite each physical processes previously described. The features of the accelerated ions are also shown.

1.7 CURRENT AND FUTURE APPLICATIONS

One of the most peculiar features of MeV protons is the energy deposition profile in dense matter: being the energy loss for ions dominated by Coulomb

		TNSA	BOA	RPA	SWA	CE
Laser	I [W/cm^2]	10^{18}	5×10^{19}	$10^{20} - 10^{22}$	10^{16}	$10^{15} - 10^{22}$
	λ [μm]	1	1	0.8	10	1
	a_0	1	6	8	$1.5 - 2.5$	1
	contrast	10^{-7}	10^{-8}	10^{-10}	10^{-5}	-
Target	L_{target} [nm]	$10^3 - 10^5$	100	1-50	gas jet	cluster
Ion	ε_{max} [MeV]	~ 70	> 100	< 5	> 22	1
	$\Delta\varepsilon/\varepsilon$ [%]	100	100	10-20	≤ 10	100

TABLE 1.1: Summary of the features of some laser driven ion acceleration mechanisms.

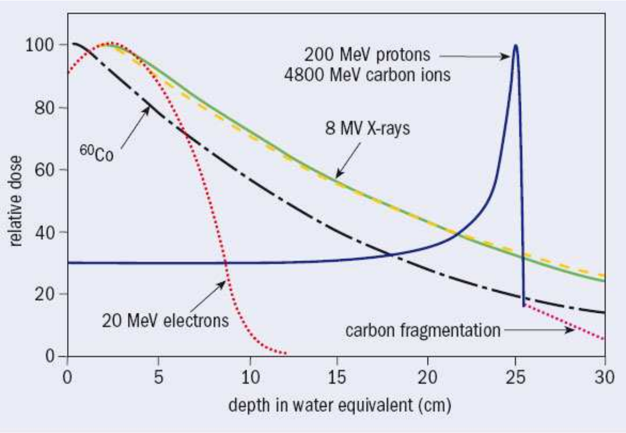

FIGURE 1.5: Dose deposited in water versus radiation range. While x-ray and electrons release most of their energy at the beginning of their path, hadrons do it at the end of their path in a very localized area, the Bragg peak. From [35].

collisions with higher cross-section at lower energies, most of the particles energy is released at the end of their path in what is called the Bragg peak [34]. The possibility of delivering energy in a very localized region makes positively charged ions very interesting for applications like cancer therapy, isotope generation for medical applications, production and probe of "warm dense matter", fast ignition of fusion targets and injectors for conventional ion accelerators. These current and future applications are illustrated in details in the next paragraphs.

1.7.1 PROTON RADIOGRAPHY

Proton radiography has been proposed in the late 1960s as an alternative to the traditional x-ray radiography. In 1968, Koehler demonstrated that proton radiographic films could be produced with high image contrast, as long as the proton range was equal to the thickness of the object to image [36].

Proton beams generated via laser-matter interaction show properties in term of spatial resolution and temporal duration that make them perfect for proton probing [37].

The most successful applications to date of proton probing are related to the detection of electric and magnetic fields in plasmas [38, 39]. The high temporal resolution is fundamental to monitor highly transient fields following short-pulse interaction. Moreover the proton probing technique has been successfully used to get detailed information on nonlinear phenomena occurring in laser-plasma interaction experiments [40, 41].

In a general laser-plasma experiment (figure 1.6), a short and intense laser pulse is focused on a thin solid foil in order to generate and accelerate an energetic and collimated proton beam with temporal duration comparable to the laser pulse duration. The protons propagate then through the region of the experiment, where a second laser is directed onto a target. Crossing this region, protons get deflected due to the fields in the plasma. Since the beam is laminar, the proton source can be viewed as a point-like virtual source and the geometrical magnification parameter M at the detector can be computed as

$$M = \frac{L + l + l_s}{l + l_s} \simeq \frac{L}{l} \tag{1.1}$$

where L is the distance between the interaction target and the detector, $l \ll L$ is the distance between the foil and the interaction target, and $l_s \ll l$ is the distance between the virtual source and the foil. Finally, the proton beam coming out from the interaction region is recorded on a spectrally resolved detector [42]. The broad energy spectrum of a TNSA produced proton beam has a time-energy correlation that allows for taking a movie of the examined interaction. Protons with different energies penetrate up to different depths in the stack camera and, releasing most of their energy in correspondence with the Bragg peak, give a different volumetric signal deposition. All the different frames taken in a single shot can then be merged to get temporal information about the interaction evolution. The minimum spatial resolution is determined

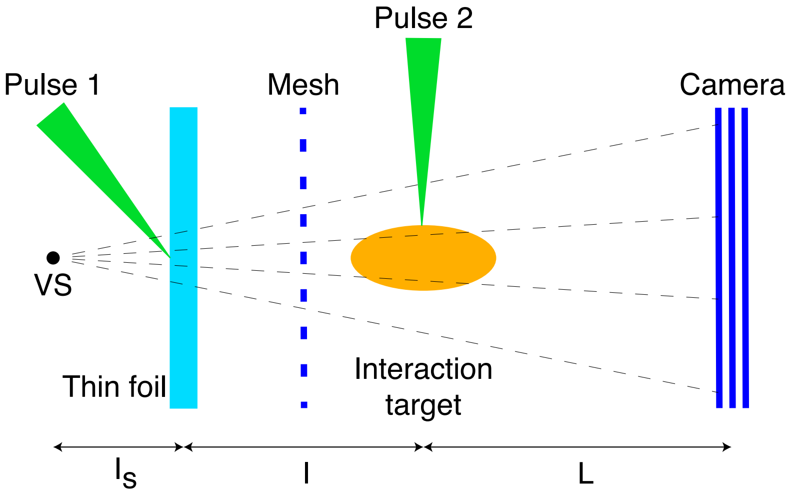

FIGURE 1.6: Proton probing technique general setup. Adapted from [42].

by the transverse size of the virtual source, allowing for resolving details of μm size [7].

1.7.2 PRODUCTION OF WARM DENSE MATTER

Warm dense matter (WDM) is an extreme state of matter in a regime of density between 1 and 10 times the solid density and temperature up to 100 eV [43]. The material is in a state between solid and plasma: it is too dense to be described by weakly coupled plasma physics, but too hot to be described by condensed matter physics. Studying these conditions is relevant in the fields of material science, geophysics and planetary science [44–47].

In order to understand the properties (equation of state and opacity) of WDM, it is necessary to heat up in a uniform way a large volume of solid density material. Therefore, ions, that can heat the material in depth, are suited for this purpose. Other methods involve x-rays heating and shock compression, but they are less effective in heating the sample uniformly.

Ion beams for this scope can be produced by conventional accelerators or by electrical-pulsed ion sources. However, ion pulses from these sources will have a long duration and will cause the materials to expand hydrodynamically before the right temperature is reached. On the other hand, laser-generated proton pulses have a shorter duration and can rapidly heat the sample before its expansion. Hence, the target stays at near solid density for a sufficient time to investigate its properties [48].

1.7.3 FAST IGNITION OF FUSION TARGETS

According to the traditional scheme to achieve inertial confinement fusion (ICF), the so called direct drive, laser pulses are used to compress to high densities ($\geq 10^{25}$ particles/cm^3) and heat to high temperatures ($\simeq 10\,\mathrm{keV}$) at the same time the central hot spot of a Deuterium-Tritium pellet. Ignition occurs following pulse compression. After the ignition has been achieved, a thermonuclear burning wave quickly propagates through the target leading to the generation of a large amount of energy from the fusion chain reaction [49]. However, in order to reach ignition and obtain energy gain, a high degree of symmetry in the explosion is required. Moreover, several hydrodynamics instabilities can play a role in preventing the success of the experiment.

For these reasons, other approaches, called indirect drive, have been proposed. In particular, referring to the fast ignition scheme, the fuel compression phase is separated from the ignition stage. The first one is reached with the use of several laser beams that ablate the target, creating an expansion wave toward the outward, responsible for the fuel compression by momentum conservation. After the fuel has been compressed, ignition is driven by a separate external trigger: a population of fast electrons generated by a second shorter and more intense laser pulse. Energetic electrons will be stopped through collisions at the core, heating and igniting the fuel [50]. However, also this approach presents some difficulties in the realization. In particular, since the energy deposition profile of electrons is a smooth function, producing a localized hot spot is very difficult.

On the other hand, protons are characterized by a highly localized energy deposition profile and offer a valid alternative as an ignitor beam. This approach has been proposed for the first time in [51], after the observation that multi-MeV protons could be produced in petawatt experiments [4]. Moreover, theoretical calculations showed that the wide energy spectrum of, for instance, TNSA produced ions and the temporal dispersion of the beam do not have a negative impact, but could actually benefit the core heating [52,53]. The proton stopping range increases with the plasma temperature. Therefore, heating due to the more energetic particles favors energy deposition by the less energetic ones, that arrive later in time.

1.7.4 BIOMEDICAL APPLICATIONS

HADRONTHERAPY

In hadrontherapy, protons or Carbon ions are used to irradiate cancer tumor cells [54, 55]. These particles present several advantages compared to the most commonly used x-rays. Irradiation of nearby healthy tissues is strongly reduced because the range for positive ions is fixed by their energy. Moreover, the well-localized Bragg peak leads to a substantial increase of the irradiation dose in the proximity of the stopping point. In order to be effective for therapeutical treatments, protons with energy between 60 and 250 MeV and Carbon ions with energy up to 400 MeV are necessary.

The use of laser-based accelerators, as alternative to conventional particle accelerators, was proposed by several authors [56–59] that pointed out its advantages in term of cost and compactness. Different schemes were suggested, from using laser-driven protons as high quality injectors in a rf accelerator [60] to all-optical systems [57], in which ion beam acceleration takes place in the treatment room itself and ion beam transport and delivery issues are thus minimized.

However, at current status, there are significant challenges before that laser-driven proton beams reach the therapeutic specifications. In particular, ion maximum energy, energy spectrum, repetition rate and reliability are still far from accomplishing the requirements [61].

MEDICAL DIAGNOSIS

Multi-MeV proton beams can induce nuclear reactions in low-Z materials. Therefore, laser-driven ion beams have been suggested for the production of short-lived positron emitting isotopes to employ in positron emission tomography (PET). The PET technique is used for medical imaging of blood flow and amino acid transport and for tumor detection. Up to now, the 20 MeV protons for PET have been produced by large size and costly cyclotrons. The possibility of using moderate energy, ultrashort, high-repetition tabletop lasers may lead in a near future to the production of short-lived isotopes via laser-driven proton beams. In order to reach an activity of about 1 GBq, necessary for PET, a laser system with energy 1 J, duration 30 fs, intensity 10^{20} W/cm^2 and kHz repetition rate is necessary [62, 63].

1.8 ORIGINAL CONTRIBUTIONS

In this thesis two different mechanisms of ion acceleration in laser-generated plasmas are investigated. The first part of the thesis is devoted to the study of shock wave acceleration in near critical density plasmas, while the second part deals with the study of ion acceleration in Coulomb explosion. The main original contributions of this work are as follows.

Chapter 2 is devoted to describe the numerical tools used to perform the simulations presented in the thesis. A simple model for the study of electrostatic collisionless plasma problems characterized by a high degree of symmetry has been developed. The electric field acting on each computational particle is evaluated by means of the Gauss law without the use of a spatial grid. The absence of the latter allows for a simple and light algorithm that can run on normal laptop or desktop machines in reasonable times providing extremely precise results that can represent a reference solution. Moreover, an algorithm to perform N-body simulations has been implemented in order to carry out statistical mechanics type of studies in systems characterized by few degree of freedom, as in the case of nanoplasmas generated via laser-cluster interaction.

In chapter 3, the theoretical model presented in [21] for the steady state Mach number of electrostatic shocks formed in the interaction of two plasma slabs of arbitrary density and temperature is generalized for relativistic electron and nonrelativistic ion temperatures. It is found that the relativistic correction leads to lower Mach numbers and as a consequence ions are reflected with lower energies. The steady state bulk velocity of the downstream population is introduced as an additional parameter to describe the transition between the minimum and maximum Mach numbers that is dependent on the initial density and temperature ratios. In order to transform the solitonlike solution in the upstream region into a shock, a population of reflected ions is considered and differences from a zero-ion temperature model are discussed.

In chapter 4, electrostatic shocks driven by the interaction of two plasma slabs with different density, temperature and/or drift velocity are studied with numerical simulations. It is shown that when the density jump between the two slabs is high enough, a shock wave capable of reflecting and accelerating the upstream ions is generated and that the percentage of reflected ions increases with the density ratio. It is demonstrated that a relative drift between the two slabs plays a similar role and an increase in the value of the drift velocity leads to an increment in the energy and in the number of reflected ions. Theoretical predictions about the shock critical Mach number (Mach number at which ion reflection occurs) are confirmed by numerical results. Moreover, when finite plasma slabs are considered, it has been seen that a TNSA field develops at the plasma-vacuum transition. This charge separation field, responsible to worsen the features of the reflected ion beams, can be controlled with a smooth transition between the plasma and the surrounding vacuum. Therefore tailored plasmas have been considered. Two possible configurations have been studied: in the first one the abrupt plasma-vacuum transition has been substituted with an exponentially decreasing density profile; in the second set up, several plasma slabs with progressively decreasing density mimicking the exponential profile have been used. Detailed parameter scans allowed to determine the optimal conditions to obtain quasi-monochromatic ion beams.

In chapter 5, the role of the laser in the formation of electrostatic shocks is analyzed. It is shown that the interaction of intense lasers with tailored near-critical density plasmas allows for the efficient heating of the plasma electrons and steepening of the plasma profile at the critical density interface, leading to the generation of high velocity shock structures and high energy ion beams. Scaling laws regarding the electron temperature and the ion energy have been retrieved for the ideal case of a plane wave laser and for the realistic case of a finite laser spot size.

Chapter 6 is dedicated to the study of Coulomb explosion in hetero-nuclear clusters. Numerical simulations show that in heavy-light systems, composed of two different ion species, the lighter ions get accelerated in a quasi-monoenergetic way, in contrast with the well known results about Coulomb explosion of clusters composed by single ion species, where the energy spectrum is much wider. A theoretical model has been derived and results have been compared with the numerical ones, showing an excellent agreement.

In chapter 7, the phenomenon of shock shell formation during the Coulomb explosion of small clusters is analyzed. N-body simulation results are presented and compared with the standard collisionless kinetic theory, showing consistent differences. This can be attributed to the fact that direct interactions among particles play a important role in these scenarios and therefore, the mean field theory of the collisionless kinetic model fails in describing the system dynamics.

The work developed in this Thesis resulted in the following scientific publications (either published or in preparation):

— F. Fiúza, A. Stockem, E. Boella, R. Fonseca, L. Silva, D. Haberberger, S. Tochitsky, C. Gong, W. Mori, and C. Joshi. ″Laser-driven shock acceleration of mono-energetic ion beams´´. *Physical Review Letters*, vol. 109, p. 215001, 2012.

— F. Fiúza, A. Stockem, E. Boella, R. Fonseca, L. Silva, D. Haberberger, S. Tochitsky, W. Mori, and C. Joshi. ″Ion acceleration from laser-driven electrostatic shocks´´. *Physics of Plasmas*, vol. 20, p. 056304, 2013.

— A. Stockem, E. Boella, F. Fiúza, and L. O. Silva. ″Relativistic generalization of formation and ion-reflection condition in electrostatic shocks´´. *Physical Review E*, vol. 87, p. 043116, 2013.

— A. Stockem, F. Fiúza, E. Boella, R. A. Fonseca, L. O. Silva, C. Joshi, and W. B. Mori. ″Theoretical studies of collisionless shocks for laser-acceleration of ions´´. *The proceedings of SPIE*, vol. 8779, p. 87790B, 2013.

— A. D'Angola, E. Boella, and G. Coppa. ″On the applicability of the collisionless kinetic theory to the study of nanoplasmas´´. Submitted to Physics of Plasmas, 2014.

— E. Boella and G. Coppa. ″Shell model: a simple gridless, particle-based technique for plasma simulation´´. To be submitted to Journal of Computational Physics, 2014.

— E. Boella, F. Fiúza, A. Stockem, and L. Silva. ″Shock wave acceleration: an optimization study´´. To be submitted to Physics of Plasmas, 2014.

— E. Boella, B. Peiretti Paradisi, A. D'Angola, G. Coppa and L. Silva. ″Quasi-monochromatic ions from Coulomb explosion of hetero-nuclear clusters´´. To be submitted to Physics of Plasmas, 2014.

CHAPTER 2

NUMERICAL METHODS FOR SHOCK WAVE ACCELERATION AND COULOMB EXPLOSION

Depending on the temporal and spatial scales involved in the problem of interest, different numerical techniques can be employed to simulate the physics of a plasma. This thesis focuses on the study of shock waves in collisionless plasmas and on Coulomb explosion, phenomena that involve non linear and kinetic processes. Therefore, particle methods are particularly suitable to tackle the physics of these phenomena. The study of shock wave acceleration has been carried out using Osiris [64, 65], a state-of-the-art particle in cell (PIC) code [66–68] and the shell model, a gridless particle-based kinetic algorithm [69]. Coulomb explosion results have been obtained employing the shell model and, when allowed by the size of the problem, solving directly Newton's equation, with an approach similar to the one adopted in molecular dynamics simulations [70]. This chapter will describe in detail the numerical schemes adopted.

2.1 PARTICLE IN CELL TECHNIQUE

The most general set of equations to describe a collisionless plasma (i.e. a plasma with $\nu/\omega_p \ll 1$, being ν the collision frequency and ω_p the plasma frequency and $\epsilon_p \gg 1$, being ϵ_p the plasma parameter, ratio between the plasma kinetic and potential energy) is the Maxwell-Vlasov system [71]:

$$\begin{cases} \dfrac{\partial f_j}{\partial t} &= -\mathbf{v}\cdot\dfrac{\partial f_j}{\partial \mathbf{x}} - q_j\left(\mathbf{E} + \dfrac{\mathbf{v}}{c}\times\mathbf{B}\right)\cdot\dfrac{\partial f_j}{\partial \mathbf{p}} \\ \nabla\cdot\mathbf{E} &= 4\pi\rho \\ \nabla\times\mathbf{E} &= -\dfrac{1}{c}\dfrac{\partial \mathbf{B}}{\partial t} \\ \nabla\times\mathbf{B} &= \dfrac{4\pi}{c}\mathbf{J} + \dfrac{1}{c}\dfrac{\partial \mathbf{E}}{\partial t} \\ \nabla\cdot\mathbf{B} &= 0 \end{cases} \tag{2.1}$$

where $f_j(\mathbf{x},\mathbf{p},t)$ is the distribution function of the species j, having mass m_j and charge q_j, $\mathbf{x} = (x, y, z)$ is the position, $\mathbf{v} = (v_x, v_y, v_z) = \mathbf{p}/m_j\gamma$ the velocity, $\mathbf{p}$ the momentum, $\gamma = \sqrt{1+\mathbf{p}^2/m_j^2c^2}$ the Lorentz factor, c the speed of light, $\mathbf{E}$ the electric field, $\mathbf{B}$ the magnetic field and ρ and $\mathbf{J}$ are the charge and current densities, defined as

$$\rho = \sum_j q_j \int f_j(\mathbf{x},\mathbf{p},t)\,\mathrm{d}\mathbf{p} \tag{2.2}$$

$$\mathbf{J} = \sum_j \frac{q_j}{m_j}\int \mathbf{p} f_j(\mathbf{x},\mathbf{v},t)\,\mathrm{d}\mathbf{p} \tag{2.3}$$

Since the distribution function is 6-dimensional, solving the system 2.1 represents a big task and it would require computational resources that are still not available. The problem can be overcome with a Lagrangian approach, using a particle method. As reported in [67], "Particle model is a generic term for the class of simulation models where the discrete representation of physical phenomena involves the use of interacting particles". However, the idea of directly simulating the interaction between the particles that compose a plasma is not feasible: in most cases (an exception will be shown in chapter 7), plasmas that one aims to simulate are composed by $10^{15} - 10^{20}$ particles. Since the number of computational operations scales with the number of particles (in the best case, it scales as $N_0 \log N_0$ [72], where N_0 is the number of particles), it is clear that this approach will not be practical. A solution can be found observing the nature of the system that one aims to simulate. Many systems of

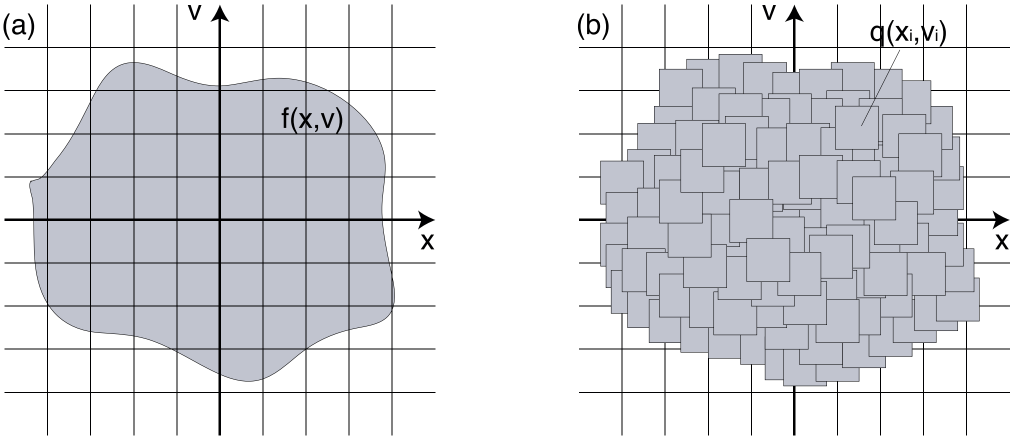

FIGURE 2.1: Relation between (a) Vlasov and (b) a macro-particle approach. Adapted from [74].

interest are composed by weakly coupled plasmas in which charged particles are occasionally and rarely dominated by mutual electrostatic influence and where collective electrostatic interactions prevail. Therefore a statistical approach can be used and instead of considering single particles, macro-particles, representative of millions of real plasma particles, can be utilized. Computational particles can be viewed as small pieces of phase space [73] or as blobs of incompressible phase fluid moving in phase space [67] (see figure 2.1). One of the main features of macro-particles is the fact that they have a finite size. In this way, the interaction among computational particles, whether there is particle overlapping, is weaker than in the case of point-like particles. The Coulomb force between point-like particles is proportional to $1/r^2$ in 3D and to $1/r$ in 2D being r the distance between two particles. This means that the force has a singularity for $r \to 0$ while it slowly falls off for $r \to \infty$. This trend for large values of r is the reason behind the collective behavior of a collisionless plasma. When the particles have finite sizes, they feel the same long range force as if they were point particles, but as the distance becomes smaller than their diameter, the particles start to overlap and the force drops off to zero. In this way, the rapidly varying force associated with close encounters is reduced, but the long range relations typical of a collisionless plasma are correctly modeled. Moreover, since quantity variations smaller than a particle size cannot be solved, a spatial grid with spacing about equal to the size of the particles is used, allowing for a further simplification of the field calculations [68].

Summarizing, in a typical PIC algorithm, macro-particles are moved individually in Lagrangian fashion according to the Lorentz equation [74]

$$
\begin{aligned}
\frac{\mathrm{d}\mathbf{p}_i}{\mathrm{d}t} &= q_i \left(\mathbf{E} + \frac{\mathbf{v}_i}{c} \times \mathbf{B} \right) && (2.4) \\
\frac{\mathrm{d}\mathbf{x}_i}{\mathrm{d}t} &= \frac{\mathbf{p}_i}{m_i \gamma_i} && (2.5)
\end{aligned}
$$

where the subscript i has been used to indicate the i^{th} particle, with $i = 1, 2, .., N_p$, being N_p the number of computational particles.

Charge and current densities at the grid points ($\rho(\mathbf{x}_g)$ and $\mathbf{J}(\mathbf{x}_g)$) needed to solve Maxwell's equation are obtained by mapping particle positions and velocities on the grid [73]

$$
\begin{aligned}
\rho(\mathbf{x_g}) &= \sum_i q_i N_p S_x (x_g - x_i) && (2.6) \\
J(\mathbf{x_g}) &= \sum_i q_i N_p S_x (x_g - x_i) && (2.7)
\end{aligned}
$$

where S_x is a function describing the shape of the particles.

Equations (2.6) and (2.7) are inserted into Maxwell's equation to find the new field values at grid points. Finally, these values are interpolated back to the particle positions and the particles are advanced to a new position with equation (2.5), as illustrated in figure 2.2.

2.1.1 OSIRIS FRAMEWORK

Osiris is a massively parallel, fully relativistic and fully object-oriented PIC code for modeling intense beam plasma interactions. The code has been developed for more than ten years by the Osiris consortium composed by University of California at Los Angeles and Instituto Superior Técnico [64,65].

In order to advance the particles, the Boris pusher [66] has been implemented. The method is based on a multi-step process and is second-order accurate in time. Since the code is electromagnetic, only Ampere's and Farday's equations are solved to advance the fields

$$
\begin{aligned}
\frac{\partial \mathbf{B}}{\partial t} &= -c \nabla \times \mathbf{E} && (2.8) \\
\frac{\partial \mathbf{E}}{\partial t} &= c \nabla \times \mathbf{B} - 4\pi \mathbf{J} && (2.9)
\end{aligned}
$$

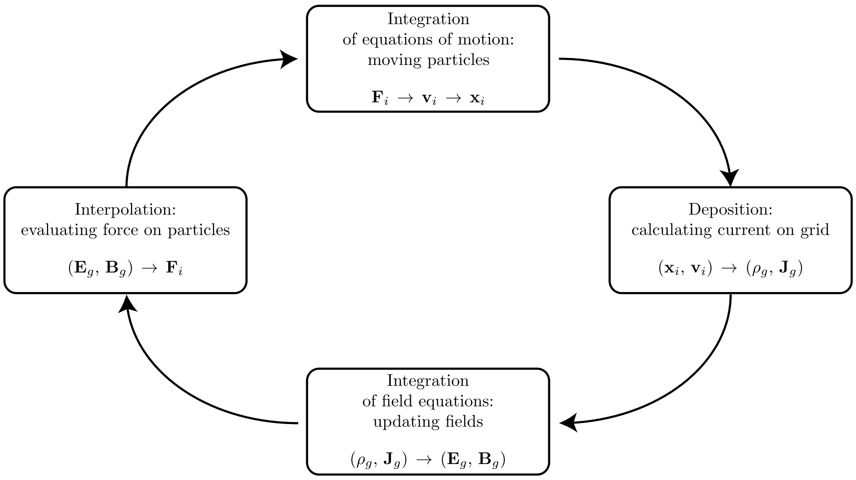
Integration
of equations of motion:
moving particles
$\mathbf{F}_i \to \mathbf{v}_i \to \mathbf{x}_i$
Deposition:
calculating current on grid
$(\mathbf{x}_i, \mathbf{v}_i) \to (\rho_g, \mathbf{J}_g)$
Integration
of field equations:
updating fields
$(\rho_g, \mathbf{J}_g) \to (\mathbf{E}_g, \mathbf{B}_g)$
Interpolation:
evaluating force on particles
$(\mathbf{E}_g, \mathbf{B}_g) \to \mathbf{F}_i$

FIGURE 2.2: Main loop of a typical electromagnetic PIC algorithm. Knowing the particle positions and velocities, the charge and current densities are computed on a grid. These values are plugged into Maxwell's equation to compute the fields. The fields are then interpolated back to the particle position to compute the force acting on the particles. The force is finally used to advance the particles to new positions and velocities.

The rotational operator is replaced by a finite difference approximation on the grid and fields and current are defined on shifted meshes for achieving a second-order accuracy. The integration in time follows a second order accuracy scheme. A charge-conserving current deposition algorithm [75] has been enforced.

Computational particles are loaded into the simulation according to the quiet start technique [68]. Particles have a different weight depending on the initial density profile to simulate.

The code is written in Fortran 90 in an object-oriented way. The parallelization of the code is done for distributed memory system and it is based on the Message Passing Interface (MPI) paradigm [76]. The parallelization is based on a domain decomposition across the available nodes. The output data are saved in the HDF [77] format, a standard, platform independent and self-contained file format. Simulation result visualization is performed with visXD, a custom designed set of IDL (Interactive Data Language) based tools [78].

Recently, Osiris demonstrated excellent scaling in parallel performance on a BlueGene/Q based architecture machine with 1.6 million cores called Sequoia [79], actually the third fastest world supercomputer [80]. Osiris obtained

75% efficiency in what is called strong scaling (increasing number of cores for a fixed size problem) and 97% efficiency in weak scaling (increasing number of cores proportional to the increasing size of the problem).

2.2 SHELL MODEL

PIC codes are powerful tools for simulating phenomena in collisionless plasma. However, in many problems of interest for plasma physics, the numerical particle-mesh technique can be further simplified. This is the case, for instance, of the studies carried out in the present thesis: pure electrostatic phenomena characterized by a high symmetry degree. In these cases, the numerical PIC scheme has been efficiently substituted by a particle-based method, in which the electric field is computed exploiting the Gauss law directly at the position of the computational particles, without using a spatial grid. Imagining, for simplicity, particles distributed at different radii of a sphere, the electric field can be computed considering that each particle behaves like a "shell" and therefore the field at the particle position will be proportional to the charge inside that "shell" (fig. 2.3 (a)). In fact, each shell has an infinitesimal width h with $h \to 0$ and the electric field, discontinuous across each "shell", has a linear behavior inside it. Therefore, the force acting on each computational particle is calculated as the product between the charge and the average between the electric field at the left and at the right hand side of the "shell" (see fig. 2.3 (b))

$$E_p = \frac{E_l + E_r}{2} \tag{2.10}$$

where the subscript p, l and r have been used to identify the electric field felt by the particle and the electric field at the left and right surfaces of the "shell", respectively.

It is important to notice that in such models the plasma collisionality is already low due to the fact that each shell does not represent a real charge, but rather a charge density (the charge is in fact distributed along a "shell") and gets further reduced when the number of shells N_p increases, vanishing for $N_p \to \infty$. Hence, the shell algorithm is appropriate for the study of plasmas dominated by collective electrostatic interactions.

Since it is a gridless algorithm, the shell model reduces computational requirements and provides precise reference solutions. Moreover, it allows, in principle, for studying an infinite domain.

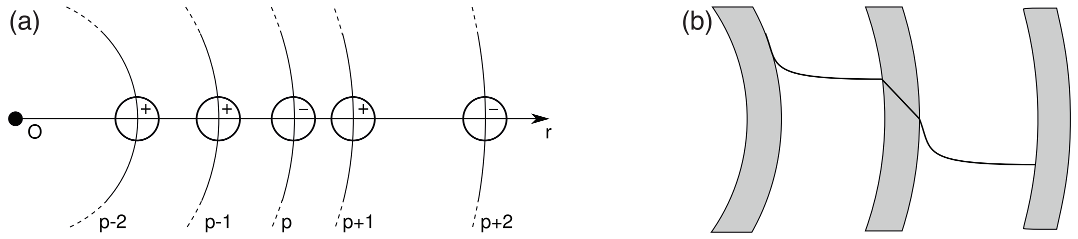
(a)
O
r
+
+
−
+
−
p-2
p-1
p
p+1
p+2
(b)

FIGURE 2.3: (a) Spherical shells constituted by the particles sorted on the radius of a sphere. (b) Qualitative field variations between two "shells" and inside a "shell", where the field is assumed to vary linearly.

A similar scheme has been used by Dawson and by Eldridge and Feix [81, 82], who employed this technique to investigate the properties of systems in thermal equilibrium. Particles were represented by sheets moving along an axis of finite length and interacting through the electric field. Unlike the "shell" model, where the field acting on the particles is computed after each finite time step Δt, sheets are accelerated according to a constant field until two sheets cross and only at this point field, velocity and position values are updated.

Following a similar approach, a reduced electrostatic code called the shell code has been developed. The typical temporal loop of the code is shown in figure 2.4. For the first time the code has been used to study the interaction of two plasma slabs (chapter 4) and the expansion of a plasma into vacuum in spherical geometry (chapter 6).

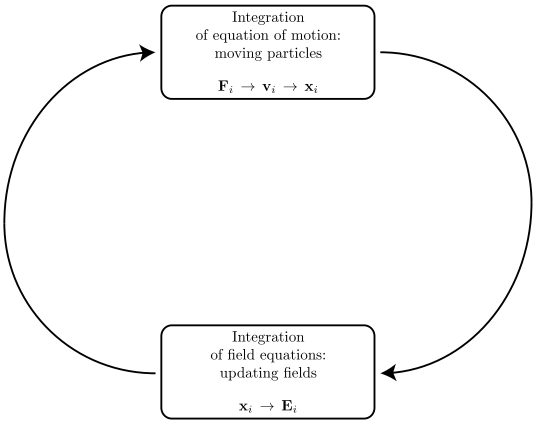
Integration
of equation of motion:
moving particles
$\mathbf{F}_i \rightarrow \mathbf{v}_i \rightarrow \mathbf{x}_i$
Integration
of field equations:
updating fields
$\mathbf{x}_i \rightarrow \mathbf{E}_i$

FIGURE 2.4: Shell algorithm loop. Given the position of the particles, the electric field is computed. The value is then used to update the particle speed and position.

2.2.1 SPHERICAL GEOMETRY

In spherical geometry, once the computational particles have been loaded into the simulation and they have been sorted according to their radii r_i, assuming spherical symmetry, the self consistent radial electric field at a given r_i can be computed as

$$E(r_i) = \frac{Q(r_i)}{r_i^2} \tag{2.11}$$

where $Q(r_i)$ is the charge contained in the sphere of radius r_i, given by the sum of the single charges q_j whose position r_j is smaller than r_i.

$$Q(r_i) = \sum_{j<i} q_j + \frac{1}{2} q_i \tag{2.12}$$

Since the shell model in spherical geometry is implemented according to a 1D3V scheme, after the radial electric field has been calculated at particle position r_i, the three components of the particle velocity $\mathbf{v}_i = (v_{x,i}, v_{y,i}, v_{z,i})$ and position $\mathbf{r}_i = (x_i, y_i, z_i)$ are directly updated as

$$\frac{d\mathbf{v}_i}{dt} = \frac{q_i}{m_i} E(r_i) \frac{\mathbf{r}}{r}_i \tag{2.13}$$

$$\frac{d\mathbf{r}_i}{dt} = \mathbf{v}_i \tag{2.14}$$

In fact, noticing that particle motion happens always on a plane (see fig. 2.5), it is possible to decrease the number of computational operations to perform by replacing $\mathbf{r}$ and $\mathbf{v}$ with two component vectors whose coordinates will be $(r, 0)$ and $(v_r, v_\perp)$, with v_r and $v_\perp$ defined as

$$v_r = \mathbf{v} \cdot \frac{\mathbf{r}}{r} \tag{2.15}$$

$$v_\perp = \left| \mathbf{v} - \frac{\mathbf{r}}{r} v_r \right| \tag{2.16}$$

This allows for a further reduction of the computational time of the model.

2.2.2 PLANE GEOMETRY

In plane geometry, the electrostatic field at the position of each particle can be computed as

$$E(x_i) = 4\pi Q(x_i) \tag{2.17}$$

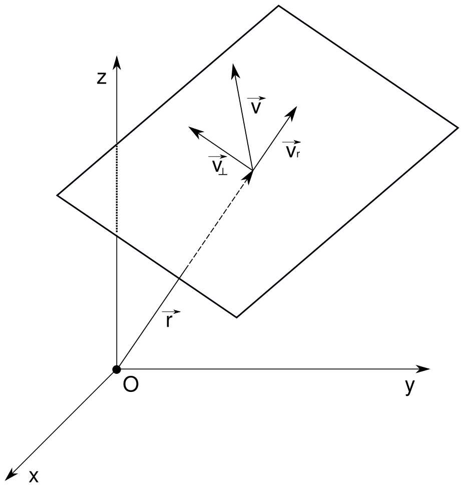

FIGURE 2.5: Relation between coordinates (x, y, z) and $(r, 0)$ and (v_x, v_y, v_z) and $(v_r, v_\perp)$.

where $Q(x_i)$ is given by

$$Q(x_i) = \sum_{j<i} q_j + \frac{1}{2} q_i \tag{2.18}$$

2.2.3 IMPLEMENTATION DETAILS

The model has been numerically implemented in Matlab (for spherical geometry) and in Fortran 90 (for plane geometry).

MATLAB IMPLEMENTATION

Particles are loaded into the simulations with the random start technique [73], using existing Matlab functions RAND for pseudorandom number uniformly distributed and RANDN for pseudorandom number distributed according to a Maxwellian. If a particular distribution is needed, there is the possibility to load particles according to it, using a routine that implements the rejection sampling.

At each time step, particles are sorted according to their radial position using the predefined Matlab function SORT.

Results are saved in files .mat and Matlab routines have been written to analyze and plot them.

FORTRAN IMPLEMENTATION

Particles are loaded into the simulations with the random start technique. The pseudorandom number generator supplied by the IBM Fortran compiler has been used to create a uniform distribution in space and in velocity. The rejection sampling has been implemented to create ad hoc particle distributions in space and velocity.

The heapsort algorithm, having a $O(N_p \log N_p)$ computational complexity, has been implemented to sort the particles at each time step. Particle sorting is the critical point in terms of performance. A possible solution would be implementing a parallel sorting algorithm, like the parallel marge sort, with computational complexity $O(\log N_p)$.

The output data, consisting of particle positions and velocities and electric field, are saved in the HDF format, with a structure comparable to the Osiris output data. Therefore, the visualization can be done using visXD.

2.3 N-BODY SIMULATION TECHNIQUE

In scenarios where the plasma involved is composed by a relativly small number of particles (as, for instance, nanoplasmas generated by the interaction of intense laser pulses with atomic clusters having $N_0 = 10^2 - 10^4$ electrons and ions), an accurate study of the particle dynamics can be obtained solving numerically the system of equations of motion, where the Coulomb force acting on a particle is due to the exact contribution of the other ones that compose the system

$$\frac{\mathrm{d}\mathbf{x}_i}{\mathrm{d}t} = \mathbf{v}_i \tag{2.19}$$

$$\frac{\mathrm{d}\mathbf{v}_i}{\mathrm{d}t} = \sum_{j \neq i} \frac{q_i^2}{m_i} \frac{\mathbf{x}_i - \mathbf{x}_j}{|\mathbf{x}_i - \mathbf{x}_j|^3} \tag{2.20}$$

with $i = 1, 2, .., N_0$.

When the system is composed by such a small number of particles, initial conditions (i.e. initial positions and velocities) of the particles can play a significant role in determining the time dynamics. In order to obtain results as general as possible, ensemble averages have been calculated to take into account the possible different initial conditions of the system. In fact, at time t, any macroscopic quantity $\mathscr{P}$ of the system is a function of the initial conditions, i.e., $\mathscr{P}(t, \{\mathbf{x}_{i0}\}, \{\mathbf{v}_{i0}\})$. Using a different set of random numbers for the initial conditions $\{\mathbf{x}_{i0}^{\alpha}\}, \{\mathbf{v}_{i0}^{\alpha}\}$, a generally distinct solution, $\mathscr{P}_{\alpha}$, is obtained. Therefore, $\mathscr{P}$ is a random variable whose average, $\langle \mathscr{P} \rangle$, is the expected value of the physical quantity. Making use of the results of $\mathscr{M}$ different simulations, $\langle \mathscr{P} \rangle$ can be estimated as $\langle \mathscr{P} \rangle \simeq \overline{\mathscr{P}}$, being

$$\overline{\mathscr{P}} = \frac{1}{\mathscr{M}} \sum_{\alpha=1}^{\mathscr{M}} \mathscr{P}(t, \{\mathbf{x}_{i0}^{(\alpha)}\}, \{\mathbf{v}_{i0}^{(\alpha)}\}) \tag{2.21}$$

Moreover, the ensemble variance $\sigma_{\mathscr{P}}^2$ is also estimated as

$$\sigma_{\mathscr{P}}^2 \simeq \frac{1}{\mathscr{M}-1} \sum_{\alpha=1}^{\mathscr{M}} \left[\mathscr{P}(t, \{\mathbf{x}_{i0}^{(\alpha)}\}, \{\mathbf{v}_{i0}^{(\alpha)}\}) - \overline{\mathscr{P}} \right]^2 \tag{2.22}$$

The standard deviation $\sigma_{\mathscr{P}}$ shows dispersion of $\mathscr{P}_{\alpha}$ values from the average and one can say that a significative number of $\mathscr{P}_{\alpha}$ lies in the interval $\left[\overline{\mathscr{P}} - 2\sigma_{\mathscr{P}}, \overline{\mathscr{P}} + 2\sigma_{\mathscr{P}}\right]$. The ensemble average $\overline{\mathscr{P}}$ converges to the expected value $\langle \mathscr{P} \rangle$ as $\mathscr{M}^{-1/2}$, where $\hat{\sigma}_{\mathscr{M}} = \sigma_{\mathscr{P}}/\sqrt{\mathscr{M}}$ is an estimate of the statistical error of $\overline{\mathscr{P}}$ which lies in the interval $[\langle \mathscr{P} \rangle - 2\hat{\sigma}_{\mathscr{M}}, \langle \mathscr{P} \rangle + 2\hat{\sigma}_{\mathscr{M}}]$ with probability [83] $\frac{1}{\sqrt{2\pi}} \int_{-2}^{2} e^{-t^2/2} dt \simeq 0.95$.

2.3.1 IMPLEMENTATION DETAILS

Equations 2.19 and 2.20 have been solved numerically using the leap-frog integration scheme [66], where the position is updated at integer time steps and the velocity is updated at integer-plus-a-half time steps, resulting in a second order integration algorithm.

Particles are loaded into the simulation according to the random start technique, using pseudorandom numbers.

The code has been written in Fortran 90 and has been parallelized with Open-MPI. In particular, a parallelization over $\mathscr{M}$ simulations has been implemented. The processor number 0 is in charge to generate $\mathscr{M} \times N_0$ initial conditions, where N_0 is the real number of particles of the system. Although this procedure has the advantage of avoiding problems with the generation of random numbers, it is going to slow down the performance of the code. The sets of initial conditions ($\mathbf{x}_{i0}^{\alpha}$ and $\mathbf{v}_{i0}^{\alpha}$ with $i = 1, .. N_0$) for each simulation are saved in $\mathscr{M}$ different files in the HDF format. At this point the tasks are divided among the processors available. Each processors will read a different set of initial conditions and will evolve the particles according to equations 2.19 and 2.20. Results (particle positions and velocities and the electric field) from each simulations are saved in $\mathscr{M}$ different folders, using the HDF file formats. Matlab routines have been written to analyze the data and compute the ensemble averages $\overline{\mathscr{P}}$, the variance $\sigma^2_{\mathscr{P}}$ and the standard deviation $\hat{\sigma}_{\mathscr{M}}$ for different macroscopic quantities $\mathscr{P}$.

Part I

Ion Shock Wave Acceleration

CHAPTER 3

THEORY OF ELECTROSTATIC SHOCK WAVES

The formation of electrostatic shock waves in unmagnetized plasmas is associated to the steepening of ion acoustic waves (IAW) propagating in plasmas composed by cold ions and hot electrons [84]. Consider for example a sinusoidal potential wave traveling in a plasma: the ions will experience a different acceleration depending on their position. In particular ions at the peak of the wave will feel a force dragging them in the direction of the phase velocity v_{ph}, while the ones at the back will feel a force dragging them in the opposite direction. This process will cause a steepening of the wave shape. Moreover, since the density perturbation is in phase with the potential, there will be a net mass flow in the propagation direction. This will result in an increase of the wave velocity that will eventually exceed the sound speed in the unperturbed plasma. As a result the Mach number M, ratio between the wave and the sound speed, will be higher than one.

3.1 ION ACOUSTIC SOLITON

Theoretical analysis of ion acoustic shock waves can be carried out applying the same techniques used to study ion acoustic solitons. To derive a theory for electrostatic shocks waves, the so-called Sagdeev formalism [85] will be

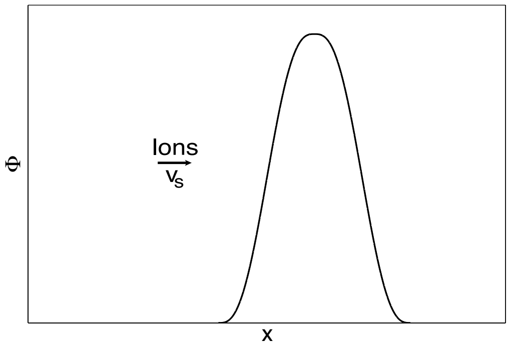

FIGURE 3.1: Sketch of a soliton wave. In the soliton reference frame, cold plasma ions are moving to the right. Electrons are considered always in equilibrium.

used. In this section, a review of the model for the simple case of an ion acoustic soliton will be illustrated.

Consider a soliton wave traveling in a plasma with cold ions and hot electrons, as in figure 3.1. The wave is moving to the left with speed v_s, much smaller than the electron thermal velocity $v_{th,e} = \sqrt{k_B T_e / m_e}$, where k_B is the Boltzmann constant, T_e the electron temperature and m_e the electron mass. In the reference frame of the wave (i.e. the frame in which the wave is at rest), all the quantities do not depend on time and the equation of mass and energy conservation can be applied in order to find the ion speed v_i and density n_i as functions of the electrostatic potential $\Phi(x)$ of the wave

$$v_i(\Phi) = \sqrt{v_s^2 - \frac{2e\Phi}{m_i}} \tag{3.1}$$

$$n_i(\Phi) = \frac{n_0}{\sqrt{1 - \frac{2e\Phi}{m_i v_s^2}}} \tag{3.2}$$

where e is the elementary charge, m_i is the ion mass and n_0 is the density in the unperturbed plasma.

The electrons can be considered in equilibrium and therefore their density is given by

$$n_e = n_0 \exp\left(\frac{e\Phi}{k_B T_e}\right) \tag{3.3}$$

Inserting equations (3.2) and (3.3) in the Poisson equation, the system closes

$$\frac{\mathrm{d}^2\Phi}{\mathrm{d}x^2} = -4\pi e(n_i - n_e) = -4\pi e n_0 \left(\frac{1}{\sqrt{1 - \frac{2e\Phi}{Mv_s^2}}} - \exp\left(\frac{e\Phi}{k_B T_e}\right) \right) \tag{3.4}$$

Introducing the dimensionless quantities

$$\varphi = \frac{e\Phi}{k_B T_e} \tag{3.5}$$

$$\chi = \frac{x}{\lambda_D} \tag{3.6}$$

$$M = \frac{v_s}{c_s} \tag{3.7}$$

where $\lambda_D = \sqrt{k_B T_e / 4\pi e^2 n_0}$ is the Debye length, $c_s = \sqrt{k_B T_e / m_i}$ is the ion sound speed and M is the soliton Mach number, the Poisson equation (3.4) becomes

$$\frac{\mathrm{d}^2\varphi}{\mathrm{d}\chi^2} = -\frac{\mathrm{d}\Psi(\varphi)}{\mathrm{d}\varphi} \tag{3.8}$$

with the right hand side defined as

$$\frac{\mathrm{d}\Psi(\varphi)}{\mathrm{d}\varphi} = \frac{1}{\sqrt{1 - \frac{2\varphi}{M^2}}} - \exp\varphi \tag{3.9}$$

The quantity $\Psi(\varphi)$ takes the name of Sadgeev potential from the analogy with the equation of motion for the harmonic oscillator

$$m\frac{\mathrm{d}^2x}{\mathrm{d}t^2} + \frac{\mathrm{d}V}{\mathrm{d}x} = 0 \tag{3.10}$$

Equation (3.10) has in fact the same structure of equation (3.8), where φ plays the role of x and Ψ can be seen as a pseudo-potential.

Integration of the equation (3.8) respect to φ results in

$$\frac{1}{2}\left(\frac{\mathrm{d}\varphi}{\mathrm{d}\chi}\right)^2 + \Psi - \Psi_0 = 0 \tag{3.11}$$

with

$$\Psi(\varphi) = -\exp(\varphi) - M^2\sqrt{1 - \frac{2\varphi}{M^2}} + \Psi_0 \tag{3.12}$$

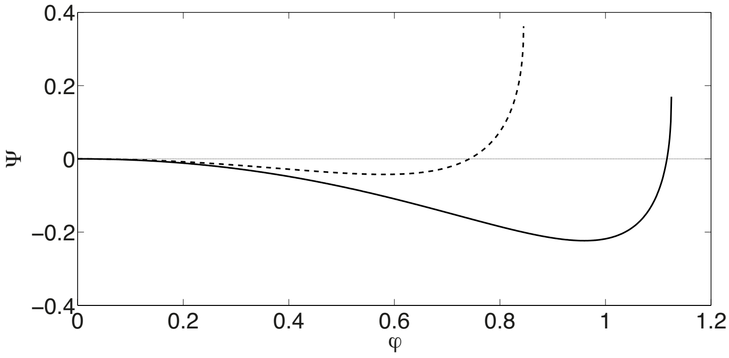

FIGURE 3.2: Sagdeev potential (Ψ) as a function of φ for $M = 1.3$ (dashed line) and $M = 1.5$ (solid line).

where the constant Ψ_0 is chosen in a way that $\Psi(\varphi) = 0$ for $\varphi = 0$, leading to

$$\Psi(\varphi) = 1 - \exp(\varphi) + M^2 \left(1 - \sqrt{1 - \frac{2\varphi}{M^2}}\right) \tag{3.13}$$

Figure 3.2 shows the shape of the pseudo potential Ψ. Consider a particle entering from the left. It will go to the right, then it will be reflected and it will come back making a single transit. In this case what has been called quasi-particle is the potential disturbance of the soliton wave traveling with speed v_s.

Equation (3.11) determines the condition for the existence of a soliton solution as $\Psi(\varphi, M) < 0$ for $\varphi \ll 1$

$$\Psi(\varphi) \overset{\varphi \ll 1}{\simeq} -\frac{\varphi^2}{2} + \frac{\varphi^2}{2M^2} < 0 \tag{3.14}$$

determining the minimum Mach number

$$M_{min} = 1 \tag{3.15}$$

An additional condition to impose is that the potential does not raise indefinitely: the virtual particle has to be reflected back. This is equivalent to ask that $\Psi(\phi) > 0$ at the maximum critical φ_{cr}

$$\varphi_{cr} = \frac{M^2}{2} \tag{3.16}$$

By plugging this value inside equation (3.13), M_{max}, the maximum Mach number, is obtained

$$\begin{aligned} M^2 + 1 - \exp\left(-\frac{M^2}{2}\right) &> 0 \qquad (3.17) \\ M_{max} &\simeq 1.6 \qquad (3.18) \end{aligned}$$

In conclusion, soliton acoustic wave can exist in a cold-ion plasma only if their Mach number is in the range $1 - 1.6$.

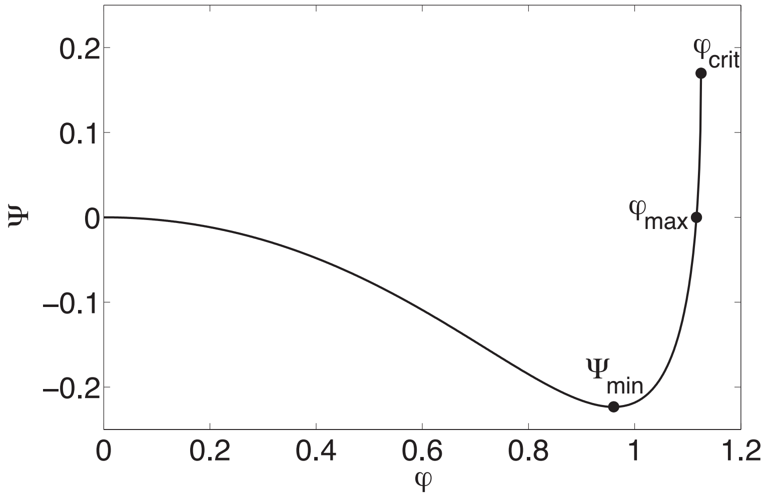

FIGURE 3.3: Sagdeev potential with points that lead to the determination of the minimum and the maximum Mach number.

Equation (3.16) can also be rewritten as

$$e\Phi \leq \frac{1}{2} m_i v_s^2 \qquad (3.19)$$

clearly showing that the potential energy can not exceed the kinetic energy of the ions, in other case there would be no ions in the downstream region.

3.2 SOLITARY SOLUTION CONSIDERING ELECTRON DISTRIBUTION FUNCTIONS

So far electrons in equilibrium with the ions have been considered. The model can be improved by looking at the different features of the particle populations that maintain the double layer [21,86,87]. Referring to figure 3.4, we can distinguish between free electrons and ions with kinetic energy higher than the potential one and electrons trapped in the upstream region of the shock, whose kinetic energy is less than the potential one. In the following derivation, electrons are treated kinetically, while ions, that are supposed to be cold, are treated as fluid. The electron distribution functions have to be solution of the stationary Vlasov equation and can be determined from the particle distributions in the unperturbed plasma. Depending on the temperature of the electrons, two different cases can be distinguished: classical, treated in subsection 3.2.1 and relativistic, discussed in subsection 3.2.2.

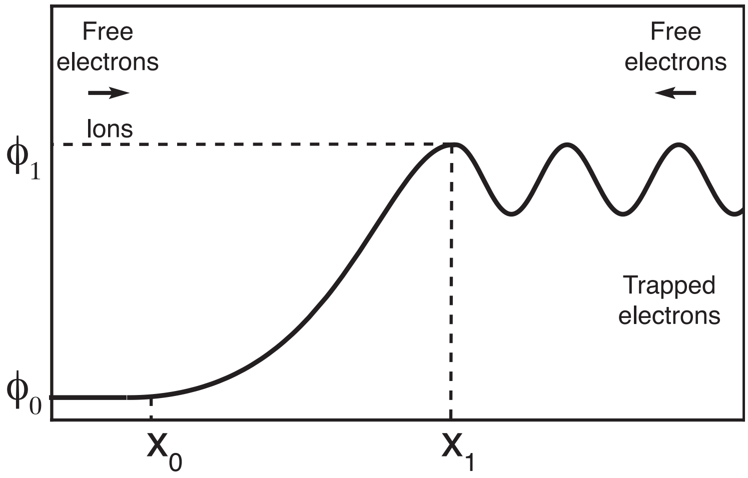

FIGURE 3.4: Electrostatic shock in the shock reference frame. The line represents the potential. Electron and ion populations are shown with their respective velocities, temperatures and unperturbed densities in the upstream and downstream regions.

3.2.1 CLASSICAL THEORY

In the soliton reference frame, the free electron population propagating from the upstream to the downstream region is described by the Maxwell-

Boltzmann distribution function, with temperature T_0 and fluid velocity v_s

$$f_0(v_0) = \frac{2N_0}{v_{th,0}\sqrt{2\pi}} \exp\left[-\frac{(v_0 - v_{sh})^2}{2v_{th,0}^2}\right] \tag{3.20}$$

where N_0 is the unperturbed electron density in the far upstream region ($x \to -\infty$), $v_0 > 0$ is the particle velocity and $v_{th,0}$ represents the electron thermal speed. The free electrons in the downstream region, whose fluid velocity is equal to zero in the shock reference frame, obey the Maxwellian distribution

$$f_1(v_1) = \frac{2N_1}{v_{th,1}\sqrt{2\pi}} \exp\left[-\frac{v_1^2}{2v_{th,1}^2} + \frac{e(\Phi_1 - \Phi_0)}{k_B T_1}\right] \tag{3.21}$$

where N_1 represents the density at $x \to -\infty$, $v_1 < 0$ is the particle speed and $v_{th,1}$, different from $v_{th,0}$, is the thermal velocity. The trapped electrons are represented by the flat-top distribution function

$$f_{1t} = \frac{2N_1}{\sqrt{2\pi}v_{th,1}} \tag{3.22}$$

according to the so called maximum-density-trapping approximation [88, 89], which guarantees $f_1(v_1 = v_c) = f_{1t}$ at the critical velocity

$$v_c = \sqrt{\frac{2e(\Phi_1 - \Phi_0)}{m_e}} \tag{3.23}$$

that discriminates between free ($v_1 < -v_c$) and trapped electrons ($|v_1| < v_c$).

Applying the conservation of energy, the electron velocity v_e in the shock frame can be written in terms of the upstream and downstream velocities

$$v_e = \sqrt{v_0^2 + \frac{2e(\Phi - \Phi_0)}{m_e}} = -\sqrt{v_1^2 + \frac{2e(\Phi - \Phi_1)}{m_e}} \tag{3.24}$$

The electron densities in the upstream n_0 and in the downstream n_1 are computed integrating the distribution functions (3.20), (3.21) and (3.22) in the proper limits

$$n_0(\Delta\varphi) = N_0 e^{\Delta\varphi} \operatorname{erfc}(\sqrt{\Delta\varphi}) \tag{3.25}$$

$$n_1(\Delta\varphi) = N_0 \Gamma e^{\frac{\Delta\varphi}{\Theta}} \operatorname{erfc}(\sqrt{\frac{\Delta\varphi}{\Theta}}) + \frac{4}{\sqrt{\pi}} N_0 \Gamma \sqrt{\frac{\Delta\varphi}{\Theta}} \tag{3.26}$$

where the dimensionless quantities $\Delta\varphi = \frac{e(\Phi-\Phi_0)}{k_B T_0}$, $\Gamma = N_1/N_0$ and $\Theta = T_1/T_0$ have been used and erfc denotes the complementary error function.

Using the fluid equations for ion mass and energy conservation and assuming that the ions are cold and that none of them is reflected at the potential, the ion density can be determined as

$$n_i(\Delta\varphi) = \frac{N_i}{\sqrt{1-\frac{2(\Delta\varphi)}{M^2}}} \tag{3.27}$$

Charge neutrality is imposed at $x = x_0$ yielding to the relation between the initial densities of electrons and ions $N_i = N_0 + N_1$. The particle densities are then combined in Poisson equation

$$\frac{\mathrm{d}^2\Delta\varphi}{\mathrm{d}\chi^2} = \frac{1}{1+\Gamma}\left(\mathrm{e}^{\Delta\varphi}\,\mathrm{erfc}\,\sqrt{\Delta\varphi} + \Gamma\mathrm{e}^{\frac{\Delta\varphi}{\Theta}}\,\mathrm{erfc}\,\sqrt{\frac{\Delta\varphi}{\Theta}} + \frac{4\Gamma}{\sqrt{\pi}}\sqrt{\frac{\Delta\varphi}{\Theta}}\right) - \frac{1}{\sqrt{1-\frac{2\Delta\varphi}{M^2}}}, \tag{3.28}$$

where the normalized quantity (3.6) has been introduced. The right hand side of equation (3.28) can be defined as $-\frac{\mathrm{d}\Psi(\Delta\varphi)}{\mathrm{d}\Delta\varphi}$, bringing up once again the similarity to the harmonic oscillator and allowing to identify bounded solutions. Integration of equation (3.28) with respect to $\Delta\varphi$ leads to

$$\frac{1}{2}\left(\frac{\mathrm{d}\Delta\varphi}{\mathrm{d}\chi}\right)^2 + \Psi(\Delta\varphi) - \Psi_0 = 0 \tag{3.29}$$

with the non-linear Sagdeev potential given by

$$\begin{aligned} \tilde{\Psi}(\Delta\varphi, M, \Gamma, \Theta) &= \Psi(\Delta\varphi, M, \Gamma, \Theta) - \Psi_0 = \\ &= P_i(\Delta\varphi, M) - P_{e0}(\Delta\varphi, \Gamma) - P_{e1}(\Delta\varphi, \Gamma, \Theta) \end{aligned} \tag{3.30}$$

where the quantities P_i, P_{e0} and P_{e1} represent the ion, the upstream electron and the downstream electron pressures respectively

$$P_i(\Delta\varphi, M) = M^2\left(1-\sqrt{1-\frac{2\Delta\varphi}{M^2}}\right) \tag{3.31}$$

$$P_{e0}(\Delta\varphi, \Gamma) = \frac{1}{1+\Gamma}\left(\frac{2\sqrt{\Delta\varphi}}{\sqrt{\pi}} + \mathrm{e}^{\Delta\varphi}\,\mathrm{erfc}\,\sqrt{\Delta\varphi} - 1\right) \tag{3.32}$$

$$P_{e1}(\Delta\varphi, \Gamma, \Theta) = \frac{\Theta\Gamma}{1+\Gamma}\left(\frac{2}{\sqrt{\pi}}\sqrt{\frac{\Delta\varphi}{\Theta}} + \mathrm{e}^{\frac{\Delta\varphi}{\Theta}}\,\mathrm{erfc}\,\sqrt{\frac{\Delta\varphi}{\Theta}} + \frac{8}{3\sqrt{\pi}}\Delta\varphi\sqrt{\frac{\Delta\varphi}{\Theta^3}} - 1\right) \tag{3.33}$$

obtained by imposing $\Psi(\Delta\varphi = 0) = \Psi_0$.

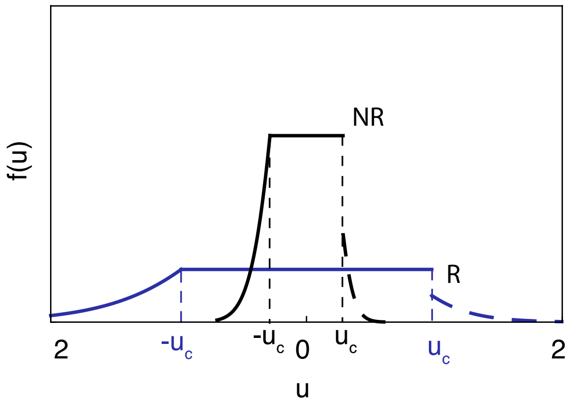

FIGURE 3.5: Electron distribution functions upstream f_0 (dashed line) and downstream $f_1 + f_{1t}$ (solid line) for relativistic electron temperature (R) $\mu_0 = 5$ (blue) and non-relativistic temperature (NR) $\mu_0 = 50$ (black) with $\Gamma = 3$, $\Theta = 2$, $(e(\phi_1 - \phi_0)/m_e c^2 = 2$ and $\beta_{sh} = 0.02$. The more convenient variable $u = \beta\gamma$ has been introduced.

3.2.2 RELATIVISTIC THEORY

In the case of relativistic electron temperatures, the free electron populations are described by one-dimensional Jüttner distribution functions [90]

$$f_0(\gamma_0) = N_0 K_1^{-1}(\mu_0)\,\gamma_0(\gamma_0^2 - 1)^{-1/2} \exp[-\mu_0\gamma_0(1 - \beta_0\beta_{sh})] \tag{3.34}$$

$$f_1(\gamma_1) = N_1 K_1^{-1}(\mu_1)\,\gamma_1(\gamma_1^2 - 1)^{-1/2} \exp\left[-\mu_1\gamma_1 + \frac{e(\Phi_1 - \Phi_0)}{k_B T_1}\right] \tag{3.35}$$

where $\beta_\alpha = v_\alpha/c > 0$ is the normalized velocity of the electrons, c is the speed of light, $\gamma_\alpha = (1 - \beta_\alpha^2)^{-1/2}$ is the Lorentz factor, $\mu_\alpha = m_e c^2/k_B T_\alpha$ is the thermal parameter and $\beta_{sh} = v_{sh}/c$ is the normalized velocity of the shock wave. The normalization constants contain the density of the left and the right electron population N_0 and N_1 in the far upstream region $(x < x_0)$ and the modified Bessel function of the second kind K_1. The downstream distribution function takes into account the potential difference $\Phi_1 - \Phi_0$. The trapped electron population, described by the maximum density approximation as in the non relativistic theory, is rewritten using relativistic notation

$$f_{1t} = N_1 K_1^{-1}(\mu_1)\,\gamma_1(\gamma_1^2 - 1)^{-1/2} \exp(-\mu_1) \tag{3.36}$$

At the critical Lorentz factor $\gamma_c = 1 + e(\Phi_1 - \Phi_0)/m_e c^2$, that discriminates between free $(\beta_1 < -\beta_c)$ and trapped electrons $(|\beta_1| < \beta_c)$, $f_1(\gamma_1 = \gamma_c)$ coincides with f_{1t} . The electron distributions are shown in figure 3.5 as a function of $u = \beta\gamma$ for relativistic and non relativistic temperatures.

Introducing the electron Lorentz factor γ_e which accounts for the electrostatic potential in the shock frame, the upstream and downstream Lorentz factors can be written as

$$\gamma_e = \gamma_0 + e(\Phi - \Phi_0)/m_e c^2 = \gamma_1 - e(\Phi_1 - \Phi)/m_e c^2 \geq 1 \qquad (3.37)$$

The electron density is computed as $n_e = \int_1^\infty f_e(\gamma_e)\, d\gamma_e$, thus obtaining the electron densities in the upstream region

$$n_0(\Delta\varphi) = N_0\, \mathrm{K}_1^{-1}(\mu_0)\mathrm{e}^{\Delta\varphi} \int_{1+\Delta\varphi/\mu_0}^{\infty} \mathrm{e}^{-\mu_0\gamma_e}\gamma_e(\gamma_e^2 - 1)^{-1/2}\, d\gamma_e \qquad (3.38)$$

and in the downstream region

$$\begin{aligned} n_1(\Delta\varphi) \;&=\; N_0\Gamma\mathrm{K}_1^{-1}(\mu_0/\Theta) \left[\mathrm{e}^{\Delta\varphi/\Theta} \int_{1+\Delta\varphi/\mu_0}^{\infty} \mathrm{e}^{-\mu_0\gamma_e/\Theta}\gamma_e(\gamma_e^2 - 1)^{-1/2}\, d\gamma_e + \right. \\ &\left. +2\mathrm{e}^{-\mu_0/\Theta}\sqrt{(1+\Delta\varphi/\mu_0)^2 - 1}\right] \qquad (3.39) \end{aligned}$$

with the dimensionless quantities $\Delta\varphi = e(\Phi - \Phi_0)\mu_0/m_e c^2$ and $\Theta = \mu_0/\mu_1$.

Following the same procedure of section 3.2.1, the electron kinetic pressure terms that appear in equation (3.30) can be evaluated as

$$P_{e0}(\Delta\varphi, \Gamma, \mu_0) \;=\; \frac{1}{1+\Gamma}\left[\frac{\mu_0}{K_1(\mu_0)}\int_1^\infty d\gamma\, \mathrm{e}^{-\mu_0\gamma}\sqrt{\left(\gamma + \frac{\Delta\varphi}{\mu_0}\right)^2 - 1} - 1\right] \qquad (3.40)$$

$$\begin{aligned} P_{e1}(\Delta\varphi, \Gamma, \Theta, \mu_0) \;&=\; \frac{\Gamma\Theta}{1+\Gamma}\left[\frac{\mu_0 \mathrm{e}^{-\mu_0/\Theta}}{\Theta K_1(\mu_0/\Theta)}\right. \\ &\left\{\int_1^\infty d\gamma\, \mathrm{e}^{-\mu_0(\gamma-1)/\Theta}\sqrt{\left(\gamma + \frac{\Delta\varphi}{\mu_0}\right)^2 - 1}\right. \\ &\left.\left. +\; s\sqrt{s^2-1} - \log\left[s + \sqrt{s^2 - 1}\right]\right\} - 1\right] \qquad (3.41) \end{aligned}$$

with $s = 1 + \Delta\varphi/\mu_0$. For highly relativistic electron temperatures, $\mu_0 \ll 1$, the pressures (3.40) and (3.41) are approximated by

$$P_{e0}^r(\Delta\varphi, \Gamma) \;=\; \frac{\Delta\varphi(1-\mu_0)}{1+\Gamma} \qquad (3.42)$$

$$P_{e1}^r(\Delta\varphi, \Gamma, \Theta) \;=\; \frac{\Delta\varphi\Gamma}{\Theta(1+\Gamma)}\left[\Delta\varphi\left(1 - \frac{\mu_0}{\Theta}\right) + \Theta\left(1 + \frac{\mu_0}{\Theta}\right)\right] \qquad (3.43)$$

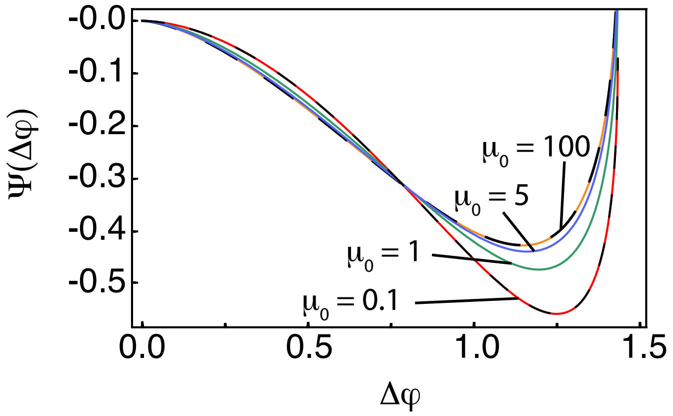

FIGURE 3.6: Sagdeev potential $\Psi(\varphi)$ obtained from equations (3.30)-(3.41) for $M = 1.7$, $\Gamma = 3$, $\Theta = 1$ and $\mu_0 = 0.1$ (red), 1 (green), 5 (blue), 100 (orange). The non-relativistic and highly relativistic approximations given by equations (3.31), (3.32), (3.33), (3.42), (3.43) are represented by dashed lines.

Figure 3.6 shows the Sagdeev potential for upstream electron temperatures $\mu_0 = 0.1 - 100$ and a comparison with the nonrelativistic and highly relativistic approximations (3.31), (3.32), (3.33), (3.42), (3.43).

3.2.3 MACH NUMBER

As for the soliton case (see 3.1), the model holds for

$$\Delta\varphi < M^2/2 = \Delta\varphi_{cr} \tag{3.44}$$

The ion pressure becomes imaginary when the electrostatic potential exceeds the ion kinetic energy

$$e\Delta\Phi > \frac{1}{2}m_i v_i^2 \tag{3.45}$$

and the ions are reflected by the shock potential. We define the Mach number at which ion reflection sets in as the maximum Mach number M_{max}. In order to determine possible shock solutions with M_{max}, we use equation (3.29) which gives the condition for the existence of a monotonic double layer solution as

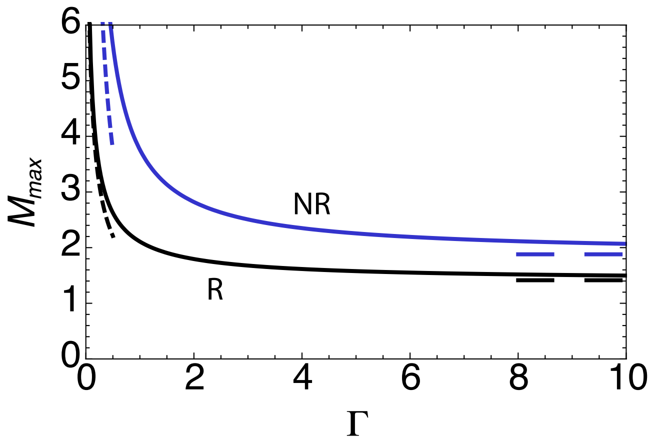

FIGURE 3.7: Maximum Mach number versus density ratio for the highly relativistic case $\mu_0 = 0.1$ (black) given by equation (3.49) and the non-relativistic case given in [21] (blue) for a temperature ratio $\Theta = 1$. The dependences for very small and very large density ratios are indicated by the dashed lines.

$\tilde{\Psi} = \Psi(\Delta\varphi, M, \Gamma, \Theta) - \Psi_0 < 0$. For a given Mach number M, a soliton-like solution is possible only if the electron pressure exceeds the ion pressure. The solutions are found numerically by solving $\tilde{\Psi}(M^2/2, M, \Gamma, \Theta) = 0$ and are shown in figure 3.7.

As already found in [21], the analytical dependence of the maximum Mach number in the non-relativistic approximation is given by

$$M_{max} = 3\sqrt{\pi\Theta/8}(1+\Gamma)/\Gamma \tag{3.46}$$

which is

$$M_{max} \simeq 3\sqrt{\pi\Theta/8} \tag{3.47}$$

for large density ratios and has a

$$M_{max} \propto \Gamma^{-1} \tag{3.48}$$

dependence for low density ratios. In the case of highly relativistic temperatures, $\mu_0 \ll 1$, the maximum Mach number can be approximated as

$$M_{max} = \sqrt{2\Theta\left(1+\frac{1+\mu_0}{\Gamma(1-\mu_0/\Theta)}\right)} \tag{3.49}$$

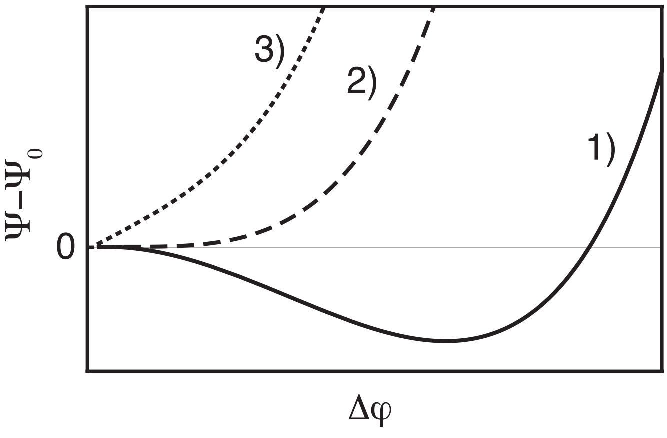

FIGURE 3.8: Different types of the Sagdeev potential $\tilde{\Psi}(\Delta\varphi) = \Psi - \Psi_0$.

which is displayed in figure 3.7 together with the non-relativistic expression (3.46). It can be easily seen that the maximum Mach number is constant for high density ratios ($\Gamma \gg 1$) as in the non-relativistic case

$$M_{max} \simeq \sqrt{2\Theta} \tag{3.50}$$

while it has a dependence

$$M_{max} \simeq \sqrt{2\Theta(1+\mu_0)/\Gamma(1-\mu_0/\Theta)} \propto \Gamma^{-1/2} \tag{3.51}$$

for $\Gamma \ll 1$. The comparison of the non-relativistic and highly relativistic cases in figure 3.7 for a temperature ratio $\Theta = 1$ shows that for higher upstream electron temperatures the maximum Mach number is reduced, in accordance with the model for equal density and temperature ratios [91].

The lower limit and the range of possible Mach numbers for given temperature and density ratios have been analyzed. The shape of the Sagdeev potential and thus the existence of shock solutions depends on the choice of Γ and Θ and three different types of solutions (shown in Figure 3.8) can be distinguished. Case (1) represents the case where shock solutions exist for $\tilde{\Psi} = \Psi - \Psi_0 < 0$ and $\Delta\varphi > 0$. While the monotonously growing Sagdeev potential in case (3) does not allow for shock solutions, case (2) defines the threshold with $\Delta\varphi = 0$ and provides the conditions to determine the minimum Mach number, which are given by $d\tilde{\Psi}/d\Delta\varphi = 0$ and $\tilde{\Psi}(\Delta\varphi) = 0$. While in the highly relativistic limit $M = 1$ is the lower limit, in the non-relativistic case a lower limit $M > 1$ exists.

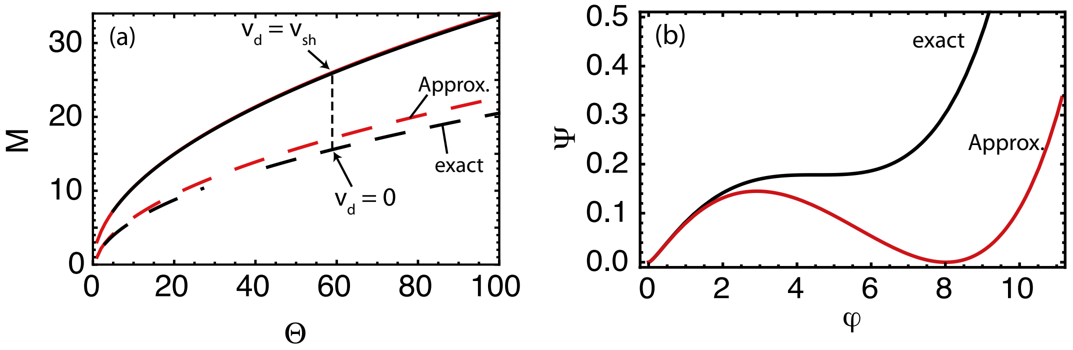

FIGURE 3.9: (a) M_{min} (dashed) and M_{max} (solid) for the approximation $\varphi_0 = 0$ (red) and comparison with the exact solution (black) for $\Gamma = 1$. The dashed vertical line shows the transition from M_{min} to M_{max} for downstream velocities $0 \leq v_d \leq v_{sh}$. (b) Sagdeev potential for the minimum Mach number with $\Delta\varphi = 0$ (black) and comparison with the approximation $\varphi_0 = 0$ (red).

The Sagdeev potential is expanded for $\Delta\varphi \ll 1$ since the interesting solutions will be for $\Delta\varphi \to 0$, obtaining

$$\begin{aligned} \tilde{\Psi}(\Delta\varphi, M, \Gamma, \Theta) \quad \simeq \quad & \Delta\varphi^2 \left[\frac{1}{2M^2(1-\frac{2\varphi_0}{M^2})^{3/2}} + \frac{1}{2(1+\Gamma)} \cdot \right. \\ & \left. \cdot \quad \left(\frac{1-\Gamma\Theta^{-1/2}}{\sqrt{\varphi_0\pi}} - e^{\varphi_0}\mathrm{erfc}(\sqrt{\varphi_0}) - \frac{\Gamma}{\Theta} e^{\varphi_0/\Theta}\mathrm{erfc}(\sqrt{\frac{\varphi_0}{\Theta}}) \right) \right] \end{aligned} \tag{3.52}$$

which is a function of the upstream potential φ_0. The minimum Mach number can then be found by solving $\tilde{\Psi}(\Delta\varphi, M(\varphi_0), \Gamma, \Theta) = 0$ with the Mach number at the minimum of the Sagdeev potential given by

$$M(\varphi_0) = \frac{\sqrt{2\varphi_0}}{\sqrt{1 - \frac{(1+\Gamma)^2}{\left[e^{\varphi_0}\mathrm{erfc}[\sqrt{\varphi_0}] + \Gamma\left(4\sqrt{\frac{\varphi_0}{\pi\Theta}} + e^{\varphi_0/\Theta}\mathrm{erfc}[\sqrt{\varphi_0/\Theta}]\right)\right]^2}}} \tag{3.53}$$

For large temperature ratios small deviations from the approximation $\varphi_0 = 0$ [21], which is equivalent to $\Psi_0 = 0$ in equation (3.29) have been found (see Figure 3.9 (a)). Panel (b) shows the respective Sagdeev potentials with $\Psi_0 = 0$ for the minimum Mach number according to $\Delta\varphi = 0$ in black and for the approximated model with $\varphi_0 = 0$ in red. The exact solution predicts the formation of electrostatic shocks at slightly lower Mach numbers.

The transition between minimum and maximum Mach number can be described as a function of the steady state ion speed in the downstream region, v_d. In the rest frame of the shock, the upstream ions propagate towards the shock with velocity $v_{i,us} = v_{sh}$ and are decelerated by the shock potential φ to velocities in the downstream $0 \leq v_{i,ds} \leq v_{sh}$. The velocity is $v_{i,ds} = 0$ if the ions are completely stopped by the potential and $v_{i,ds} = v_{sh}$ if they are unaffected and stream freely in the downstream region. In the upstream frame this corresponds to ion downstream velocities $-v_i \leq v_{i,du} = -v_d \leq 0$. Starting from the energy conservation for ions, the downstream ion speed can be related to the shock potential

$$\frac{v_d}{c_s} = M - \sqrt{M^2 - 2\Delta\varphi} \tag{3.54}$$

and using

$$\Delta\varphi_d = \frac{M^2}{2}\left[1 - \left(1 - \frac{v_d}{v_{sh}}\right)^2\right] \tag{3.55}$$

to find the zeros of the Sagdeev potential $\tilde{\Psi}(\Delta\varphi_d, M, \Gamma, \Theta)$ in order to determine the Mach number M. This transition is shown in figure 3.9 (a). When the shock propagates with a speed slightly above the minimum Mach number, the downstream will have almost the same speed as the upstream population due to the small potential jump that has only a weak effect on the particles. At the maximum Mach number, the potential jump is so strong that the downstream propagates with the same speed as the shock front.

3.3 ION ACOUSTIC SHOCK WAVE

So far, the solitary solutions in the upstream region have been described, while the processes leading to a shock solution have not been treated. A shock solution can arise due to different physical mechanisms that break the symmetry [17]. For instance, a very small ion temperature is sufficient to lead to an oscillating solution (cp. [92]). To describe this, a population of reflected ions is included in the model. The electrostatic potential in the upstream region is computed as in subsections 3.2.1 and 3.2.2, with the extension of a kinetic treatment of the ions. On the basis of [93–95], the ion populations are described by a Maxwellian distribution

$$f_i = \frac{n_i}{\sqrt{2\pi} v_{th,i}} \exp\left[-\frac{1}{2v_{th,i}^2}\left(\sqrt{v^2 + 2c_{s0}^2\varphi} - c_{s0}M\right)^2\right] \tag{3.56}$$

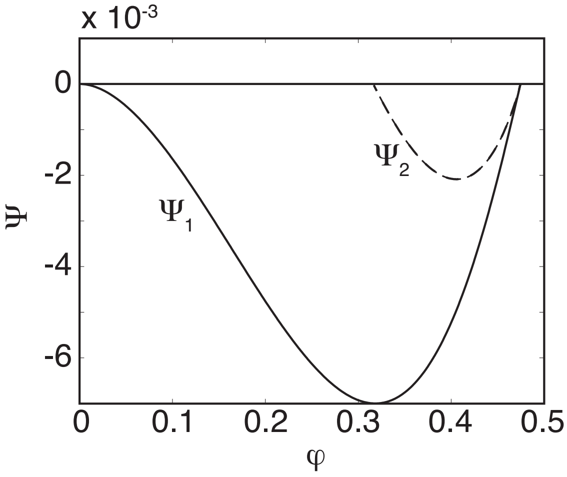

FIGURE 3.10: Sagdeev potentials for $T_e = 10$ keV, $T_i = 0.5$ keV, $M = 1.5$ and $\Theta = \Gamma = 1$. Potential Ψ_1 (solid) corresponds to $0 \leq \chi \leq \chi_m$ and Ψ_2 (dashed) to $\chi > \chi_m$.

with thermal velocity $v_{th,i} = \sqrt{k_B T_i / m_i}$ and unperturbed ion density n_i defined to guarantee charge neutrality with the electrons in the far upstream region $\chi \to -\infty$. The free particle population has velocities

$$v > v_c = \sqrt{2(\varphi - \varphi_1)c_{s0}^2} \tag{3.57}$$

and the reflected population $0 \leq v \leq v_c$. Since an exact analytical solution cannot be found, the equations are numerically solved. The Sagdeev potential Ψ_1 is computed for $\chi \leq \chi_m$ where χ_m is the position of the maximum of the electrostatic potential and the connection point with the oscillatory downstream region of the shock, described by a second Sagdeev potential Ψ_2 (see figure 3.10). For the computation of the latter, two populations of free ions and electrons as well as trapped electrons are considered.

Figure 3.11 shows the corresponding electrostatic potential against the spatial coordinate, which consists of a monotonously increasing part for $\chi \leq \chi_m$ and an oscillatory downstream region for $\chi > \chi_m$. We also compare the solution where ion reflection was neglected (dashed red) with the extended model. For an ion temperature corresponding to 0.5 keV, we observe only a small deviation from the cold model. For the same potential difference, the maximum Mach number increases as it was expected [21].

Figure 3.12 shows the electron and ion phase spaces, where the different populations (free, trapped, reflected) can be identified. The ion density fol-

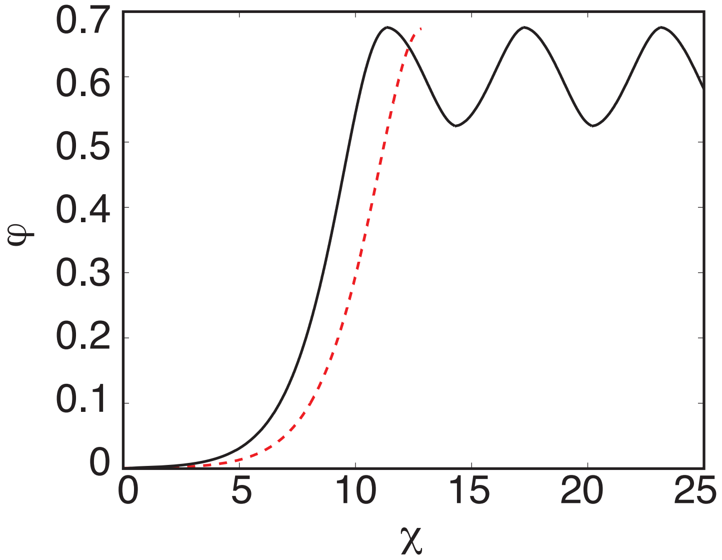

FIGURE 3.11: Electrostatic potential for $T_e = 10$ keV, $M = 1.62$, $\Theta = \Gamma = 1$ and $T_i = 0.5$ keV (solid black), $T_i = 0$ (red dashed).

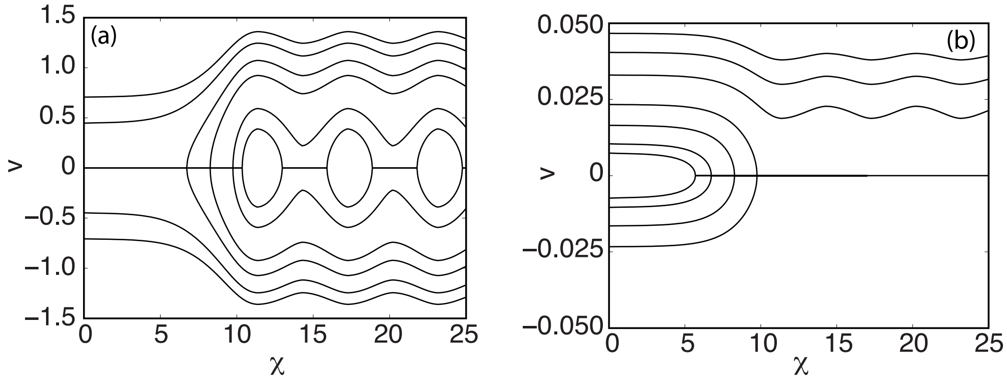

FIGURE 3.12: Electron (a) and ion (b) phase spaces for $T_e = 10$ keV, $M = 1.62$, $\Theta = \Gamma = 1$ and $T_i = 0.5$ keV.

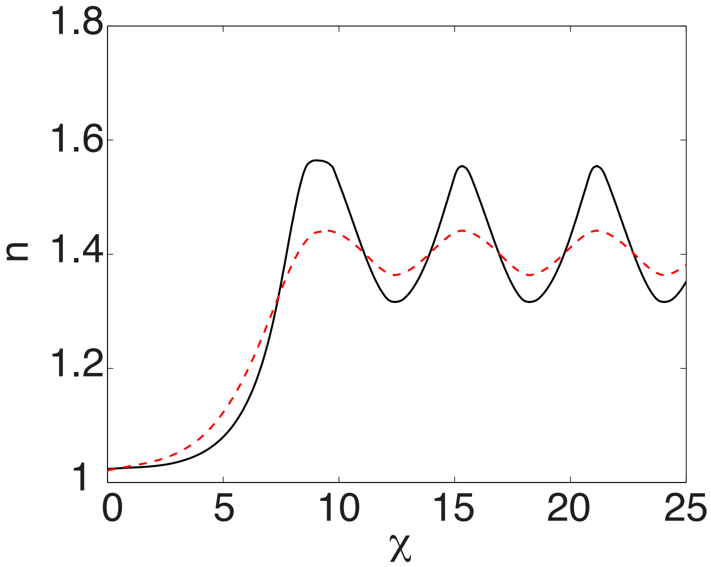

FIGURE 3.13: Spatial dependence of the ion (black, solid) and electron (red, dashed) density for $T_e = 10$ keV, $M = 1.62$, $\Theta = \Gamma = 1$ and $T_i = 0.5$ keV.

lows the trend of the electrostatic potential φ (see figure 3.13). In the upstream region, the increasing potential decelerates and accumulates the ions which leads to an increase in the density. In the downstream, the ion density oscillates around a mean value.

CHAPTER 4

ELECTROSTATIC SHOCK FORMATION AND ION ACCELERATION IN PLASMAS

The interpenetration of collisionless plasmas with different density, temperature and drift velocity leads to the generation of instabilities and to the formation of nonlinear structures that can develop into shock waves.

For a better comprehension of the physics of electrostatic shock formation, the interaction of two adjacent plasma slabs with different initial properties has been analyzed. Electrostatic instabilities develop at the interface between the plasma slabs building up an electrostatic potential. The induced wave can then evolve in an electrostatic shock wave whenever dissipation is provided by the electrons trapped behind the shock and by the ions reflected by the shock.

A series of 1D and 2D numerical simulations has been performed using the shell model and Osiris, described in chapter 2. Infinite and finite plasma slabs composed by cold ions and hot electrons have been considered. A parametric study has been conducted varying the initial density and the electron temperature of the slabs to understand the most favorable conditions for shock formation and ion reflection. The effects related to finite size plasmas have been analyzed and, with the purpose of achieving high quality ion beams, tailored plasma profiles have been considered.

4.1 SHOCK FORMATION AND ION REFLECTION IN INFINITE PLASMA SLABS

The interaction of two semi-infinite plasma slabs P_0 and P_1 composed by cold ions and hot electrons has been modeled. The initial density of the two slabs is different, with $\Gamma = n_1/n_0 = 4$, where n_0 and $n_1 = 10^{19}\,\mathrm{cm}^{-3}$ are the plasma densities of the right and left slab respectively (see figure 4.1 (a)). The initial electron temperature of the two slabs is the same, $\Theta = T_{e1}/T_{e0} = 1$, where T_{e0} and $T_{e1} = 1.5\,\mathrm{MeV}$ are the initial electron temperatures in the right and left slabs respectively. It is important to underline that in all the following simulations P_1 is always the slab with the highest density, temperature or drift velocity and will correspond to the downstream plasma once the shock is formed; as a consequence P_0 will correspond to the upstream plasma. The interface between the two slabs is situated at $x_1 = 0.03\,\mathrm{cm}$. A box with length $L_{x1} = 600\,c/\omega_p$ and width $L_{x2} = 60\,c/\omega_p$, where $\omega_p = \sqrt{4\pi e^2 n_1/m_e}$ is the electron plasma frequency in the downstream slab, has been used, together with absorbing boundary conditions for fields and particles along x_1 and periodic boundary conditions for fields and particles along x_2. A grid with 2400×240 points, corresponding to $\Delta x = \Delta y = 0.25\,c/\omega_p$ and to a time step $\Delta t = 0.175\,\omega_p^{-1}$, has been employed. In each cell 36 cubic particles for every species have been utilized. Particles have been pushed for more than 20000 temporal steps. Results are shown in figure 4.1. At early times, the denser slab P_1 starts to expand into P_0, piling up the density around the discontinuity and driving a non linear ion acoustic wave (IAW) (figures 4.1 ((b), (g), (l), (q)). With time, the wave grows, the longitudinal electric field reaches high amplitudes and ions start to get trapped, causing the formation of an ion acoustic shock wave (IASW) (see figures 4.1 (c), (h), (m) and (r)). Clear signatures of the IASW are the spike of the electric field and the peak of the density. Afterwards, the potential energy associated with the wave becomes so high that the wave starts to pick up the ions of the upstream slab and to reflect them to a velocity that is about twice the shock speed, behaving as if it was a perfectly reflecting moving wall (figures 4.1 (d), (e), (i), (j), (n), (o), (s) and (t)). The shock is moving at a constant speed $v_s \simeq 0.05\,c$, corresponding to a shock Mach number of $M_s = v_s/c_{s0} \simeq 1.34$, as shown in figure 4.2, where the position of the shock versus time has been plotted. Consequently, the average speed of the reflected ions is $v_i \simeq 2v_s \simeq 0.10\,c$, in agreement with the simulations.

A set of simulations in which the only parameter varied was Γ has been

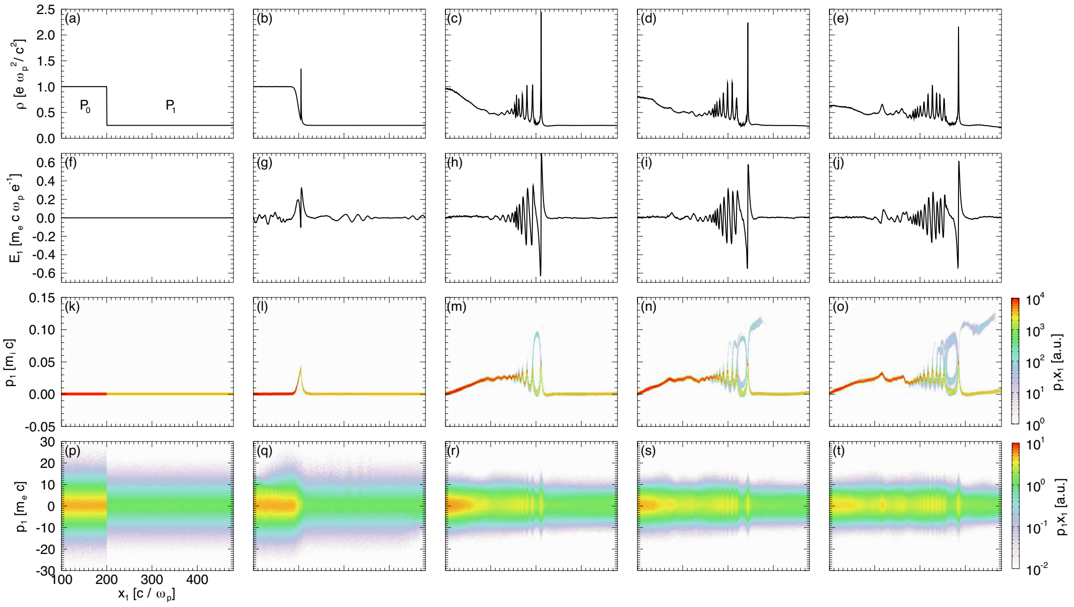

FIGURE 4.1: Shock formation and ion reflection driven by the interaction of two plasma slabs with $\Gamma = n_1/n_0 = 4$, $\Theta = T_{e1}/T_{e0} = 1$ and $T_{e0} = 1.5\,\mathrm{MeV}$. Snapshots of ion density profile ((a)-(e)), longitudinal electric field ((f)-(j)), longitudinal ion phase space ((k)-(o)) and longitudinal electron phase space ((p)-(t)) are shown at $t = 0$ ((a), (f), (k), (p)), 175 ((b), (g), (l), (q)), 2188 ((c), (h), (m), (r)), 2800 ((d), (i), (n), (s)) and 3588 ((e), (j), (o), (t)) ω_p^{-1}. Simulation performed with Osiris.

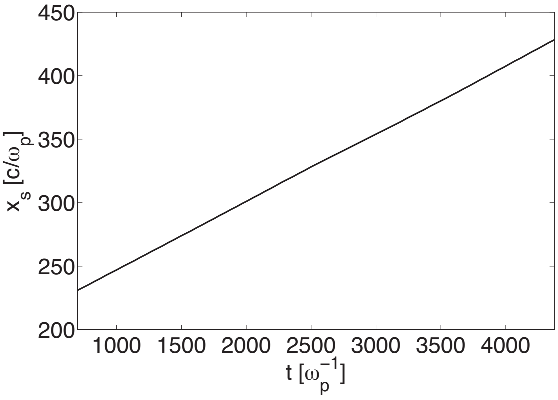

FIGURE 4.2: Shock position versus time for the same initial conditions as in figure 4.1. The shock is moving with a constant speed $v_s \simeq 0.05\,c$, corresponding to a shock Mach number $M_s \simeq 1.34$.

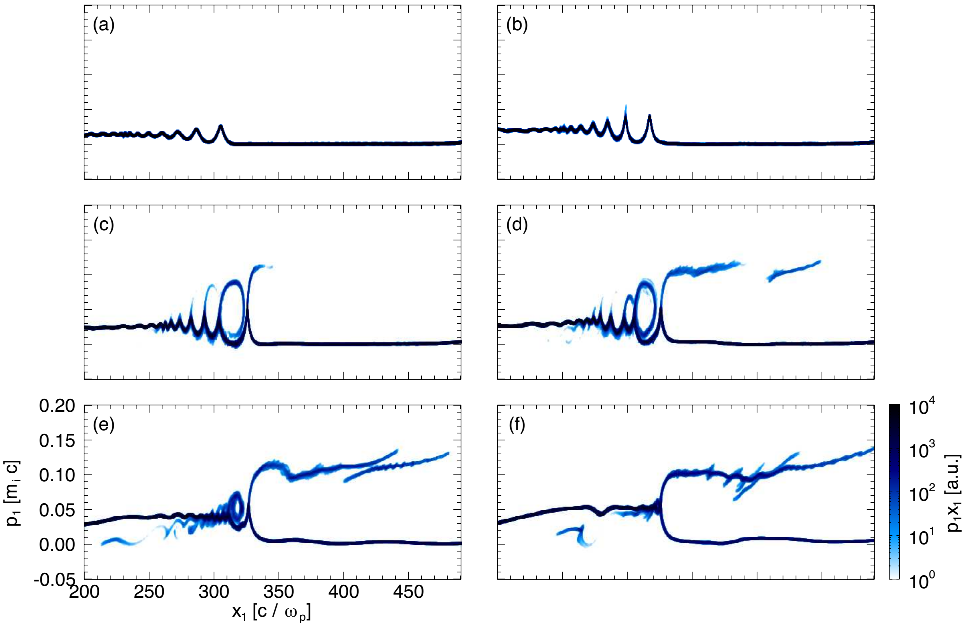

FIGURE 4.3: Ion phase space at $t = 2450\,\omega_p^{-1}$ for $\Gamma = 2$ (a), 3 (b), 4 (c), 5 (d), 10 (e) and 20 (f), $\Theta = 1$ and $T_{e0} = 1.5\,\mathrm{MeV}$. Simulations performed with Osiris.

performed in order to understand the role of the density jump in the physics of shock formation. Figure 4.3 shows the ion phase space for $\Gamma = 2, 3, 4, 5, 10$ and 20 at $t = 2450\,\omega_p^{-1}$. When the density jump between the two slabs is small ($\Gamma < 4$), the expansion of the denser slab into the more rarified one drives a non linear IAW, but the electrostatic potential associated with the wave is not strong enough to reflect the background ions (figures 4.3 (a) and (b)). When $\Gamma \geq 4$ the amplitude of the IAW gets bigger and it starts to reflect ions. In such cases, it is also possible to observe that some downstream plasma ions get trapped in the nonlinear wave that follows the shock (figures 4.3 (c), (d) and (e)). The ion trapping decreases when increasing Γ, in contrast to the ion reflection in the upstream, that increases with Γ. For very high values of Γ the ion trapping almost disappears, while the majority of the upstream ions gets reflected by the shock (figure 4.3 (f)).

In order to get ion reflection when Γ is small, it is necessary for P_1 to have a drift velocity v_{d1} towards the upstream slab. The relative drift, together with the density discontinuity, will drive a stronger wave able to reflect the upstream ions, as illustrated in figure 4.4, where the ion phase space at $t =$

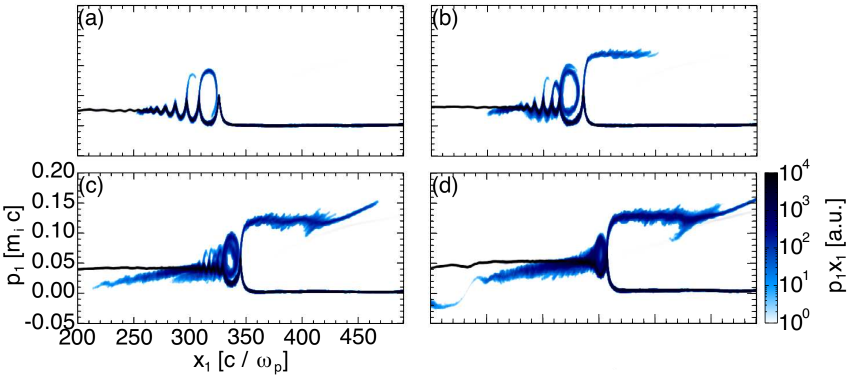

FIGURE 4.4: Ion phase space at $t = 2450\,\omega_p^{-1}$ for $\Gamma = 3$, $\Theta = 1$ and $T_{e0} = 1.5\,$MeV. The slab P_1 has a drift velocity $v_{d1} = 0.25$ (a), 0.5 (b), 1 (c) and 1.6 (d) c_{s0}. Simulations performed with Osiris.

$2450\,\omega_p^{-1}$ is reported for $\Gamma = 3$ and increasing relative fluid velocity v_{d1}. As a consequence of a small speed ($v_{d1} < 0.5\,c_{s0}$) some ions in the downstream get trapped by the non linear IAW, however the wave is still not strong enough to reflect the upstream ions (figure 4.4 (a)). When v_{d1} is bigger, the wave driven in the interaction becomes large enough to reflect the upstream ions (figure 4.4 (b)). A further increase on v_{d1} causes a stronger ion reflection and a weaker ion trapping (figures 4.4 (c) and (d)).

The effect of a temperature jump $\Theta = T_{e1}/T_{e0}$ has also been analyzed. When the initial electron temperature is the only difference between the slabs, no shocks are observed for the values of Θ tested ($\Theta = 1 - 10$). A relative drift and/or a density discontinuity are necessary to excite the waves.

In order to find the most favorable conditions for ion reflection, the relation between M_{max}, Mach number at which ion reflection occurs, Γ and Θ has been studied. Results obtained for low and high temperature electrons are reported in figure 4.5, where a small relative drift has been added when ion reflection was not directly driven by the expansion of P_1 into P_0. Simulation results are in good agreement with the theoretical ones achieved in chapter 3. When the density ratio Γ is high and the temperature ration Θ is low, ion reflection occurs for shocks with lower Mach numbers. These types of shocks are easier to drive in the laboratory which is why a high Γ and a low Θ are desirable conditions to accelerate ions. However, since the ion speed is directly proportional to the shock Mach number, the beam will have a lower energy. In order to increase

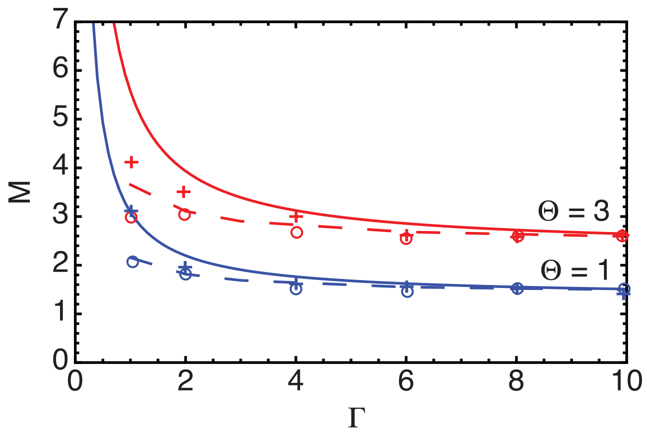

FIGURE 4.5: Maximum Mach number versus Γ for $\Theta = 1$ (blue) and 3 (red). Simulation results have been obtained considering $T_e = 1\,\text{keV}$ (+) (non relativistic) and 1.5 MeV (o) relativistic. The analytical curves deduced in chapter 3 have also been plotted.

the final energy of the beam, as $v_i \simeq 2Mc_{s0}$ and $c_{s0} \propto \sqrt{T_{e0}}$, it is then necessary to strongly heat the plasma [96].

4.2 SHOCK FORMATION AND ION REFLECTION IN FINITE PLASMAS

With the aim of moving towards more realistic scenarios, simulations employing finite plasma slabs have been performed. Two adjacent finite plasma slabs, P_1 and P_0, whose widths are 0.03 cm and 0.02 cm respectively, have been considered. The right slab P_0 is followed by a region of vacuum, as shown in figure 4.6 (a). The downstream plasma slab P_1 has a density $n_1 = 10^{20}\,\text{cm}^{-3}$ and Γ is 10. The electron temperature T_e is 1.5 MeV in both slabs. At the sharp plasma-vacuum transition, the hot electrons expanding into vacuum create a strong charge separation field (fig. 4.6 (b)), whose maximum amplitude can be estimated as [97]

$$E_{TNSA} = \frac{\sqrt{2}k_B T_e}{e\lambda_D} \tag{4.1}$$

This field is responsible to accelerate the upstream ions up to a velocity v_0. The particles will be then reflected by the further coming shock to a velocity

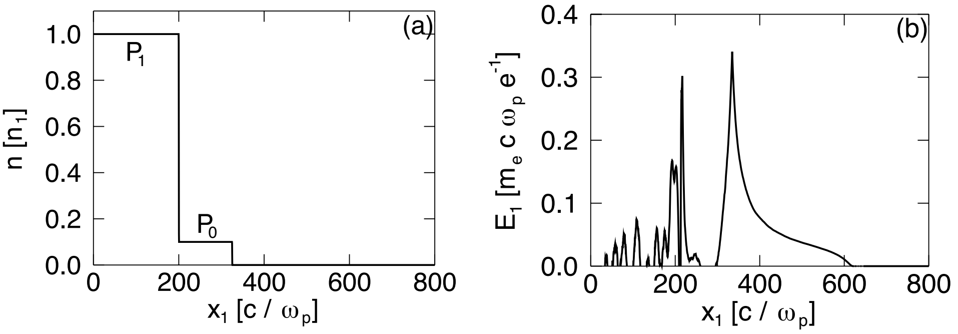

FIGURE 4.6: Shock simulation in finite plasmas with $\Gamma = 10$ for the case of an abrupt plasma-vacuum transition: initial density (a) and electric field at $t = 297.50\,\omega_p^{-1}$ (b). Simulations performed with Osiris.

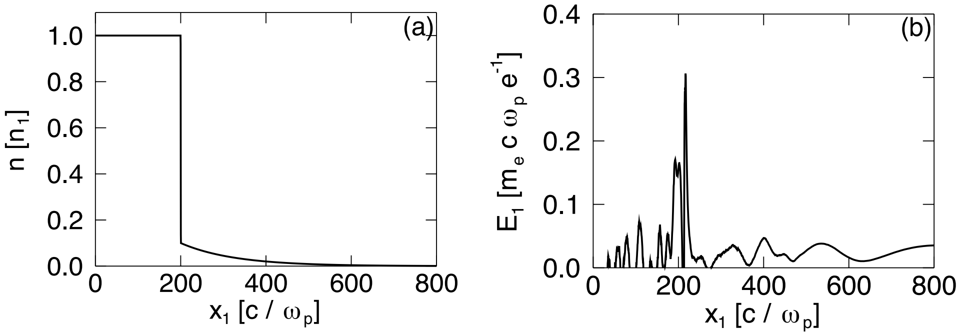

FIGURE 4.7: Shock simulation in finite plasmas with $\Gamma = 10$ for the case of a smooth plasma-vacuum transition: initial density (a) and electric field at $t = 297.50\,\omega_p^{-1}$ (b). Simulations performed with Osiris.

$v_{ions} = 2M_{cr}c_{s0} + v_0$. Since the field is not uniform, it introduces a chirp in the ion velocity [19], that will broaden the final energy spectrum as typical of TNSA mechanism, as shown in figure 4.8 (a).

The sheath field can be controlled with a smooth transition between the upstream plasma and vacuum. For instance, at early times ($t \ll 4L_g/c_{s0}$), an exponentially decreasing plasma profile with scale length L_g gives rise to a constant electric field [98]

$$E_{TNSA} = \frac{k_B T_e}{e L_g} \tag{4.2}$$

which can be decreased by choosing a large scale length L_g. This will help pre-

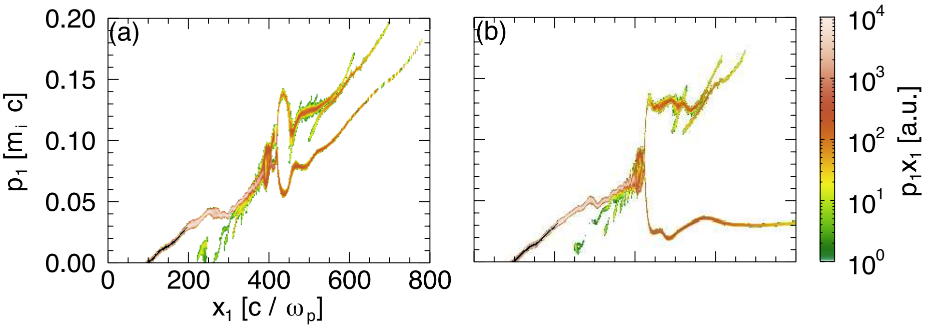

FIGURE 4.8: Ion phase space at $t = 3430\,\omega_p^{-1}$ for the case of figure 4.6 (a) and for the case of figure 4.7 (b).

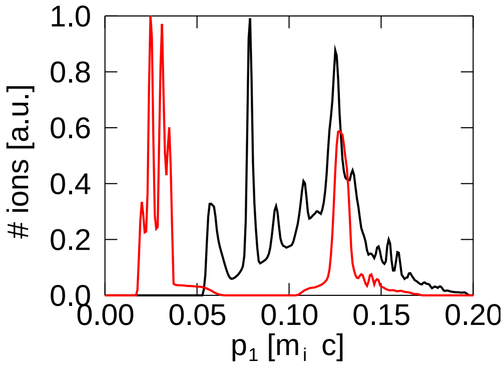

FIGURE 4.9: Ion distribution as function of the longitudinal momentum p_1 at $t = 3430\,\omega_p^{-1}$ for the case of figure 4.6 (black) and for the case of figure 4.7 (red).

serving the monoenergetic feature of the ions reflected by the shock. This can be seen in figure 4.7 (a) and (b). The sharp transition plasma-vacuum has been substituted by an exponentially decaying plasma profile with $L_g = 0.02\,\text{cm}$. The sheath field is now approximately constant and it will accelerate the ion to a uniform and lower speed. The ions are then reflected by the shock, preserving their narrow energy spread, as can be observed in figure 4.8 (b). Figure 4.9 shows the normalized ion distribution function confirming that a tailored plasma can be used for the generation of monoenergetic ion beams.

In order to get a beam with low energy spread, it is crucial to address the role of the competing accelerating fields. In particular, it is important to guarantee that the velocity of the expanding upstream ions $v_0 = c_{s0}^2 t/L_g$ [98] is small compared to the shock velocity, so that the shock can pick them up at the time that the shock is formed τ_r:

$$v_s \gg \frac{c_{s0}^2 \tau_r}{L_g} \tag{4.3}$$

For strong shocks, when ion reflection is the dominant mechanism, the ion reflection time is similar to the shock formation time. A numerical estimate of this quantity is given by Forsulnd and Shonk [86] in the case of low Mach number shocks

$$\tau_r = \frac{4\pi}{\omega_{pi}} \tag{4.4}$$

Alternatively, one can define the ion reflection time as the time that an upstream ion takes to be accelerated to $v_s = Mc_{s0}$ in the presence of the shock electrostatic field. Considering for simplicity an upstream ion at rest and a uniform electric field associated to the shock $E_s = -\Phi/L_s$ with $L_s \simeq \lambda_D$ typical width of an electrostatic shock, τ_r can be computed as [96]

$$\tau_r \simeq \frac{\lambda_D}{Mc_{s0}} = \frac{1}{M\omega_{pi}} \tag{4.5}$$

obtaining a result consistent with equation (4.4). Plugging equation (4.4) into expression (4.3), a constraint for monoenergetic ions is obtained [99]:

$$L_g \gg \frac{4\pi c_{s0}^2}{v_s \omega_{pi}} \tag{4.6}$$

Besides this condition for monoenergetic ion generation, there is a stricter one that concerns the ideal target thickness for optimal plasma heating. As it will be discussed in chapter 5, uniform heating is a key factor to generate a stable shock with constant velocity. In these simplified simulations, plasma electrons have already a homogenous temperature at the beginning of the simulations, therefore the more rigid condition does not apply directly to this fundamental configuration. However, since it imposes an upper limit on L_g, it appears important considering it at this stage (see section 5.1.1):

$$L_g \leq \frac{\pi c}{\omega_{pi}} \tag{4.7}$$

Assuming the superior limit of inequality (4.7) as the optimal L_g, theoretical predictions have been tested with numerical simulations. The interaction of

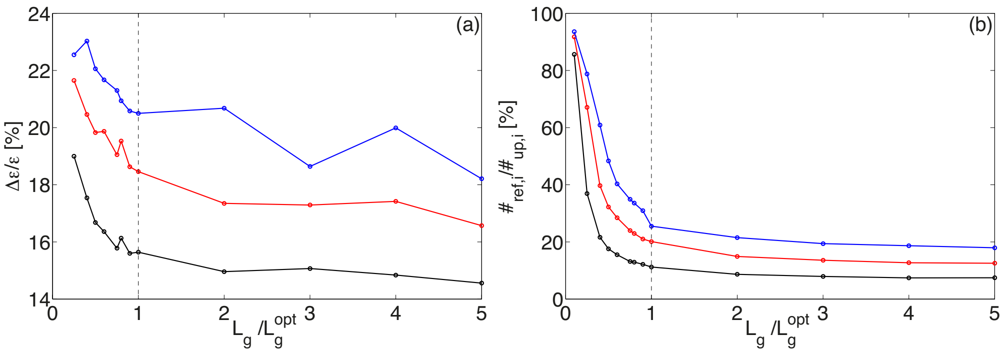

FIGURE 4.10: Upstream ion energy spread (a) and percentage of reflected upstream ions (b) versus L_g at $t = 3308$ (black), 4734 (red) and 6688 (blue) ω_p^{-1}. Simulations performed with the shell algorithm.

two plasma slabs having a longitudinal density profile as shown in figure 4.7 (a) has been considered. The slab P_1 has a width $L_1 = 0.01\,\mathrm{cm}$, a density $n_1 = 10^{19}\,\mathrm{cm}^{-3}$ and it is followed by a decreasing density profile described by

$$n_0 = \frac{n_1}{\Gamma} \exp\left(-\frac{x - L_1}{L_g}\right) \tag{4.8}$$

with $\Gamma = 10$. A detailed parameter scan varying L_g around its optimal value $L_g^{opt} = \pi c/\omega_{pi} \simeq 0.02\,\mathrm{cm}$ has been performed. Results can be seen in figures 4.10, 4.11 and 4.12.

Figure 4.10 shows the energy spread of the reflected ion beam and the percentage of reflected upstream ions for different values of L_g at different times. All the curves flatten around $L_g \simeq L_g^{opt}$, confirming the validity of the theoretical prediction 4.7. It is possible to notice that the beam energy spread increases for longer times. In fact the shock speed, constant at early times, decreases at later times. This is due to the fact that the wave is constantly transferring energy to the ions and since no plasma is injected into the simulation, it slows down as a consequence of the dissipation, as illustrated in figure 4.11 and previously noted in [100]. The speed of the reflected ions is then no longer constant and a chirp is introduced in the ion spectrum, that causes the energy spread to increase. It is also interesting to observe that the deceleration of the shock wave depends on L_g. Right after the shock is formed, it starts to move with the same speed, regardless of the decaying scale length, however, when ion reflection gets important, at around $t = 1000\,\omega_p^{-1}$, it starts to loose energy

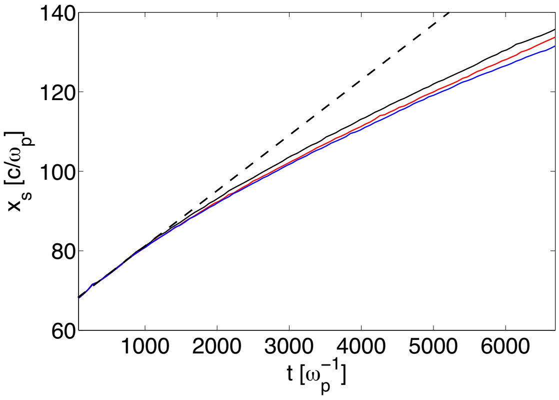

FIGURE 4.11: Shock speed versus time for $L_g = L_g^{opt}$ (black), $5L_g^{opt}$ (red), and $20L_g^{opt}$ (blue). Simulations performed with the shell algorithm.

and, therefore, it decelerates with a rate that increases with L_g, in agreement with the model for soliton-like laser pulses propagating in inhomogeneus plasmas presented in [101].

Figure 4.12 shows the energy spread of the reflected ion beam and the percentage of reflected upstream ions versus L_g for different initial values of electron temperature at $t = 3308\,\omega_p^{-1}$. Also in this case, all the curves show the same trend and suggest that the upper limit (4.7) on L_g, which is critical in laser driven ion acceleration but of no importance in this fundamental configuration, will not prevent to obtain a much lower energy spread, since the minimum value of $\Delta\varepsilon/\varepsilon$ is reached around $L_g = L_g^{opt}$. Moreover, as predicted by the theory, numerical simulations indicate that the optimal decay length does not depend on the initial electron temperature.

4.3 SHOCK FORMATION AND ION REFLECTION IN MULTILAYER PLASMAS

A key factor for the generation of monoenergetic ions is represented by the reduction of the fields that build-up at the interface between plasma and vacuum. As seen in section 4.2, this is achieved when the upstream plasma has the required exponentially decaying density profile.

With the purpose of exploiting the information on shock formation ac-

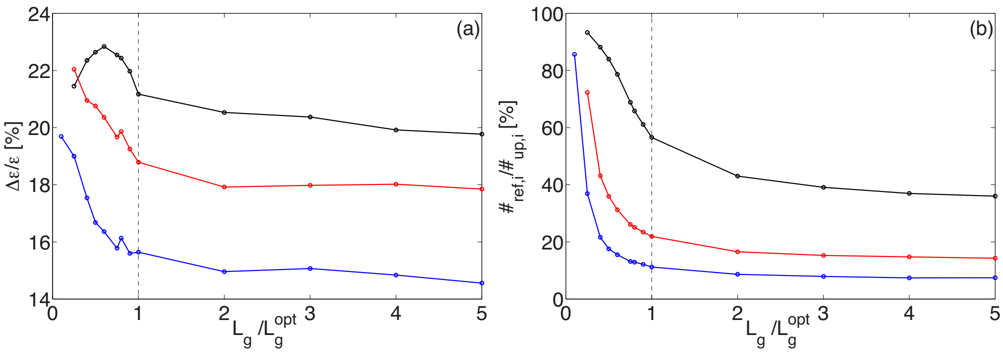

FIGURE 4.12: Upstream ion energy spread (a) and percentage of reflected upstream ions (b) versus L_g at $t = 3308\,\omega_p^{-1}$ for $T_e = 0.08$ (blue), 0.2 (red) and 0.5 (black) MeV. Simulations performed with the shell algorithm.

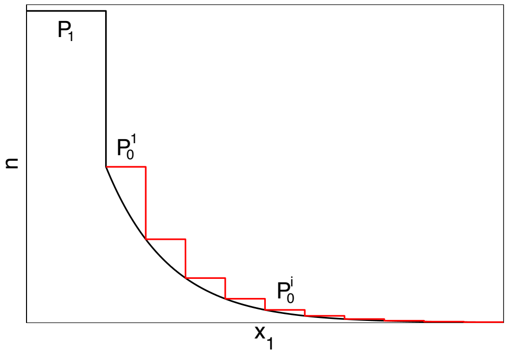

FIGURE 4.13: Sketch of the multilayer plasma considered in the simulations of section 4.3.

quired modeling the interaction of two ideal plasma slabs for the generation of shocks in laboratory, it has been realized that the conditions described in section 4.2 may not be so straightforward to reproduce. For this reason, the possibility of using several plasma slabs with progressively decreasing density to mimic the exponential profile of equation (4.8) has been tested. The idea of coupling micro or nano layers of various materials having different density has been already explored in the contest of TNSA acceleration [102, 103]. For the first time, such an engineered approach is explored in the context of shock

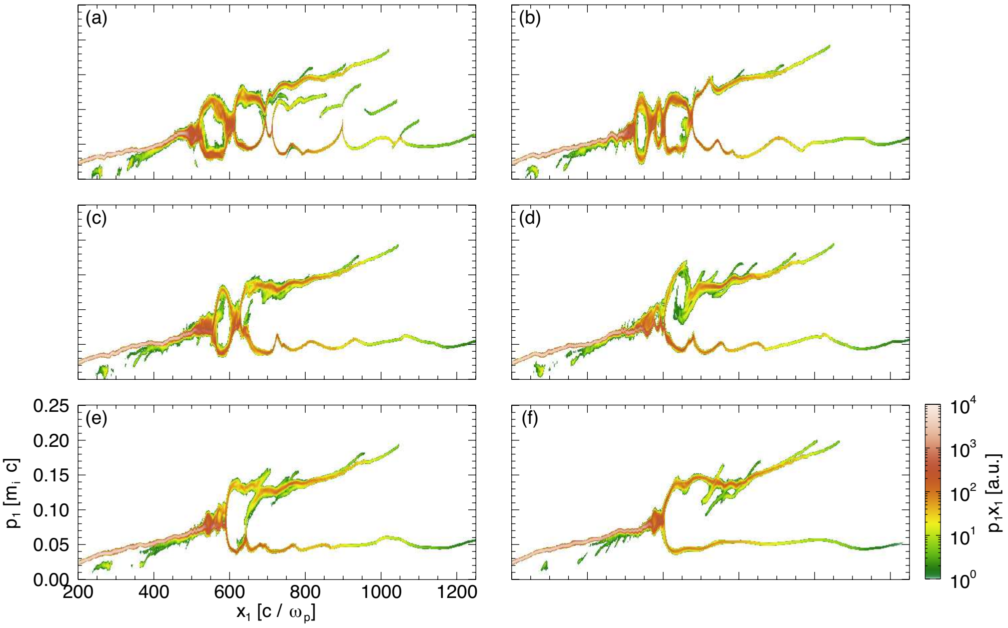

FIGURE 4.14: Ion phase space generated in the interaction between a plasma slab P_1 and a plasma P_0 composed by several layers with thickness $L_0^i = 0.035$ (a), 0.025 (b), 0.022 (c), 0.018 (d) and 0.015 (e) cm. (f) Ion phase space for density profile of P_0 according to equation (4.8). Simulations performed with Osiris.

acceleration.

Numerical simulations in which the upstream plasma P_0 has been replaced by several plasma layers P_0^i with decreasing density (as shown in figure 4.13) have been performed. The slab P_1 is 0.03 cm long and has a density of $n_1 = 10^{19}\,\text{cm}^{-3}$. The density ratio Γ between P_1 and P_0^1 is 10. The length of the layers following P_1 and their density have been varied. Figure 4.14 shows the ion phase space at $t = 5600\,\omega_p^{-1}$ for an upstream plasma with density given by equation (4.8) with $L_g = L_g^{opt} = 0.02\,\text{cm}$ and for an upstream plasma composed by several layers with lengths $L_0^i = 0.035$, 0.025, 0.022, 0.018 and 0.015 cm, corresponding to a density ratio Γ_0^i between two contiguous layers P_0^i of 5.4, 3.3, 2.8, 2.3 and 2 respectively. The density discontinuity triggers the generation of non linear structures at the interfaces between the layers. These structures are stronger for higher Γ_0^i and can lead to the generation of smaller, secondary shock waves, that reflect the upstream ions and give rise to ion trapping, as can be seen in figures 4.14 (a)-(c). Their presence degrades the quality

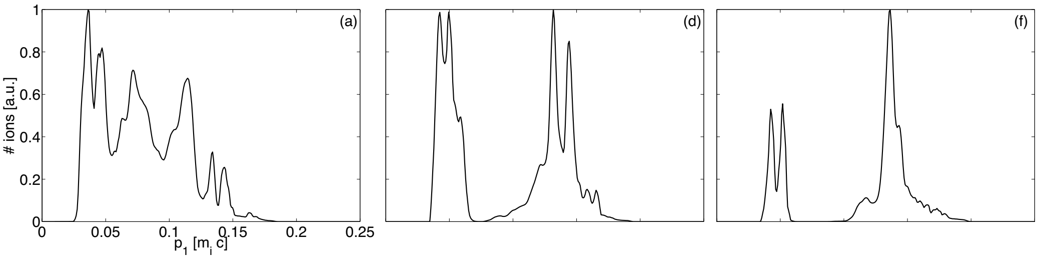

FIGURE 4.15: Ion momentum distribution for the case of figure 4.14 (a), (d) and (f)

of the accelerated ion beam, whose spectrum is no longer monoenergetic. For smaller values of Γ_0^i, modulations in the upstream still occur (figures 4.14 (d) and (e)), but their influence on the property of the reflected ions is weak. Figure 4.15 shows the ion distribution for the cases of figure 4.14 (a), (d) and (f). While in the case of figure 4.15 (a), the ion energy spectrum is wide, in the case of figure 4.15 (d), two peaks corresponding to the expanding upstream and to the reflected ions, can be clearly identified. The spectrum looks very similar to the one of figure 4.15 (f) obtained with the exponentially decaying profile. The energy spread is measured to be around 10% in both cases, showing that multilayer plasmas can be a promising alternative to achieve a high quality ion beam, provided that the density discontinuity between two contiguous layers is small ($\Gamma_0^i \leq 2.5$).

CHAPTER 5

LASER-DRIVEN ELECTROSTATIC SHOCKS

As seen in chapter 4, two requirements are necessary to drive strong shock waves in plasmas capable to accelerate ions: a density discontinuity and/or a relative drift inside the plasma. They can be practically achieved in the interaction between an intense laser pulse and a plasma target. However the laser and the plasma parameters need to be accurately tuned to improve the quality of the generated ion beam. For instance, as stated in section 4.1, a strong electron heating is fundamental to reach high energy. For this reason, a near critical density plasma is preferable. In this case, the pulse can interact with the majority of the target, transferring a huge fraction of its energy to the plasma electrons [96]. Moreover, as observed in section 4.2, a smooth transition plasma-vacuum at the back of the target is essential to preserve the monoenergetic features of the ion beam. Such condition can be obtained by means of a slow and controlled expansion of the target, as a consequence of the pre-heating due to the laser pre-pulse or due to a low intensity pulse before the main one [99]. A valid alternative to this scheme is the use of multi-layer targets, tailored in a way to reproduce the suitable density profile, as found in section 4.3.

5.1 SHOCK FORMATION AND ION REFLECTION IN LASER-PLASMA INTERACTION

In order to understand the role of the laser in shock formation, 2D Osiris simulations have been performed. The parameters of the CO_2 laser available at University of California at Los Angeles [104] have been used. The pulse has intensity $I \simeq 10^{17}\,\mathrm{W/cm^2}$, wavelength $\lambda_0 = 10\,\mu\mathrm{m}$ and frequency $\omega_0 = 2\pi c/\lambda_0 = 0.2\,\mathrm{fs}^{-1}$. The normalized vector potential associated to the wave is then $a_0 = eE_0/m_e c\omega_0 \simeq 0.85\sqrt{I\,[\mathrm{W/cm^2}]\lambda^2\,[\mu\mathrm{m}]/10^{18}\,[\mathrm{W/cm^2}]} = 2.5$. The pulse is modeled as a plane wave polarized in the plane (p-polarization) with a gaussian like polynomial profile in the longitudinal direction, whose envelope is defined as $f(\hat{t}) = 10\hat{t}^3 - 15\hat{t}^4 + 6\hat{t}^5$ being $\hat{t} = \sqrt{2}t/\tau$, where $\tau = 14\,\mathrm{ps}$ is the laser pulse duration at FWHM. The pulse interacts with a pre-formed cold electron-proton plasma having a longitudinal density profile described by

$$n = \begin{cases} \dfrac{a_0 n_c}{16\lambda_0}(x - 16\lambda_0) & \text{for} \quad x \le 16\lambda_0 \\[2ex] a_0 n_c \exp\left(-\dfrac{x - 32\lambda_0}{L_g}\right) & \text{for} \quad x > 32\lambda_0 \end{cases} \tag{5.1}$$

where $n_c \simeq 10^{19}\,\mathrm{cm}^{-3}$ is the critical density, so that $\omega_0 = \omega_p = \sqrt{4\pi e^2 n_c/m_e}$ and $L_g \simeq 20\,\lambda_0$ [20]. The critical density n_c has been multiplied by a_0 to take into account the relativistic self-induced transparency [105]. A simulation box with size $2500 \times 120\,(c/\omega_p)^2$ and a grid of 10000×480, corresponding to a spatial step $\Delta x = \Delta y = 0.25\,c/\omega_p$ and a temporal step $\Delta t = 0.175\,\omega_p^{-1}$, have been used. The boundary conditions have been chosen to be absorbing in the longitudinal direction and periodic in the transverse, both for particles and fields. In each cell 64 computational particles for each species have been placed and cubic interpolation has been utilized. Particles have been pushed for more than 80000 time steps. Results are illustrated in figure 5.1. The laser interacts with the portion of the target with density smaller than the critical one. When it reaches the density peak, it corrugates the target surface and it causes the density to steep, reaching values up to 4 times the original ones (figures 5.1 (a), (b), (f), (g)). A strong electron heating occurs at the front of the target (figure 5.1 (p)). The hot electrons expand toward the unperturbed plasma and a return current is set up due to the current imbalance. The cold electrons are dragged back towards the laser by the strong electric field, as can be seen in figure 5.1

(q), where a population of electrons with negative momentum is clearly visible. As a consequence of the electron recirculation, all the target is strongly and uniformly heated up as can be seen in figure 5.1 (r). The small separation field due to the hot electrons at the back of the target accelerates the upstream ions initially at rest to a velocity $v_0 \simeq 0.04\,c$ (figure 5.1 (w)). As seen in chapter 4, both the density steepening and the relative drift contribute to form the shock. The shock structure is characterized by a localized electric field and by a density discontinuity at the shock front (figures 5.1 (c), (h), (m)). Once the shock is formed, it starts to propagate towards the right and it starts to reflect the upstream ions that have kinetic energy smaller than the potential energy associated to the shock (figure 5.1 (w)). At later times, the shock has reflected and accelerated a big portion of the upstream ions, as can be observed in figure 5.1 (y). The electron temperature has been measured at $t = 3528\,\omega_p^{-1}$, when the electron phase space clearly indicates that the refluxing of the electrons has stopped and the thermal spread looks quite uniform all over the target, as can be seen in figure 5.2 (a), where the electron distribution function $f(\gamma)$ is shown. The distribution function has then been fitted with a relativistic Maxwellian of the form

$$f(\gamma) = C\gamma\sqrt{\gamma^2 - 1}\exp(-\mu\gamma) \tag{5.2}$$

where γ is the Lorentz factor, $\mu = m_e c^2/k_B T_e$ and $k_B T_e$ has been evaluated to be around 1.1 MeV, corresponding to $c_{s0} = 0.03\,c$. The shock speed v_s has been mesaured as $0.11\,c$ (see figure 5.3), leading to a Mach number of 2.3. The upstream ion energy spectrum at $t = 14896\,\omega_p^{-1}$ is reported in figure 5.2 (b). The shock accelerated ions have an average energy of 16 MeV and an energy spread of 14%. As can be seen in figures 5.1, the shock has a width much smaller than $10\,c/\omega_p$. The shock length is then of the same order of λ_D and much smaller than the mean free path for electron-electron and ion-ion collisions, clearly indicating that the shock is not mediated by particle collisions.

5.1.1 TARGET DECAYING LENGTH IMPACT ON LASER-DRIVEN ION SHOCK WAVE ACCELERATION

As anticipated in section 4.2, a uniform electron temperature represents a necessary factor to generate shocks having uniform speed and therefore able to accelerate ions with low energy spread. That is why the initial phase of

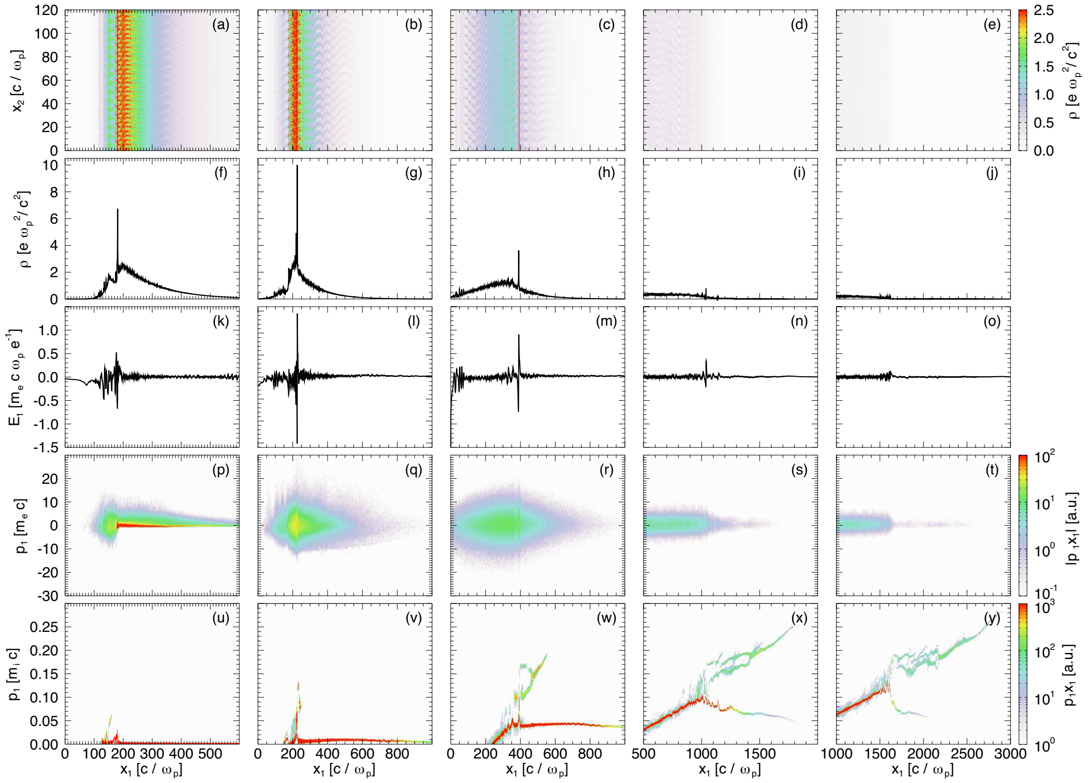

FIGURE 5.1: Shock formation and ion acceleration driven by a laser pulse with $a_0 = 2.5$ interacting with a near critical density plasma. Snapshots of the ion density ((a)-(e)), of the ion density integrated along x_2 ((f)-(j)), of the longitudinal electric field ((k)-(o)), of the electron ((p)-(t)) and the ion ((u)-(y)) longitudinal momentum at $t = 1960$, 2940, 4900, 10584, 14896 ω_p^{-1} (first, second, third, fourth and fifth column, respectively).

the laser interaction with plasma is very crucial. It is necessary that the electrons heated by the laser at the plasma surface recirculate in the target uniforming the temperature before ion reflection actually occurs. This means that the shock formation time, that for strong shocks coincides with the reflection time τ_r, has to be longer than the recirculation time [19]:

$$\tau_r > 2N_{rc}\frac{L_{target}}{v_{rc}} \tag{5.3}$$

with $N_{rc} \geq 1$ number of recirculation cycles, L_{target} length of the target and $v_{rc} \simeq c$ recirculation speed. Considering a critical plasma and using expression

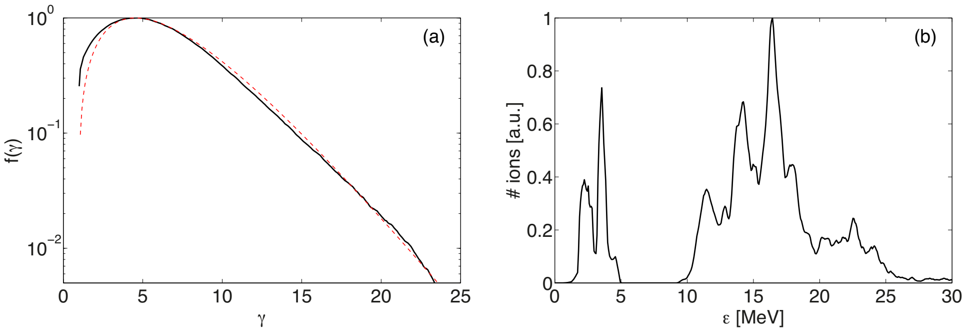

FIGURE 5.2: Electron distribution function $f(\gamma)$ at $t = 3528\,\omega_p^{-1}$ (a) and upstream ion energy spectrum at $t = 14896\,\omega_p^{-1}$ (b) for the same case of figure 5.1. The electron distribution has been fitted to the Maxwell-Jüttner distribution function $f(\gamma) = C\gamma\sqrt{\gamma^2 - 1}\exp(-\mu\gamma)$, with $\mu = m_e c^2/k_B T_e$ and $k_B T_e = 1.1\,\text{MeV}$. Ions are accelerated to an average energy of 16 MeV and an energy spread of 14%

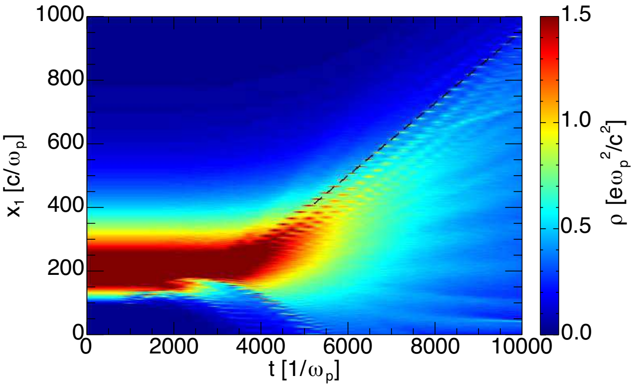

FIGURE 5.3: Ion density averaged over x_2 versus time. The black dashed line indicates the shock position. The speed of the shock has been measured to be $0.11\,c$.

(4.4), an estimate for L_{target} is obtained

$$L_{target} < \sqrt{\frac{m_i}{m_e}}\lambda_0 \tag{5.4}$$

As noted in section 4.2, it is important to maximize the scale length at the back of the target to get a good control over the TNSA field that develops at the plasma-vacuum interface (see equation (4.6)). Therefore the target thickness should be the maximum allowed. Supposing that the decaying profile is due to a symmetric target expansion ($L_{target} \simeq 2L_g$), the optimal decaying length can be evaluated as

$$L_g^{opt} \simeq \frac{\lambda_0}{2}\sqrt{\frac{m_i}{m_e}} \tag{5.5}$$

A set of simulations employing the same parameters as in figure 5.1, but with different values of L_g have been performed. Figure 5.4 shows the ion phase space at $t = 13720\,\omega_p^{-1}$. When $L_g \ll L_g^{opt}$ (figure 5.4 (a)), the TNSA field is dominant and the ion spectrum is wider (the ions are accelerated to an average energy of 25 MeV with an energy spread of about 30% for $L_g = L_g^{opt}/2$). For $L_g \gg L_g^{opt}$ (figure 5.4 (b), (c)), the laser cannot heat the whole plasma. The induced shock is slower and therefore the energy of the reflected ions is lower (the average energy is about 16, 2.1 and 0.5 MeV for $L_g = 1$, 2 and $4\,L_g^{opt}$ respectively). The ion energy spread is of the same order of L_g^{opt} ($\Delta\varepsilon/\varepsilon \leq 15\%$), while the charge of the beam decreases (the fraction of reflected particles compared to the total amount of ions in the upstream is 10, 0.04 and 0.03% for $L_g = 1$, 2 and $4\,L_g^{opt}$ respectively). These results, similar to the ones achieved in section 4.2, where the shock was driven by a density jump in the plasma, confirm that theoretical prediction about L_g^{opt} are valid also for laser-driven shocks.

5.1.2 LASER POLARIZATION IMPACT ON LASER-DRIVEN ION SHOCK WAVE ACCELERATION

The effect of laser polarization has been tested in the 2D configuration. Results comparing the electron distribution function $f(\gamma)$ at $t = 3528\,\omega_p^{-1}$ and the ion energy spectrum at $t = 14896\,\omega_p^{-1}$ for the cases of a pulse linearly polarized in the plane (p-polarization), out of the plane (s-polarization) and of a circularly polarized laser are shown in figure 5.5. A p-polarized laser can directly

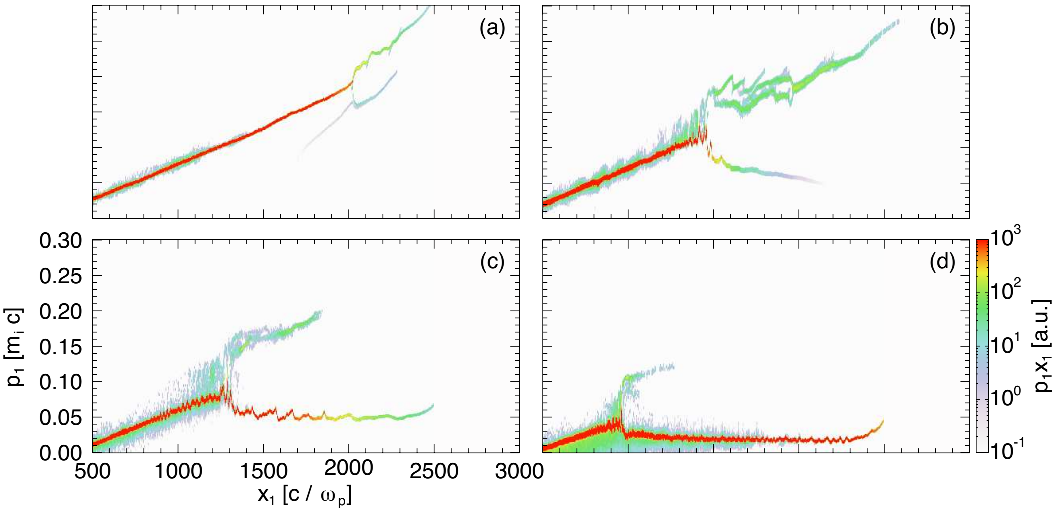

FIGURE 5.4: Ion phase space at $t = 13720\,\omega_p^{-1}$ for $L_g = 0.5$ (a), 1 (b), 2 (c) and $4\,L_g^{opt}$ (d). Smaller values of L_g allows for higher ion energy, but the spectrum is broader. Better results in term of low energy spread are obtained with larger values of L_g.

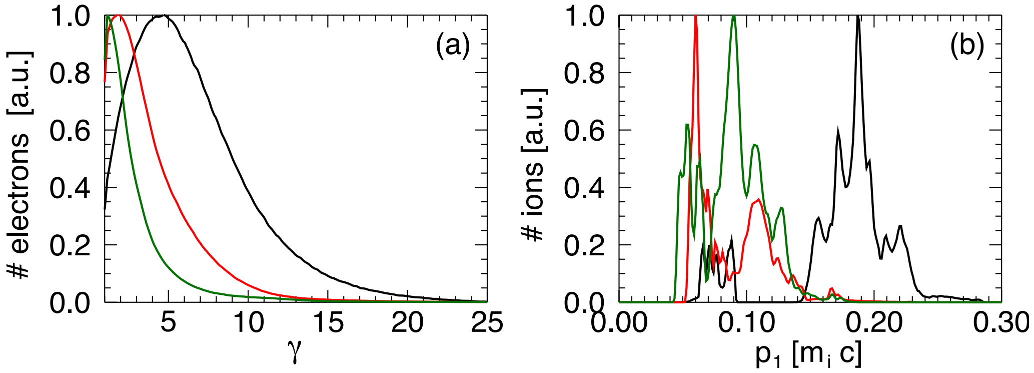

FIGURE 5.5: Electron distribution function $f(\gamma)$ at $t = 3528\,\omega_p^{-1}$ (a) and upstream ion energy spectrum at $t = 14896\,\omega_p^{-1}$ (b). The black curves have been obtained with a laser pulse linearly polarized in the plane (p-polarization), the red ones with a pulse linearly polarized out of the plane (s-polarization) and the green ones with a circularly polarized laser.

drive the electrons in the $x - y$ plane across the density gradient, resulting in a better coupling of this kind of pulse with the plasma electrons [106]. As a consequence, the absorption coefficient of the laser increases [107] and the electron heating is enhanced, resulting in higher electron temperatures. This leads to the generation of a more stable shock moving with a faster and more uniform speed. Therefore, ions are reflected and accelerated by the shock structure to higher energy and with lower spread, as can be seen in figure 5.5 (b). It is possible to speculate that, while in reality, the difference between p and s polarization will not be so pronounced and the final results will be a mixture of the two cases, a circularly polarized pulse is completely ineffective. The absence of the component of the laser electric field perpendicular to the target surface and the oscillating part of the ponderomotive force annihilate most of the electron heating processes [11] ($\mathbf{j} \times \mathbf{B}$ heating [10], resonance absorption [108] and vacuum heating [109]). As a result, the electron temperature is lower and the generated shock is weaker.

5.1.3 ELECTRON HEATING AND ION ENERGY SCALINGS WITH a_0

The dependence of the electron temperature and, consequently, of the ion energy on the laser intensity has been object of study in [96] and results will be summarized here. Simulations have been performed for increasing values of a_0. The optimal plasma profile (equation (5.1)) has been considered; the peak density has been increased with the intensity to compensate for the relativistic transparency.

For high intensity and steep density profile at the laser-plasma interaction region, the electron temperature scaling with a_0 is expected to be close to ponderomotive [107]:

$$T_e = m_e c^2 \left(\sqrt{1 + \frac{a_0^2}{2}} - 1 \right) \tag{5.6}$$

As can be seen in figure 5.6 (a), simulations clearly show that $T_e \propto a_0$. In particular, an empirical law has been deduced equating the electron energy density

$$u_e = 3 a_0 n_c L_{target} k_B T_e \tag{5.7}$$

to the absorbed laser energy density

$$u_l = \eta I \tau \tag{5.8}$$

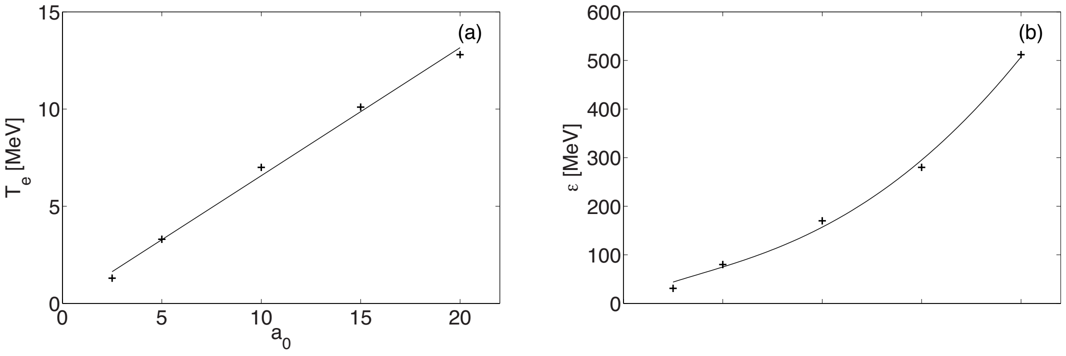

FIGURE 5.6: Electron temperature (a) and ion energy (b) for increasing laser amplitude a_0. A plane wave has been considered.

being $\eta \simeq 0.5$ the laser absorption efficiency. The electron temperature dependence on a_0 is then computed as [99]

$$T_e[\mathrm{MeV}] = 0.02\eta a_0 \frac{\tau\,[\mathrm{ps}]}{L_{target}\,[\mathrm{mm}]} \tag{5.9}$$

Figure 5.6 (b) shows the ion energy scaling with a_0. The simulation points have been fitted with the following function

$$f(a_0) = \alpha a_0 + \beta a_0^{3/2} + \gamma a_0^2 \tag{5.10}$$

where the first and second term are connected with the shock acceleration, which is the dominant process for low values of a_0 and the third represents the contribution of the upstream ion expansion, that becomes important at high values of a_0 [99].

In order to understand if the same scaling laws are valid in more realistic scenarios, simulations using a finite spot size laser have been performed. A pulse with a Gaussian transverse profile and a focal spot diameter $2w_0 = 10\,\mu$m has been used.

When a finite spot size laser is used, the shock front has a curvature. The acceleration occurs at an angle and the ion beam will have a certain divergence. As a result, the ion beam will present a bigger energy spread. Figure 5.7 shows a detail of the interaction area for a plane wave and for a pulse with a finite spot size. The interaction region looks pretty different in the two cases. While the plane wave is not stopped by the target, the finite spot size pulse can penetrate

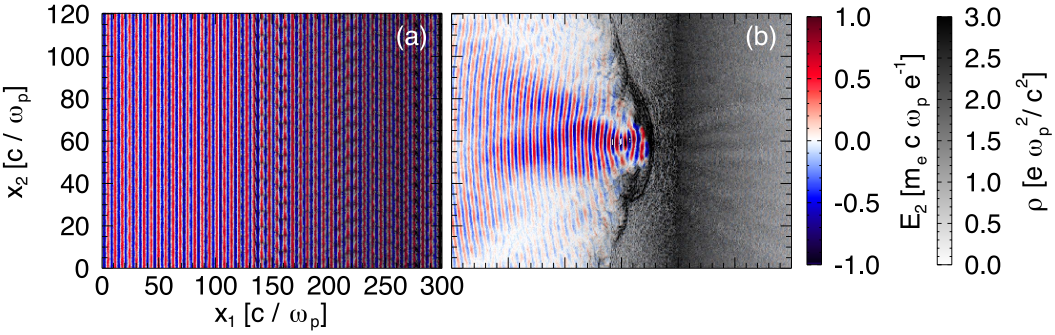

FIGURE 5.7: Details of the zone of interaction between the pulse and and the plasma in the case of a plane wave (a) and of a finite spot size pulse (b). Transverse electric field and ion density at $t = 3920\,\omega_p^{-1}$ are shown.

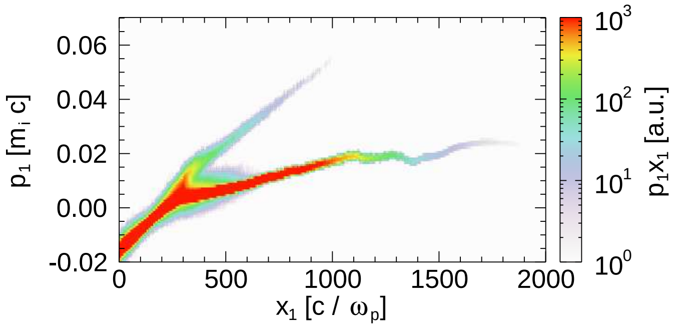

FIGURE 5.8: Ion phase space at $t = 19600\,\omega_p$. A finite spot size pulse with $a_0 = 2.5$ and $2w_0 = 10\,\mu$m has been used to drive the shock.

only the under-dense region. When it reaches the critical density, it cannot proceed further. At this point the pressure exerted by the laser contributes in pushing the plasma inwards preferentially at the center of the focal spot, a phenomenon called hole boring. The hole boring contributes in increasing the laser absorption coefficient benefiting the electron heating [106]. Moreover, the steepening of the density profile due to the intense radiation pressure, creates the density jump necessary to trigger the shock. Figure 5.8 shows the ion phase space, confirming that the ion beam is not collimated.

Electron temperature and ion energy have been measured. Results are reported in figures 5.9 and 5.10. The electron distribution function indicates the the electron temperature is not uniform (figure 5.9 (a)). There are, indeed, a

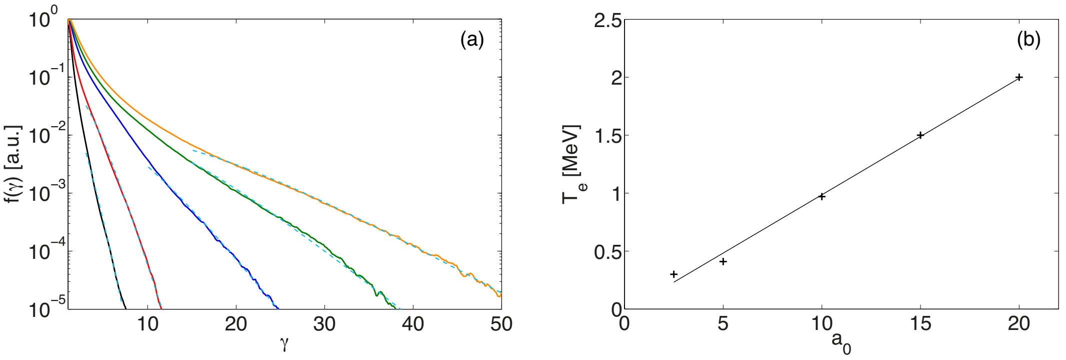

FIGURE 5.9: (a) Electron distributions at $t = 5488\,\omega_p^{-1}$ for $a_0 = 2.5$ (black), 5 (red), 10 (blue), 15 (green) and 20 (orange). The pulse has a finite spot size $w_0 = 3\,\lambda_0$. The distributions show the presence of a cold and of a hot electron component. The hot electron distributions have been fitted to 3D Maxwell-Jüttner distribution (light blue dashed lines). (b) Scaling of the electron temperature with the laser amplitude a_0.

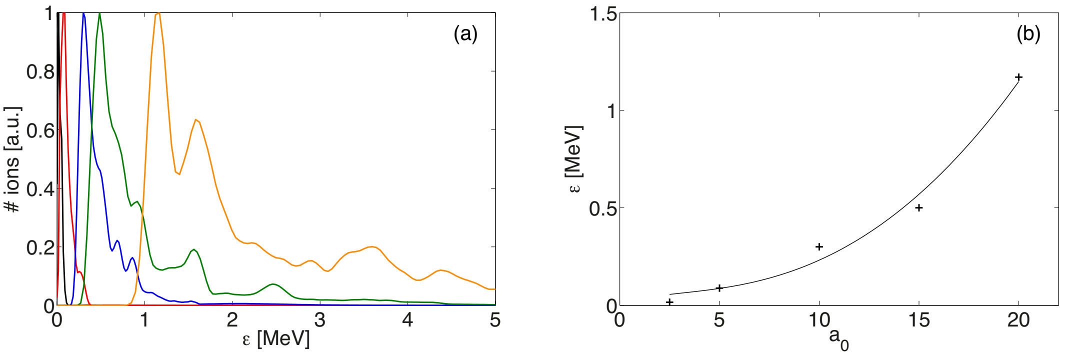

FIGURE 5.10: (a) Upstream ion energy spectra at $t = 10192\,\omega_p^{-1}$ for the same cases of figure 5.9. (b) Scaling of the ion energy with the laser amplitude a_0.

group of hot electrons and a group of cold ones. This is due to the fact that the region where the laser interacts with the target is smaller and there are portions of the target not directly heated up by the laser. The hot electron distributions have been fitted to a 3D relativistic Maxwellian (equation (5.2)). Figure 5.9 (b) shows that, also when a finite spot laser is used, the temperature scales linearly with a_0. Figure 5.10 (a) reports the ion energy spectra at $t = 10192\,\omega_p^{-1}$ for different a_0. The scaling on the average ion energy versus different values of a_0 can be seen in figure 5.10 (b). Simulation points have been fitted with equation 5.10, showing that plane wave scalings can be retrieved in realistic scenarios.

It is possible to notice that, also in this case (see figure 5.10 (a)), the ion expansion contribution in the acceleration process becomes more important for high laser intensities and causes the spectrum to broaden.

Part II

Ion acceleration in Coulomb explosion

CHAPTER 6

COULOMB EXPLOSION OF HETERO-NUCLEAR CLUSTERS

The interaction of ultraintense ($I > 10^{16}\,\mathrm{W/cm^2}$) and ultrafast ($\tau = 10 - 100\,\mathrm{fs}$) laser pulses with gases composed by clusters (microscopic aggregations of $10^2 - 10^7$ atoms bounded together by Van der Waals forces, whose shape is approximately spherical [110]) leads to the formation of completely ionized nanoplasmas [30]. Depending on the laser and on the cluster characteristics, different scenarios can take place ranging from hydrodynamic expansion of quasi-neutral plasmas [111–113] to Coulomb explosion of pure ion clouds [26, 114, 115].

Coulomb explosion is a well known mechanism of ion acceleration [116]. It occurs when all the electrons are stripped away instantaneously from the cluster. In this case, a cloud composed only by positively charged ions is left behind and the Coulomb repulsive forces cause its explosion. Studies on Coulomb explosion dynamics are relevant not only for plasma physics in general, but also for fusion research [22,23] and imaging by "diffraction before destruction" [24]. This chapter will be devoted to investigate Coulomb explosion in composite clusters consisting of different atomic species. The focus is on heavy-light systems made of hydride molecules composed of C, H, N and O, in order to collect valuable information for coherent diffractive imaging [117].

6.1 COULOMB EXPLOSION OF A CLUSTER COMPOSED BY TWO ION SPECIES

When clusters are irradiated by intense pulses, three different processes are going to happen: matter gets ionized in a phenomenon usually referred to as inner ionization, the free electrons heated by the laser start to escape the cluster in what is called outer ionization [118] and finally the massive positive cloud left behind expands under the effect of the pressure exerted by the hot electrons and the Coulomb repulsive forces. The two latter are usually concurrent: when the first one prevails, the cluster undergoes a hydrodynamic expansion, while, in the other case, the cluster will simply explode.

In many realistic conditions, there is no need to model the inner ionization process: usually the laser pre-pulse is sufficient to completely ionized the target and the nanoplasma approximation can be adopted [30, 119]. However, a self-consistent treatment of the free electron dynamics is generally required to correctly model the cluster expansion. Nevertheless, there are scenarios where the electron dynamics can be ignored: this is the Coulomb explosion or cluster vertical ionization case [27, 120]. When the initial radius of the cluster R_0 is smaller than both the electron skin depth $\delta_e = c/\omega_p$ and the electron excursion length $\xi_e \simeq x_m$, where x_m is the maximum oscillation amplitude of an electron in a ponderomotive field, the totality of the cluster electrons are indeed cast away before the ions move significantly. The outer ionization is occurring much faster than the bulk expansion and the ion dynamics does not depend on the electrons [121]. That is why pure Coulomb explosion scenarios can be modeled neglecting electrons.

6.1.1 SHELL MODEL SIMULATIONS

A pure ion sphere of initial radius $R_0 = 38\,\text{Å}$ composed by $N_0 \simeq 450000$ ions for an initial density of $n_0 = 2 \times 10^{24}\,\text{cm}^{-3}$ has been modeled. The cluster is constituted by a mix of 70% Carbon ions ionized once and 30% Hydrogen ions, so that $\beta = m_C/m_H = 12$, $\Theta = q_C/q_H = 1$ and $\alpha = N_H/N_0 = 0.3$ where m and q are the mass and the charge of the ions, N is the number of ions and the subscripts H and C stand for Hydrogen and Carbon, respectively. At the initial time, ions are at rest and uniformly distributed in the sphere. A $\Delta t = 0.002\sqrt{4\pi R_0^3 m_e/3e^2 N_0}$ has been used and particles have been pushed

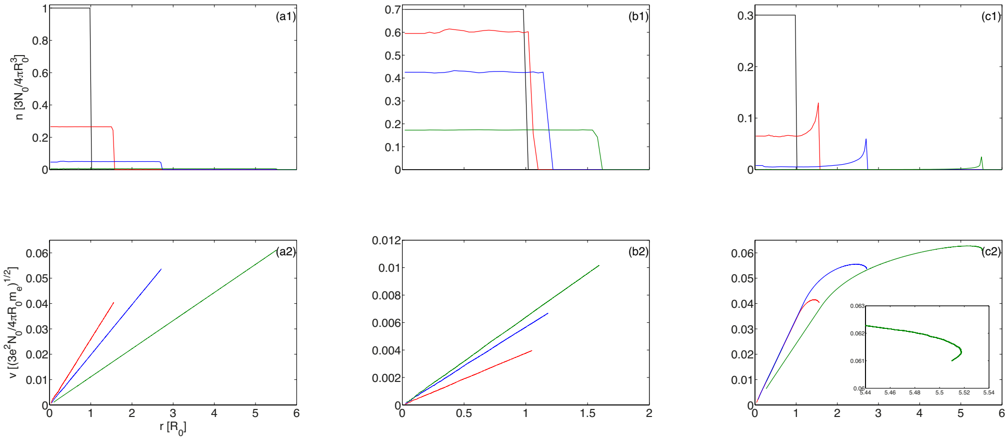

FIGURE 6.1: Ion density (1) and phase space (2) due to the explosion of a pure ion sphere composed by H^+ (a) and by a mixture of C^+ (b) and H^+ (c) at $t = 0$ (black), 24 (red), 48 (blue), 96 $\sqrt{4\pi R_0^3 m_e/3e^2 N_0}$ (green). The insert in figure (c2) shows a detail of the light ions multi-flow occurring at the expansion front.

for more than 120000 time steps. Figures 6.1-6.3 show the explosion evolution. For comparison purposes, the evolution of the explosion of a pure Hydrogen sphere with the same radius R_0 and density n_0 is also reported. As in the single species case, at the initial time, Hydrogen and Carbon ions contribute to create a linear electric field responsible for the acceleration. Differences between homo-nuclear and hetero-nuclear cluster explosions emerge immediately after. In the pure Hydrogen case, ions expand radially under the influence of the field that is smaller at the center and stronger at the periphery, preventing the particles to pass each other. As a result, the density stays uniform during the whole process, the phase space appears always as a straight line and the energy spectrum is broad and shows a cutoff value of $\varepsilon_{CE} = 4/3\pi n_0 e^2 R_0^2$ for $t \to \infty$. When the cluster is composite, the linear electric field at $t = 0$ will accelerate the H^+ ions more, because of their smaller mass to charge ratio (compared to C^+ ions). Consequently, the lighter particles can overtake the heavier ones and propagate ahead of them. The radial electric field, that is linearly increasing inside the bulk sphere of the C^+ ions, decreases as $1/r^2$ outside. The faster light ions coming from the bulk reach the peripheral ones, that are much slower due to the decaying field, forming a thin shell. The heavy ions act as a Coulomb piston and accelerate the light ions in the shell to the same energy, giving rise to a quasi-monoenergetic spectrum. Moreover the H^+ phase space

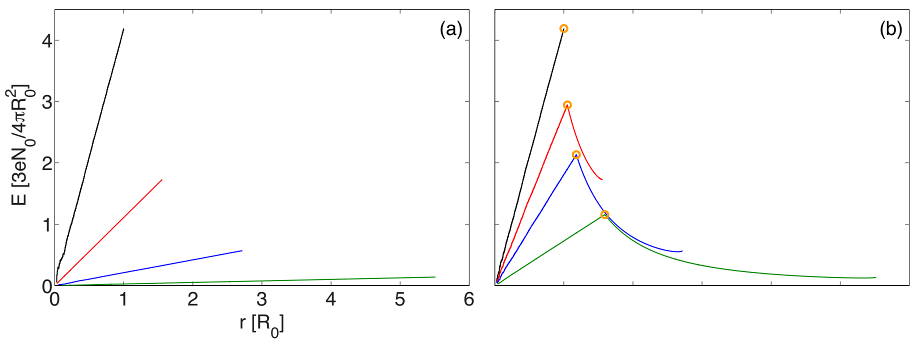

FIGURE 6.2: Radial electric field for the same cases as in figure 6.1. Figure (a) refers to the pure Hydrogen cluster explosion, while figure (b) refers to the composite clusters. The orange circles in (b) indicate the Carbon ion front.

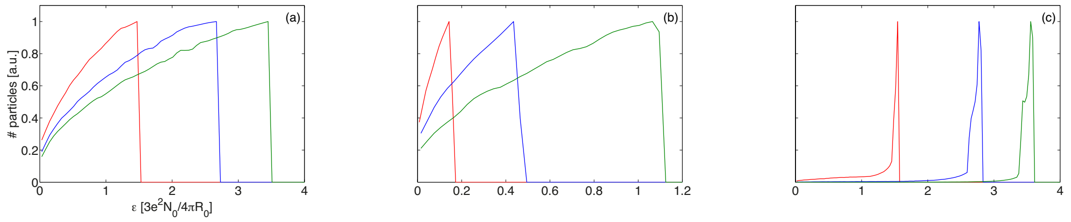

FIGURE 6.3: Hydrogen (a) and Carbon (b) and Hydrogen (c) energy spectrum evolution for the same cases of figure 6.1. Figures (b) and (c) refer to the composite cluster.

at late times shows a multi-flow of ions near the expansion front that is causing the peak in the density.

A parameter scan has been performed varying the fraction α of light ions inside the cluster. Results can be seen in figures 6.4 and 6.5. For small values of α, the phase space (figure 6.4 (b)) indicates that there is a multi-flow of Hydrogen ions. The size of the multi-flow decreases for increasing values of α and disappears for $\alpha > 0.3$. This is due to a reduction of the accelerating field with α (figure 6.4 (a)), that prevents the ions to overtake each other. A small decrease of the multi-flow benefits the ion energy spectrum (figure 6.4 (c)) that becomes narrower, being almost monochromatic for $\alpha = 0.3$. For $\alpha > 0.3$, the phase space becomes a single-flow and the energy spectrum gets wider. This can be seen also in figure 6.5 (a), where the energy spread versus α is reported at different times. Moreover, for $\alpha = 0.3$, almost all the H^+ ions (about 94%) have energy between $[\varepsilon_{avg} - \sigma, \varepsilon_{avg} + \sigma]$, where ε_{avg} is the average energy of

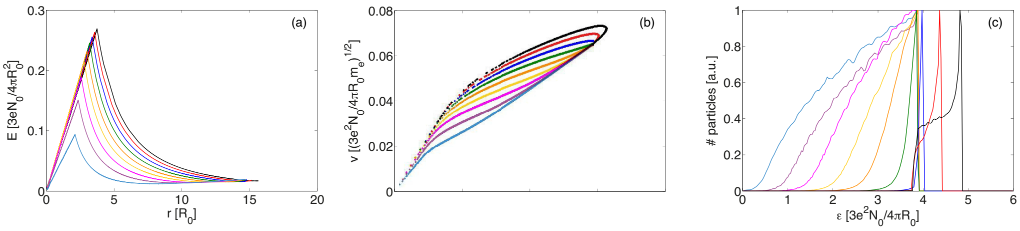

FIGURE 6.4: Radial electric field (a) and Hydrogen phase space (b) and energy spectrum (c) at $t = 240\sqrt{4\pi R_0^3 m_e/3e^2 N_0}$ due to the explosion of a cluster composed by C^+ and H^+. The different curves correspond to $\alpha = 0.1$ (black), 0.2 (red), 0.3 (blue), 0.4 (green), 0.5 (orange), 0.6 (yellow), 0.7 (magenta), 0.8 (violet) and 0.9 (light blue).

the particles and σ the standard deviation, this configuration being the one that maximizes the number of monochromatic ions (figure 6.5 (b)). Figures 6.5 (c) and (d) show the Hydrogen ions average and maximum energy versus α. The average energy is inversely proportional to α and it is bigger when the concentration of the light species is lower. The maximum energy (ε_{max}) decreases for small values of α until it reaches a plateau for $\alpha > 0.3$.

The influence of the Carbon ionization level (and therefore of the q/m ratio) on the dynamics of the explosion has also been studied. Results are shown in figures 6.6 and 6.7. As expected the best results are obtained when the ionization level of the heavy species is low and the q/m ratio between light and heavy ions is maximized.

6.1.2 ANALYTICAL MODEL

As numerical simulations showed, when the pure ion sphere is constituted by two species with different charge to mass ratio q/m and particles are uniformly distributed, they experience a different acceleration; in particular the species with a bigger q/m move faster and advance more with respect to the other, creating two concentric spherical regions, S_1 and S_2, with radius $R_1(t)$ and $R_2(t) \leq R_1(t)$ (see figure 6.8). The sphere S_2 contains a mix of light and heavy particles and $R_2(t)$ represents the frontline of the heavy ions. The spherical shell outside S_2 contains instead only light particles and R_1 is therefore the frontline of the light ions. Simulations also indicate that the electric field is

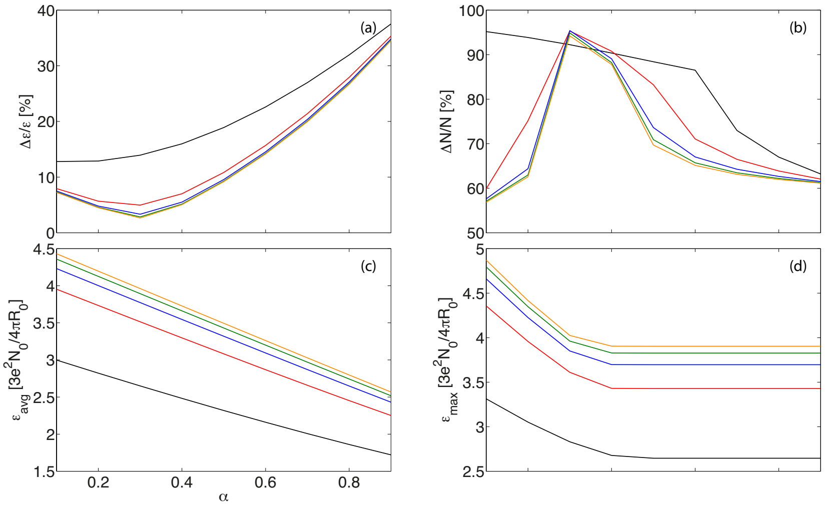

FIGURE 6.5: Energy spread (a), percentage of monoenergetic ions (ions with $\varepsilon \in [\varepsilon_{avg} - \sigma, \varepsilon_{avg} + \sigma]$) (b), average energy (c) and maximum energy (c) of Hydrogen ions versus α for the same clusters of figure 6.4. Here, the different colors correspond to $t = 48$ (black), 96 (red), 144 (blue) 192 (green) and 240 $\sqrt{4\pi R_0^3 m_e / 3e^2 N_0}$ (orange).

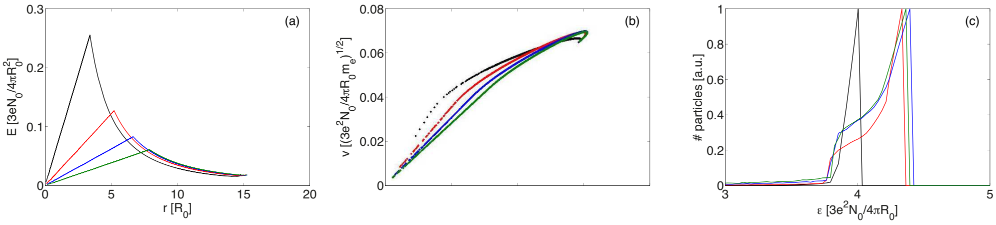

FIGURE 6.6: Radial electric field (a) and Hydrogen phase space (b) and energy spectrum (c) at $t = 240 \sqrt{4\pi R_0^3 m_e / 3e^2 N_0}$ due to the explosion of a heterogeneous cluster composed of 70% Carbon and 30% Hydrogen ions. The curves correspond to different levels of ionization of the Carbon ions: C^+ (black), C^{2+} (red), C^{3+} (blue) and C^{4+} (green).

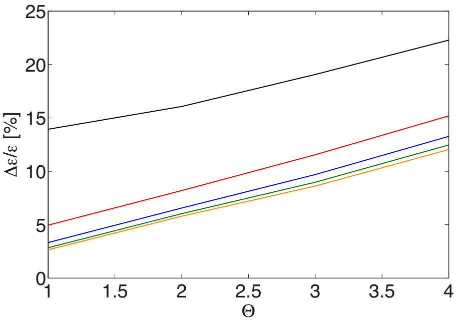

FIGURE 6.7: Hydrogen energy spread versus $\Theta = q_C/q_H$. The different colors correspond to $t = 48$ (black), 96 (red), 144 (blue) 192 (green) and 240 $\sqrt{4\pi R_0^3 m_e/3e^2 N_0}$ (orange).

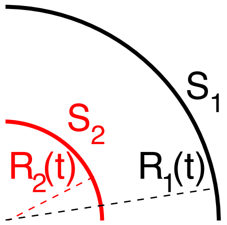

FIGURE 6.8: Concentric sphere of the heavy and light ions.

linear inside S_2 (figure 6.2):

$$E(r,t) = A(t)r \tag{6.1}$$

Using this assumption, the equation of motion for the light and the heavy ions inside S_2 can be written. Starting with the light ions, until they do not cross the frontline of the heavy ions (i.e. they are still in S_2), they obey to

$$m_1 \frac{\partial^2 r_1}{\partial t^2} = q_1 A(t) r_1 \tag{6.2}$$

where m_1 is the mass of a light ion, q_1 its charge and $r_1(t, r_0)$ the radial position at time t of a light ion with initial position r_0 ($r_1(0, r_0) = r_0$) and initial speed equal to zero ($\partial r_1(0, r_0)/\partial t = 0$). Introducing the dimensionless quantity $\xi(t) = r_1(t, r_0)/r_0$, the dependency on r_0 drops and equation 6.2 becomes

$$\frac{\mathrm{d}^2 \xi}{\mathrm{d}\, t^2} = \frac{q_1}{m_1} A(t) \xi \tag{6.3}$$

Eq. (6.3) is completed by the initial conditions:

$$\xi(t=0) = 1 \tag{6.4}$$

$$\frac{d\xi}{dt}(t=0) = 0 \tag{6.5}$$

The motion of the heavy ions is determined by

$$m_2 \frac{\partial^2 r_2}{\partial t^2} = q_2 A(t) r_2 \tag{6.6}$$

where m_2 is the mass of a heavy ion, q_2 its charge and $r_2(t, r_0)$ the radial psition at time t of a heavy ion with initial position r_0 ($r_2(0, r_0) = r_0$) and initial speed equal to zero ($\partial r_2(0, r_0)/\partial t = 0$). Introducing the dimensionless quantity $\eta(t) = r_2(t, r_0)/r_0$, as before, the dependency on r_0 drops and equation (6.6) becomes

$$\frac{d^2\eta}{dt^2} = \frac{q_2}{m_2} A(t)\eta \tag{6.7}$$

where the following initial conditions hold

$$\eta(t=0) = 1 \tag{6.8}$$

$$\frac{d\eta}{dt}(t=0) = 0 \tag{6.9}$$

A direct consequence of equation (6.7) is that

$$R_2(t) = \eta(t) R_0 \tag{6.10}$$

The term $A(t)$ is computed considering that the electric field at $r = R_2$, according to the Gauss law, is

$$E(R_2(t), t) = \frac{Q}{R_2(t)^2} \tag{6.11}$$

where $Q = Q_2 + Q_1$ is the total charge contained in S_2, being Q_2 the charge of the heavy ions that at $t = 0$ were contained in the sphere of radius R_0 and Q_1 the charge of the light ions that at time t are still in S_2

$$Q_2 = q_2 \frac{4\pi}{3} R_0^3 n_2(0) \tag{6.12}$$

$$Q_1 = q_1 \frac{4\pi}{3} r_0^3 n_1(0) \tag{6.13}$$

with r_0 defined as

$$r_0 = R_0 \frac{\eta}{\xi} \tag{6.14}$$

which ensures $r_1(t, r_0) \leq R_2(t)$. Plugging equations (6.12) and (6.13), into equation (6.11) and using equation (6.1), an expression for A can be found

$$A(t) = \frac{4\pi}{3} \left(\frac{q_1 n_1(0)}{\xi^3(t)} + \frac{q_2 n_2(0)}{\eta^3(t)} \right) \tag{6.15}$$

The trajectories of the light and heavy ions inside S_2 are then determined by solving the following system of equations

$$\begin{cases} \dfrac{\mathrm{d}^2\xi}{\mathrm{d}t^2} &= \dfrac{4\pi}{3} \dfrac{q_1}{m_1} \left(\dfrac{q_1 n_1(0)}{\xi^3(t)} + \dfrac{q_2 n_2(0)}{\eta^3(t)} \right) \xi \\ \\ \dfrac{\mathrm{d}^2\eta}{\mathrm{d}t^2} &= \dfrac{4\pi}{3} \dfrac{q_2}{m_2} \left(\dfrac{q_1 n_1(0)}{\xi^3(t)} + \dfrac{q_2 n_2(0)}{\eta^3(t)} \right) \eta \end{cases} \tag{6.16}$$

Introducing the normalized units $\tau = t\omega_{pi,1}$ with $\omega_{pi,1} = \sqrt{4\pi q_1^2 n_1(0)/m_1}$, $\gamma = n_2(0)/n_1(0) = (1-\alpha)/\alpha$, $\beta = m_2/m_1$ and $\Theta = q_2/q_1$, system (6.16) becomes

$$\begin{cases} \dfrac{\mathrm{d}^2\xi}{\mathrm{d}\tau^2} &= \dfrac{1}{3} \left(\dfrac{1}{\xi^3(t)} + \Theta\gamma \dfrac{1}{\eta^3(t)} \right) \xi \\ \\ \dfrac{\mathrm{d}^2\eta}{\mathrm{d}t^2} &= \dfrac{1}{3} \dfrac{\Theta}{\beta} \left(\dfrac{1}{\xi^3(t)} + \Theta\gamma \dfrac{1}{\eta^3(t)} \right) \eta \end{cases} \tag{6.17}$$

The system of equations (6.16) describes the trajectory of a light ion until $t = t_c$, time at which it reaches and passes R_2, front line of the heavy ions. The exact instant can be computed numerically solving equation

$$r_1(t_c) = R_2(t_c) \tag{6.18}$$

Inserting the definitions previously used, equation (6.18) becomes

$$\frac{\eta(t_c)}{\xi(t_c)} = \frac{r_0}{R_0} \tag{6.19}$$

The electric field for $r = r_1 \geq R_2$ can be computed as

$$E(r \geq R_2) = \frac{Q}{r^2} \tag{6.20}$$

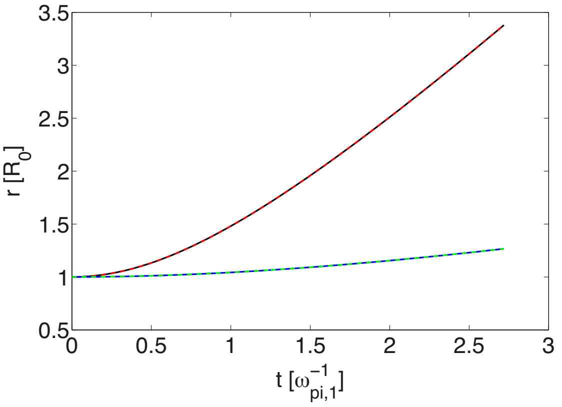

FIGURE 6.9: Frontline of the light (red dashed line) and heavy ions (green dashed line) versus time for a cluster composed by a mix of H^+ and C^+ ions with $\alpha = 0.3$, $\gamma = 2.3$, $\beta = 12$ and $\Theta = 1$. The initial radius of the cluster is $R_0 = 38\,\text{Å}$ and the Hydrogen density at $t = 0$ is $n_1 = 6 \times 10^{23}\,\text{cm}^{-3}$. Theoretical results have been compared with numerical ones (solid black line and solid blue line) obtained with the shell code.

where the quantity Q depends only on r_0 and is given by

$$Q(r_0) = \frac{4\pi}{3}\left(q_2 n_2(0) R_0^3 + q_1 n_1(0) r_0^3\right) \tag{6.21}$$

The equation of motion for a light ion outside S_2 is

$$\begin{cases} \dfrac{d^2 r}{dt^2} &= \dfrac{q_1}{m_1}\dfrac{Q(r_0)}{r^2} \\ r(t_c) &= \eta(t_c) R_0 \\ \dot{r}(t_c) &= r_0 \dot{\xi}(t_c) \end{cases} \tag{6.22}$$

Plugging equation (6.20) and (6.21) into (6.22) and introducing the dimensionless quantities τ, γ, Θ and $\hat{r} = r/R_0$, the system to solve becomes

$$\begin{cases} \dfrac{d^2 \hat{r}}{d\tau^2} &= \dfrac{1}{3}\dfrac{1}{\hat{r}^2}\left(\gamma\Theta + \hat{r}_0^3\right) \\ \hat{r}(\tau_c) &= \eta(\tau_c) \\ \dot{\hat{r}}(\tau_c) &= \hat{r}_0 \dot{\xi}(\tau_c) \end{cases} \tag{6.23}$$

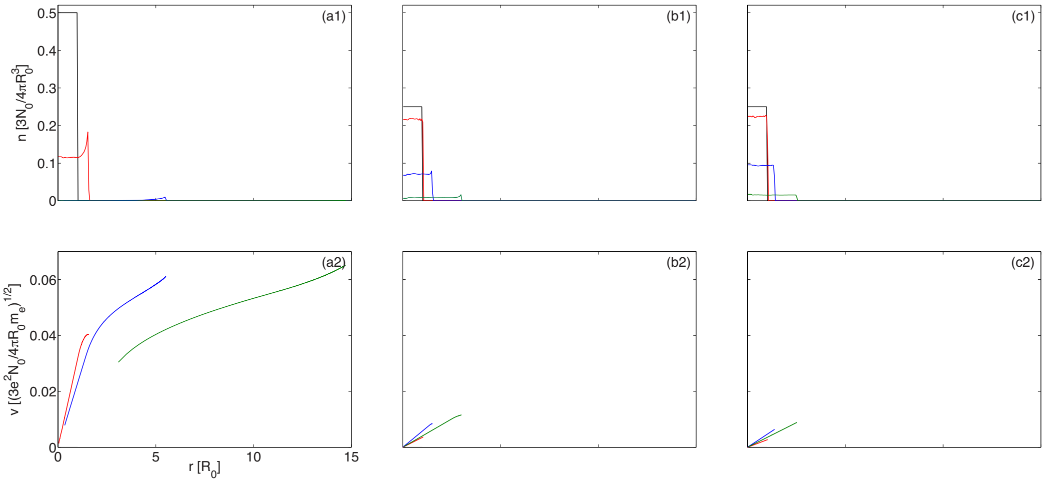

FIGURE 6.10: H^+ (a), C^+ (b) and O^+ (c) density (1) and phase space evolution (2) during Coulomb explosion of a cluster with $R_0 = 38$ Å and $N_0 \simeq 450000$. The different colors correspond to $t = 0$ (black), 24 (red), 96 (blue) and 240 $\sqrt{4\pi R_0^3 m_e/3e^2 N_0}$ (green).

Figure 6.9 shows the evolution of the frontline of the heavy and light ions for a cluster composed by a mix of H^+ and C^+, with $\alpha = 0.3$, $\gamma = 2.3$, $\beta = 12$ and $\Theta = 1$. The initial radius of the cluster is $R_0 = 38$ Å and the Hydrogen density at $t = 0$ is $n_1 = 6 \times 10^{23}\,\mathrm{cm}^{-3}$. Theoretical results have been compared with numerical ones obtained with the shell code, showing a perfect agreement.

Equation (6.22) can be rewritten as

$$m_1 \frac{\mathrm{d}^2 r}{\mathrm{d}t^2} = -\frac{\partial}{\partial r}\left(\frac{q_1 Q(r_0)}{r}\right) \tag{6.24}$$

and then integrated respect to t to compute the asymptotic kinetic energy of the light ions

$$\varepsilon_\infty = \frac{1}{2} m_1 \dot{r}^2(t_c) + \frac{q_1 Q(r_0)}{r(t_c)} \tag{6.25}$$

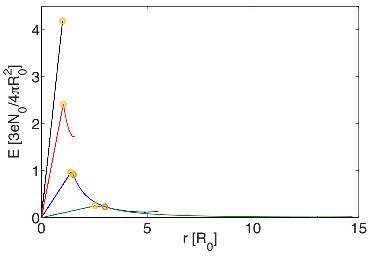

FIGURE 6.11: Electric field evolution for the same case of figure 6.10. The orange and yellow points indicate the Carbon and Oxygen ion fronts respectively.

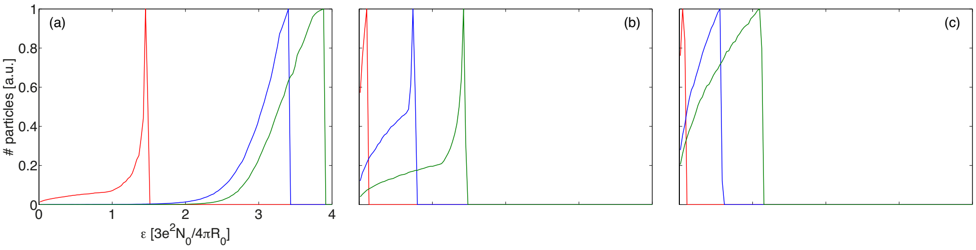

FIGURE 6.12: H^+ (a), C^+ (b) and O^+ (c) energy spectrum evolution for the same case of figure 6.10.

6.2 COULOMB EXPLOSION OF A CLUSTER COMPOSED BY THREE ION SPECIES

The explosion of multi-species clusters has also been modeled. A pure ion sphere of initial radius $R_0 = 38$ Å made of Hydrogen, Carbon and Oxygen (all ionized ones) has been considered. The cluster contains $N_0 \simeq 450000$ ions, distributed among the three species according to the following fractions: $1/2\, H^+$, $1/4\, C^+$ and $1/4\, O^+$. At $t = 0$ ions are at rest and uniformly distributed inside the sphere. A $\Delta t = 0.002\sqrt{4\pi R_0^3 m_e/3e^2 N_0}$ has been used and particles have been pushed for more than 120000 time steps. The evolution of the explosion can be seen in figures 6.10-6.12, where the density, the phase space, the electric field and the energy spectrum are reported. In the presence of three species with decreasing ratio q/m, the lightest and fastest ions overtake the heavier ones and propagate in front of them, gathering in a thin shell and giving rise to a quasi monoenergetic spectrum at early times, as in the case analyzed in section 6.1. At later times, also the Carbon ions, less massive than the Oxygen ones, overtake the latter, ending in a zone where the electric field is decreasing and getting therefore decelerated. As a result, the Carbon ions also gather together in a small shell, contributing to create a third spherical region between the positive ion bulk and the Hydrogen ion front. This region is characterized by an almost uniform electric field, that accelerates them to the same energy, producing quasi-monochromatic C^+ ions.

CHAPTER 7

N-BODY SIMULATIONS OF SHOCK SHELLS IN COULOMB EXPLOSION

During the Coulomb explosion of an ideal pure ion sphere, in the presence of a radial non-uniformity of the initial density profile, some of the ions can overtake the others, leading to the formation of shock shells [122], which are characterized by a multi valued phase space and by a peak in the density profile. Moreover, if the initial ion density has a suitable shape, a large fraction of the ions reaches the same radial position at the same time [123]. When this shock occurs, a finite amount of charge is compressed infinitely.

The density can be opportunely tailored, in order to obtain the desirable profile. This operation is done using a sequence of laser pulses with different intensities [124, 125]: a first relatively weak pulse hits the cluster, stripping off only a small number of electrons and inducing a slow hydrodynamics expansion, that causes the ion density to decrease at the periphery, while being almost constant in the core; at this point, a second extremely intense pulse reaches the cluster and sweeps away all the electrons, provoking the explosion of the pure ion bulk. When the outer ionization process is complete, the density of the ions is higher in the center than at the periphery, therefore the inner ions will feel a much higher repulsive force than the outer ones. Consequently, the inner ions will gain a higher velocity and will overtake the slower outer ions, leading to the formation of shock shells.

In the first part of this chapter collisionless theory and simulations about the formation of shock shells in Coulomb explosion will be introduced. Finally, a rigorous analysis of the Coulomb explosion dynamics is presented by using the N-body simulation method and the results will be compared.

7.1 THEORETICAL MODEL

The trajectory of each ion of a given distribution containing N_0 ions in 1D spherical geometry follows Newton's law

$$m\frac{\mathrm{d}^2 r}{\mathrm{d}t^2} = qE(r) \tag{7.1}$$

being m and q the ion mass and charge and E the radial electric field, that can be evaluated integrating Poisson's equation

$$\frac{1}{r^2}\frac{\mathrm{d}(r^2 E)}{\mathrm{d}r} = 4\pi q n(r) \tag{7.2}$$

where n is the ion density, leading to

$$E = \frac{qN(r)}{r^2} \tag{7.3}$$

with $N(r)$ defined as

$$N(r) = \int_0^r n(r')4\pi r'^2 \, dr' \tag{7.4}$$

Combining (7.1) and (7.3), the equation of motion becomes

$$m\frac{\mathrm{d}^2 r}{\mathrm{d}t^2} = q^2\frac{N(r)}{r^2} \tag{7.5}$$

Introducing the dimensionless quantities $\zeta = r/R_0$ and $\tau = t/t_0$, with R_0 initial radius of the cluster and $t_0 = \sqrt{mR_0^3/(q^2 N_0)}$, equation (7.5) becomes

$$\frac{\mathrm{d}^2\zeta}{\mathrm{d}\tau^2} = \frac{Q(\zeta)}{\zeta^2} \tag{7.6}$$

where $Q(\zeta) = N(\zeta)/N_0$ is the charge enveloped by the ion along its trajectory. Supposing that the ions do not overtake each other, the following property is verified

$$Q(\zeta(\zeta_0, \tau)) = Q(\zeta_0) \tag{7.7}$$

where $Q(\zeta_0)$ denotes the charge within a sphere of radius ζ_0 at $\tau = 0$. Using property (7.7) and multiplying both sides of the equation for $v = \mathrm{d}\zeta/\mathrm{d}\tau$, equation (7.6) can be solved analytically, leading to an expression for the particle velocity v

$$v(\zeta_0, \tau) = \sqrt{2Q_0(\zeta_0)\left(\frac{1}{\zeta_0} - \frac{1}{\zeta}\right)} \tag{7.8}$$

Integrating (7.8), an equation to compute ζ is retrieved

$$\mathscr{F}\left(\frac{\zeta}{\zeta_0}\right) = \sqrt{\frac{2Q_0(r_0)}{r_0^3}}\tau \tag{7.9}$$

where

$$\mathscr{F}\left(\frac{\zeta}{\zeta_0}\right) = \sqrt{\frac{\zeta}{\zeta_0}\left(\frac{\zeta}{\zeta_0} - 1\right)} + \log\left(\sqrt{\frac{\zeta}{\zeta_0}} + \sqrt{\frac{\zeta}{\zeta_0} - 1}\right) \tag{7.10}$$

A shock occurs when a set of ions reaches the position ζ_s at the same time τ_s; for this to happen, the initial charge density distribution in the interval $[\zeta_{0,1}\,\zeta_{0,2}]$ must have the particular form Q_0 defined by

$$Q_0(\zeta_0) = \frac{\zeta_0^3}{2\tau_s^2}\mathscr{F}^2\left(\frac{\zeta_s}{\zeta_0}\right) \tag{7.11}$$

The interval $[\zeta_{0,1}\,\zeta_{0,2}]$ is found requiring that the density profile is physically acceptable and that the no-overtaking assumption stays valid for $\tau < \tau_s$, i.e.,

$$\frac{\partial v}{\partial \zeta_0}(\zeta_{0,1}, \tau_s) \;=\; 0 \tag{7.12}$$

$$\frac{\mathrm{d}Q_0}{\mathrm{d}\zeta_0}(\zeta_{0,2}) \;=\; 0 \tag{7.13}$$

These conditions guarantee that, for $\zeta_0 < \zeta_{0,2}$, Q_0 is a monotonically growing function of ζ_0 and that before the shocks, ions do not overtake each other. Moreover, equations (7.12) and (7.13) yield $\zeta_{0,1} = 0.12\,\zeta_s$ and $\zeta_{0,2} = 0.61\,\zeta_s$ and, normalizing the maximum value of $Q_0(\zeta_0)$ to 1, the shock time is uniquely defined as $\tau_s = 0.59\,\zeta_s^{3/2}$. The charge profile for $\zeta_0 < \zeta_{0,1}$ can be chosen arbitrarily, provided that it matches $Q_0(\zeta_{0,1})$ and that it does not cause any ion to catch up with the ion started at $\zeta_{0,1}$ before τ_s; in the simulations a flat top density profile has been chosen.

7.2 KINETIC SIMULATIONS OF SHOCK SHELL FORMATION

The explosion of small clusters composed by $N_0 \simeq 1000$ ions with charge density profile described by equation (7.11) has been investigated using the shell algorithm, that, as seen in chapter 2, provides a reference solution of the Vlasov-Poisson model. Since the system is composed by a small number of particles, in order to smooth out the graininess of the plasma and reduce the collisionality, each particles has been split in $N_F \gg 1$ fragments with charge and mass respectively q/N_F and m/N_F. When the total number of fractional particles $N_p = N_0 \times N_F \to \infty$, the plasma collisionality vanishes, as the discrete charge density is transformed into a continuous distribution.

Moreover, for this particular study, ensemble averages have been calculated in order to take into account the different initial conditions of the system. For each simulation, at time t, any macroscopic quantity $\mathscr{P}$ of the system is a function of the number of computational particles N_p and of the initial conditions, i.e., $\mathscr{P}(t, N_p, \{\mathbf{x}_{i0}\}, \{\mathbf{v}_{i0}\})$. By considering the same number of computational particles N_p, but using a different set of pseudorandom numbers for the initial conditions $\{\mathbf{x}_{i0}^{\alpha}\}, \{\mathbf{v}_{i0}^{\alpha}\}$, a generally distinct solution, $\mathscr{P}_\alpha$, is obtained. Therefore, $\mathscr{P}$ is a random variable whose average, $\langle\mathscr{P}\rangle$, is the expected value of the physical quantity. Making use of the results of M different simulations, $\langle\mathscr{P}\rangle$ can be estimated as $\langle\mathscr{P}\rangle \simeq \overline{\mathscr{P}}$, being

$$\overline{\mathscr{P}} = \frac{1}{M} \sum_{\alpha=1}^{M} \mathscr{P}(t, N_p, \{\mathbf{x}_{i0}^{(\alpha)}\}, \{\mathbf{v}_{i0}^{(\alpha)}\}) \tag{7.14}$$

In fact, for a finite value for N_p, the ensemble averages obtained with $M \to +\infty$ does not represent the solution of the Vlasov equation but the results of the dynamics of a statistical ensemble of a physical system made of N_p point charges interacting as they were spherical shells. The solution of the Vlasov equation, $\mathscr{P}_{\mathrm{Vlasov}}$, can be obtained as the limit of $\overline{\mathscr{P}}(t)$:

$$\mathscr{P}_{\mathrm{Vlasov}}(t) = \lim_{N_p \to +\infty} \overline{\mathscr{P}}(t, N_p) \tag{7.15}$$

A Deuterium cluster composed by $N_0 = 1025$ ions and having initial radius $R_0 = 20$ Å has been considered. It has been supposed that a slow and controlled pre-expansion of the cluster creates the appropriate density profile in

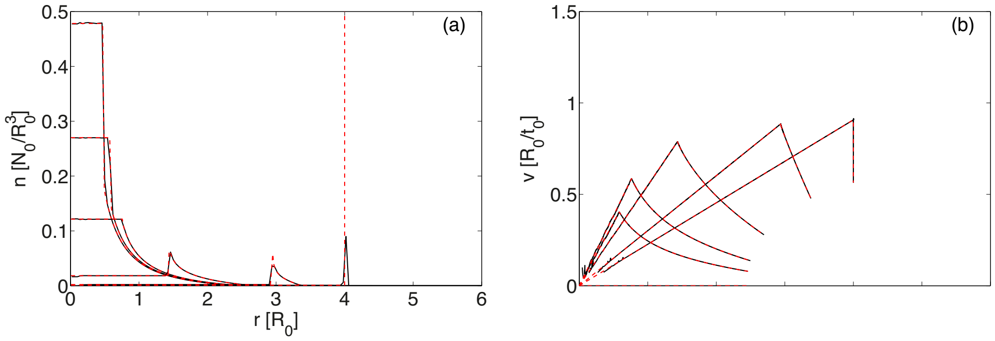

FIGURE 7.1: Ion density (a) and phase space (b) at $t = 0, 0.5, 0.8, 1.8, 3.5, 4.7\, t_0$ for a Deuterium cluster composed by $N_0 = 1025$ ions and having initial radius $R_0 = 20\,\text{Å}$. Shell model results (black solid lines) have been compared with theoretical ones (red dashed lines), showing a very good agreement.

such a way that $r_s = 4\, R_0$. The ions are initially at rest and distributed in space according to equation (7.11). Results are shown in figure 7.1. They represent the average over $M = 1000$ simulations with $N_p = 16000$ and $\Delta t = 0.002\, t_0$. At the beginning of the expansion, ions starting at $r_0 \in [0, r_{0,1}]$ feel a linearly increasing electric field, while outer ions with $r_0 > r_{0,1}$ perceive a decreasing field. The inner ions are then accelerated more than the latter, causing the particles to pile-up around $r = r_s$. When the ion trajectories cross, the density has a big increment in a small localized region and the phase space becomes multi valued. Shell model results have been compared with theoretical ones, given by equations (7.9) and (7.8) showing a very good agreement.

It is interesting to notice that numerical results obtained by using the shell technique do not change much when the number of computational particle N_p is decreased. The ion phase space at $t_s = 4.7\, t_0$ obtained running simulations with a different number of computational particles has been plotted in figure 7.2. All the curves, corresponding to different N_p, lie on top of each other and are practically indistinguishable, confirming that in the shell model the plasma collisionality is strongly reduced. Hence the shell algorithm turns out to be a tool suitable to study collisionless plasmas.

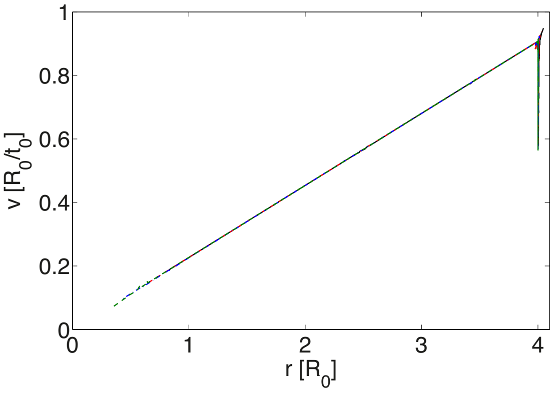

FIGURE 7.2: Ion phase space at $t_s = 4.7\, t_0$ for the same cluster of figure 7.1. Simulation results have been obtained with $N_p = 400$ (black), 800 (red), 2000 (blue) and 16000 (green) and are practically indistinguishable.

7.3 N-BODY SIMULATIONS OF SHOCK SHELL FORMATION

In sections 7.1 and 7.2 the phenomenon of shock shell formation during the Coulomb explosion of a pure ion plasma have been studied under the hypotheses that the collisionality was negligible and that kinetic theory was the suitable model to investigate the problem. However, looking carefully to the characteristics of the plasma, some questions about the accuracy of these assumptions may arise. This study focuses on nanoplasmas created during the interaction between intense laser pulses and small clusters composed by a relative small number of particles ($N_0 = 10^2 - 10^4$). Kinetic theory usually applies to systems with an extremely large set of particles; therefore one should wonder if a kinetic model is the tool to tackle this problem. Moreover, when these shocks occur, a finite amount of charge is highly compressed, causing a possible increment of the plasma collisionality. This is why a collisionless technique that solves the Vlasov-Poisson model might not be very accurate. For these reasons, the analytical solution obtained from expressions (7.9) and (7.8) has been compared with the results of numerical simulations based on the N-body method (see chapter 2), which provides the exact (numerical) solution for the Coulomb explosion. Ensemble averages have been computed in order to take into account the different initial conditions of the system. Ac-

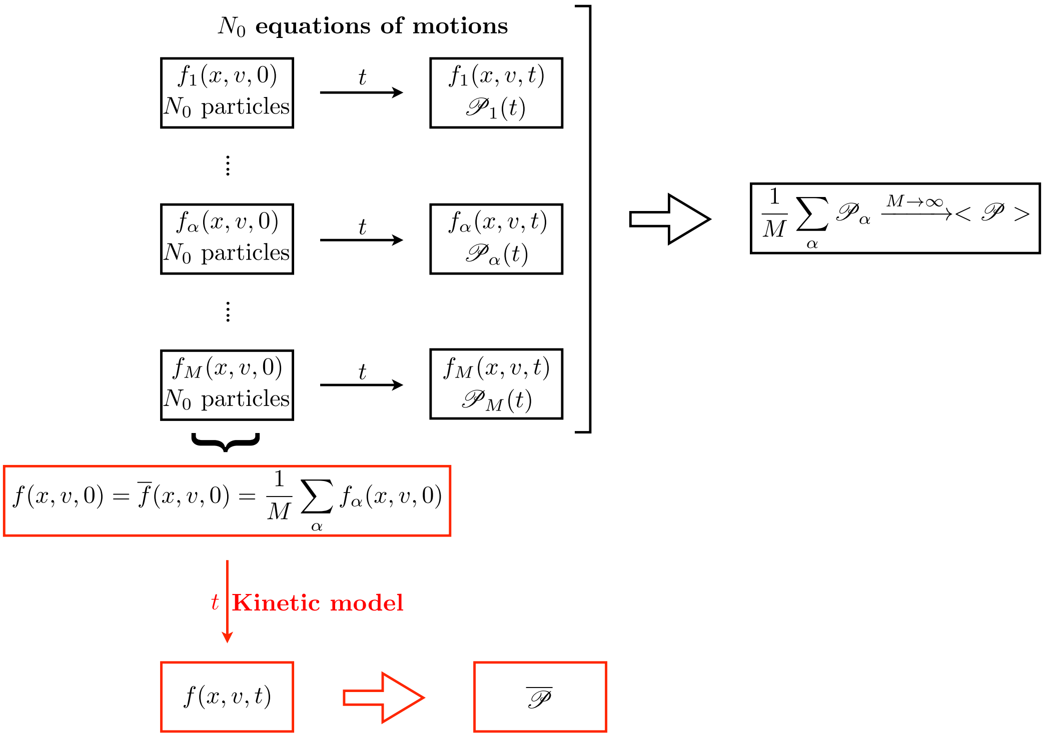
N_0 equations of motions
$f_1(x,v,0)$ N_0 particles
t
$f_1(x,v,t)$ $\mathscr{P}_1(t)$
$f_\alpha(x,v,0)$ N_0 particles
$f_\alpha(x,v,t)$ $\mathscr{P}_\alpha(t)$
$f_M(x,v,0)$ N_0 particles
$f_M(x,v,t)$ $\mathscr{P}_M(t)$
$\frac{1}{M}\sum_\alpha \mathscr{P}_\alpha \xrightarrow{M\to\infty} < \mathscr{P} >$
$f(x,v,0) = \overline{f}(x,v,0) = \frac{1}{M}\sum_\alpha f_\alpha(x,v,0)$
t Kinetic model
$f(x,v,t)$
$\overline{\mathscr{P}}$

FIGURE 7.3: Schematic description of the calculation of ensemble averages according to classical statistical mechanics. A generic macroscopic quantity calculated from the kinetic equation, $\overline{\mathscr{P}}$, and the corresponding value $\langle \mathscr{P} \rangle$, obtained as the average of the $\mathscr{P}_\alpha$ of every copy of the system.

cording to the classic treatment of the statistical mechanics, from the ensemble average (figure 7.3) one obtains the total distribution function to be used as initial condition for the kinetic model. If this model is correct, the value of every macroscopic quantity $\overline{\mathscr{P}}$ obtained by solving the kinetic equations and the corresponding ensemble-averaged $\langle \mathscr{P} \rangle$ should coincide at every time t.

The method shown in figure 7.3 has been tested for an ideal case: the Coulomb explosion of a spherical plasma with ions uniformly distributed. A pure Deuterium cluster with $R_0 = 20\,\text{Å}$ and $N_0 = 1025$ ions has been considered. At $t = 0$, ions are at rest and they start to expand due to the Coulomb forces. A time step of $\Delta t = 0.002\,t_0$ has been used. The ion density and the phase space at different times can be seen in figure 7.4. The results have been obtained averaging over $M = 2000$ N-body simulations and the mean values have been compared with shell code results, showing a good agreement. Figure 7.5 shows the phase space at $t = 1.2\,t_0$. Each red dot corresponds to an ion.

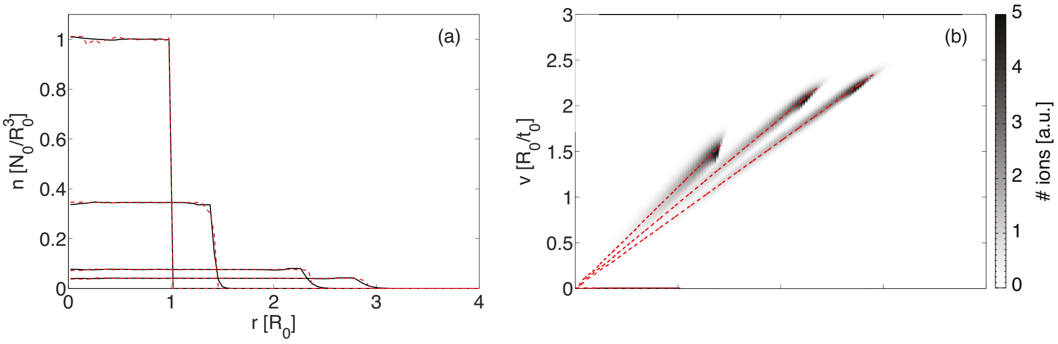

FIGURE 7.4: Ion density (a) and phase space (b) at $t = 0, 0.48, 0.96, 1.2\, t_0$ for a pure ion sphere, composed by $N_0 = 1025$ Deuterium ions and having raids $R_0 = 20$ Å. N-body simulation results (black) have been compared with shell model results (red, dashed).

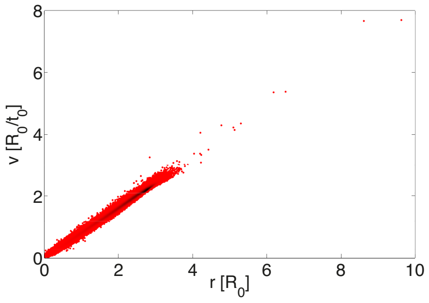

FIGURE 7.5: Ion phase space at $t = 1.2\, t_0$ for the same case of figure 7.4. Ensemble average (black line) and single calculations (red dots) are reported.

Particles from $M = 2000$ simulations are plotted along with the mean value in order to show the dispersion of the results. Figures 7.4 and 7.5 indicate that the collisionless kinetic model agrees with the exact solutions of the equation of motion, as far as mean values are considered, while in a single experiment the calculated value may differ significantly from the average. Therefore, the pure Coulomb explosion of a spherical plasma with ions uniformly distributed can be study by means of a collisionless kinetic model.

The same procedure has been used to investigate the formation of shock shells. A Deuterium cluster with the same properties of the one considered in section 7.2 has been studied ($N_0 = 1025$, $R_0 = 20$ Å, $r_s = 4\, R_0$ and density profile according to equation (7.11)). Results obtained averaging over 4000

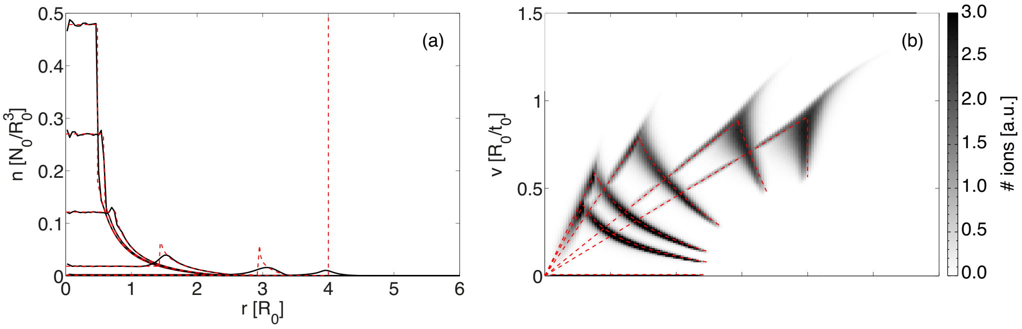

FIGURE 7.6: Ion density (a) and phase space (b) at $t = 0, 0.5, 0.8, 1.8, 3.5, 4.7\, t_0$ for the same Deuterium cluster of figure 7.1. N-body simulation results (in black) have been compared with theoretical ones (in red).

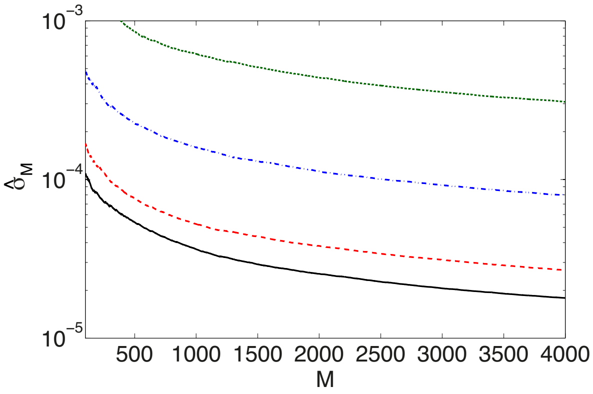

FIGURE 7.7: Standard deviation of the peak of the ion density for the same case of figure 7.6 for $t = 0.8$ (green dotted line), 1.8 (blue dash-dot line), 3.5 (red dashed line), $4.7\, t_0$ (black solid line).

simulations are shown in figure 7.6; in particular the ion density and phase space evolutions have been reported together with the collisionless analytical solution. Solutions start to differ already at early times. This can be attributed to the fact that the plasma is highly coupled: the plasma parameter ϵ_p (ratio between kinetic and potential energy) for this particular configuration tends to infinite and two body correlations can not be ignored. Direct interactions between particles cause them to diffuse preventing the shock formation. The statistical errors as function of M number of simulations are presented in figure 7.7.

CHAPTER 8

CONCLUSIONS

In the thesis, two different mechanisms to accelerate ions in laser-produced plasmas have been studied.

Numerical simulation tools, based on the particle technique, have been largely used. In particular, the state-of-the art particle in cell code Osiris, which is massively parallel, fully relativistic and object oriented, has been employed. A reduced electrostatic model, called the shell model, has been developed. Despite its simplicity, the technique has proved to be accurate in capturing the physics involved in collisionless electrostatic phenomena and to provide reduced computational times. Finally, an algorithm to carry out N-body simulations has been implemented. The technique allows for analyzing the exact (numerically speaking) dynamics of a plasma, because it does not contain any approximations. However, since it is computationally expensive, it has been applied only to small systems containing a little number of particles.

The first part of the thesis has been devoted to study the process of shock wave acceleration. Shock waves generated in plasmas can act as reflecting moving walls, picking up ions at rest and accelerating them to high velocities. It has been shown analytically and with numerical simulations that such electrostatic shocks can be generated by the interaction of two plasma regions with different temperatures and densities. A kinetic theoretical model that includes relativistic electron temperatures and a population of reflected ions has been developed. It exploits the Sagdeev formalism and it allows to identify the conditions for shock formation and ion reflection. It shows that, in order to accelerate ions in low Mach number shocks, easier to drive in laboratory, large density and low temperature ratios are favorable conditions. In order to increase the final ion energy that depends on the shock Mach number and on the ion sound speed $c_s \propto \sqrt{T_e}$, with T_e electron temperature, it is then necessary to maximize the electron heating. The theoretical predictions have been confirmed by numerical simulations carried out with Osiris and the shell model. An idealized scenario where the shock raised from the interpenetration of semi-infinite plasma slabs with different initial electron temperatures and densities has been simulated. Results indicate that the percentage of reflected ions increases with the density ratio. The presence of a relative drift between the two plasma regions has also been examined; an increase in v_d leads to an increment in the energy and in the number of reflected ions. Moving towards more realistic scenarios, finite plasma slabs have been considered. In this case, it has been seen that a TNSA field develops at the plasma-vacuum transition. The field is responsible to broaden the energy spectrum of the shock accelerated ions. It has been shown that this charge separation field can be controlled if the transition between plasma and vacuum is smooth. This is why tailored plasmas have been considered. The abrupt plasma-vacuum transition has been substituted with an exponentially decreasing density profile. In this case the charge separation field is almost constant and does not degrade the quality of the accelerated beam. An optimal decaying length has been derived theoretically and confirmed by a parameter scan over a wide range of values. A different approach has been proposed and tested: it consists in the use of several plasma slabs with progressively decreasing density to reproduce the exponential density profile. Simulation results indicate that multilayer plasmas can be a promising alternative to achieve a high quality ion beam. Moreover, it has been shown that the conditions necessary to drive a strong shock (i.e. a density discontinuity or a drift inside the plasma) can be achieved in laboratory by the interaction of a laser pulse with a near critical density tailored plasma. The laser is absorbed at the critical density, leading to a density steepening and to a strong electron heating. The fast electrons propagate through the target, setting up a return current that drags cold electrons towards the laser region. This causes a homogeneous electron heating all over the target. Some of the electrons leave the target at the back, creating a small and constant charge separation field that accelerates them to a uniform velocity. The small drift, the density jump and the intense electron heating contribute in launching a strong electrostatic collisionless shock wave that reflects the background ions leading to the generation of a high energy and high quality ion beam. Theoretical predictions about the scale length of the plasma profile has been confirmed also in laser-driven shock scenarios. Finally, scaling laws regarding the electron temperature and the ion energy have been retrieved for the ideal case of a plane wave laser and for the realistic case of a finite laser spot size.

In the second part of this work, the problem of ion acceleration in the Coulomb explosion of pure ion nanoplasmas has been investigated. A study of the explosion dynamics of multi-species spherical plasmas, that can be produced via the interaction between intense laser pulses and cluster targets, has been reported. Numerical simulations showed that in heavy-light systems, composed of two different ion species, the lighter ions get accelerated in a quasi-monoenergetic way (energy spread is less than 5%). It has been shown that the phase space of the lighter species can exhibit multi-flows whose role in determining the monochromaticity of the beam has been addressed. A parameter scan has been conducted where the relative percentage between heavy and light ions and the ionization level of the heavier species have been varied. An optimal light ion concentration leading to low energy spread and high ion charge in the beam has been determined. Moreover, a theoretical model, useful for a deep comprehension of the explosion dynamics, has been derived and solutions have been compared with numerical ones, showing a perfect agreement. Finally a study on shock shell formation during Coulomb explosion is presented. Shock shells may arise in the presence of radial non-unoformities of the initial ion density; in this case, since the electric field is no longer a monotonic function of the radius, ions from the center can experience a bigger acceleration than the ones at the periphery and overtake them. A particular kind of shock shells, that are driven by a peculiar initial density profile, has been investigated. According to the collisionless kinetic theory, when these shocks occur, a large fraction of the ions reaches the same radial position at the same time. A rigorous analysis on system composed by a small number of ions has been carried out with the N-body simulation technique, which is free from any assumption, thus providing insights on the real dynamics of the explosion. In this case, ensemble averages of the quantities of interest have been computed in order to take into account the different initial conditions of the system. They have been compared with reference solutions of the Vlasov-Poisson model, pointing out that the two approaches lead to different results. In particular, N-body simulations show that direct interactions between particles, that are not considered by the kinetic model, cause them to repulse each other and diffuse, preventing the shock formation.

BIBLIOGRAPHY

[1] V. Malka, J. Faure, Y. A. Gauduel, E. Lefebvre, A. Rousse, and K. T. Phuoc, "Principles and applications of compact laser-plasma accelerators," *Nature Physics*, vol. 4, p. 447, 2008.

[2] H. Daido, M. Nishiuchi, and A. S. Pirozhkov, "Review of laser-driven ion sources and their applications," *Reports on Progress in Physics*, vol. 75, p. 056401, 2012.

[3] S. C. Wilks, A. B. Langdon, T. E. Cowan, M. Roth, M. Singh, S. Hatchett, M. H. Key, D. Pennington, A. MacKinnon, and R. A. Snavely, "Energetic proton generation in ultra-intense laser-solid interactions," *Physics of Plasmas*, vol. 8, p. 542, 2001.

[4] R. A. Snavely, M. H. Key, S. P. Hatchett, T. E. Cowan, M. Roth, T. W. Phillips, M. A. Stoyer, E. A. Henry, T. C. Sangster, M. S. Singh, S. C. Wilks, A. MacKinnon, A. Offenberger, D. M. Pennington, K. Yasuike, A. B. Langdon, B. F. Lasinski, J. Johnson, M. D. Perry, and E. M. Campbell, "Intense high-energy proton beams from petawatt-laser irradiation of solids," *Physical Review Letters*, vol. 85, p. 2945, 2000.

[5] J. Fuchs, Y. Sentoku, S. Karsch, J. Cobble, P. Audebert, A. Kemp, A. Nikroo, P. Antici, E. Brambrink, A. Blazevic, E. M. Campbell, J. C. Fernández, J. C. Gauthier, M. Geissel, M. Hegelich, H. Pépin, H. Popescu, N. Renard-LeGalloudec, M. Roth, J. Schreiber, R. Stephens, and T. E. Cowan, "Comparison of laser ion acceleration from the front and rear surfaces of thin foils," *Physical Review Letters*, vol. 94, p. 045004, 2005.

[6] A. Macchi, F. Cattani, T. V. Liseykina, and F. Cornolti, "Laser acceleration of ion bunches at the front surface of overdense plasmas," *Physical Review Letters*, vol. 94, p. 165003, 2005.

[7] A. Macchi, M. Borghesi, and M. Passoni, "Ion acceleration by superintense laser-plasma interaction," *Reviews of Modern Physics*, vol. 85, p. 751, 2013.

[8] T. Esirkepov, M. Borghesi, S. V. Bulanov, G. Mourou, and T. Tajima, "Highly efficient relativistic-ion generation in the laser-piston regime," *Physical Review Letters*, vol. 92, p. 175003, 2004.

[9] A. Macchi, S. Veghini, T. V. Liseykina, and F. Pegoraro, "Radiation pressure acceleration of ultrathin foils," *New Journal of Physics*, vol. 12, p. 045013, 2010.

[10] W. L. Kruer and K. Estabrook, "heating by very intense laser light," *Physics of Fluids*, vol. 28, p. 430, 1985.

[11] O. Klimo, J. Psikal, J. Limpouch, and V. T. Tikhonchuk, "Monoenergetic ion beams from ultra thin foils irradiated by ultrahigh-contrast circularly polarized laser pulses," *Physical Review Special Topics - Accelerators and Beams*, vol. 11, p. 031301, 2008.

[12] A. Macchi, S. Veghini, and F. Pegoraro, ""light sail" acceleration reexamined," *Physical Review Letters*, vol. 103, p. 085003, 2009.

[13] L. Yin, B. J. Albright, B. M. Hegelich, K. J. Bowers, K. A. Flippo, T. J. T. Kwan, and J. C. Fernández, "Monoenergetic and gev ion acceleration from the laser breakout afterburner using ultrathin targetsa)," *Physics of Plasmas*, vol. 14, p. 056706, 2007.

[14] O. Buneman, "Dissipation of currents in ionized media," *Physical Review*, vol. 115, p. 503, 1959.

[15] B. J. Albright, L. Yin, K. J. Bowers, B. M. Hegelich, K. A. Flippo, T. J. T. Kwan, and J. Fernández, "Relativistic buneman instability in the laser breakout afterburner," *Physics of Plasmas*, vol. 14, p. 094502, 2007.

[16] M. S. F., R. A. Fonseca, L. O. Silva, and W. B. Mori, "Ion dynamics and acceleration in relativistic shocks," *The Astrophysical Journal Letters*, vol. 695, p. L189, 2009.

[17] D. Tidman and N. Krall, *Shock waves in collisionless plasmas*. Wiley-Interscience, New York, 1971.

[18] J. Denavit, "Absorption of high-intensity subpicosecond lasers on solid density targets," *Physical Review Letters*, vol. 69, p. 3052, 1992.

[19] L. O. Silva, M. Marti, J. R. Davies, R. A. Fonseca, C. Ren, F. S. Tsung, and W. B. Mori, "Proton shock acceleration in laser-plasma interactions," *Physical Review Letters*, vol. 1, p. 015002, 2004.

[20] D. Haberberger, S. Tochitsky, F. Fiuza, C. Gong, R. A. Fonseca, L. O. Silva, W. B. Mori, and C. Joshi, "Collisionless shocks in laser-produced plasma generate monoenergetic high-energy proton beams," *Nature Physics*, vol. 8, p. 95, 2012.

[21] G. Sorasio, M. Marti, R. A. Fonseca, and L. O. Silva, "Very High Mach-Number Electrostatic Shocks in Collisionless Plasmas," *Physical Review Letters*, vol. 96, p. 045005, 2006.

[22] I. Last, I. Schek, and J. Jortner, "Energetics and dynamics of Coulomb explosion of highly charged clusters," *The Journal of Chemical Physics*, vol. 107, no. 17, p. 6685, 1997.

[23] T. Ditmire, J. Zweiback, V. P. Yanovsky, T. E. Cowan, G. Hays, and K. B. Wharton, "Nuclear fusion from explosions of femtosecond laser–heated deuterium clusters," *Nature*, vol. 398, p. 489, 1999.

[24] R. Neutze, R. Wouts, D. van der Spoel, E. Weckert, and J. Hajdu, "Potential for biomolecular imaging with femtosecond x-ray pulses," *Nature*, vol. 406, no. 6797, p. 752, 2000.

[25] B. Iwan, *Creating and Probing Extreme States of Materials: From Gases and Clusters to Biosamples and Solids*. PhD thesis, Acta Universitatis Upsaliensis, Uppsala, 2012.

[26] J. Zweiback, R. A. Smith, T. E. Cowan, G. Hays, K. B. Wharton, V. P. Yanovsky, and T. Ditmire, "Nuclear fusion driven by Coulomb explosions of large deuterium clusters," *Physical Review Letters*, vol. 84, p. 2634, 2000.

[27] F. Peano, *Laser-induced Coulomb explosion of large deuterium clusters*. PhD thesis, Politecnico di Torino, Turin, 2005.

[28] A. McPherson, B. D. Thompson, A. B. Borisov, K. Boyer, and C. K. Rhodes, "Multiphoton-induced x-ray emission at 4-5 kev from xe atoms with multiple core vacancies," *Nature*, vol. 370, no. 6491, p. 631, 1994.

[29] T. Ditmire, T. Donnelly, R. W. Falcone, and M. D. Perry, "Strong x-ray emission from high-temperature plasmas produced by intense irradiation of clusters," *Physical Review Letters*, vol. 75, p. 3122, 1995.

[30] T. Ditmire, T. Donnelly, A. M. Rubenchik, R. W. Falcone, and M. D. Perry, "Interaction of intense laser pulses with atomic clusters," *Physical Review A*, vol. 53, p. 3379, 1996.

[31] Y. L. Shao, T. Ditmire, J. W. G. Tisch, E. Springate, J. P. Marangos, and M. H. R. Hutchinson, "Multi-kev electron generation in the interaction of intense laser pulses with Xe clusters," *Physical Review Letters*, vol. 77, p. 3343, 1996.

[32] L. M. Chen, J. J. Park, K.-H. Hong, J. L. Kim, J. Zhang, and C. H. Nam, "Emission of a hot electron jet from intense femtosecond laser-cluster interactions," *Physical Review E*, vol. 66, p. 025402, 2002.

[33] E. Springate, N. Hay, J. W. G. Tisch, M. B. Mason, T. Ditmire, M. H. R. Hutchinson, and J. P. Marangos, "Explosion of atomic clusters irradiated by high-intensity laser pulses: scaling of ion energies with cluster and laser parameters," *Physical Review A*, vol. 61, p. 063201, 2000.

[34] F. H. Attix, *Introduction to radiological physics and radiation dosimetry*. Wiley-VCH, 2004.

[35] "Particle accelerators take up the fight against cancer." `http://cerncourier.com/cws/article/cern/29777`.

[36] A. M. Koehler, "Proton radiography," *Science*, vol. 160, p. 303, 1968.

[37] M. Borghesi, A. J. Mackinnon, D. H. Campbell, D. G. Hicks, S. Kar, P. K. Patel, D. Price, L. Romagnani, A. Schiavi, and O. Willi, "Multi-MeV proton source investigations in ultraintense laser-foil interactions," *Physical Review Letters*, vol. 92, p. 055003, 2004.

[38] M. Borghesi, D. H. Campbell, A. Schiavi, M. G. Haines, O. Willi, A. J. MacKinnon, P. Patel, L. A. Gizzi, M. Galimberti, R. J. Clarke, F. Pegoraro,

H. Ruhl, and S. Bulanov, “Electric field detection in laser-plasma interaction experiments via the proton imaging technique,” *Physics of Plasmas*, vol. 9, p. 2214, 2002.

[39] A. J. Mackinnon, P. K. Patel, R. P. Town, M. . J. Edwards, T. Phillips, S. C. Lerner, D. W. Price, D. Hicks, M. H. Key, S. Hatchett, S. C. Wilks, M. Borghesi, L. Romagnani, S. Kar, T. Toncian, G. Pretzler, O. Willi, M. Koenig, E. Martinolli, S. Lepape, A. Benuzzi-Mounaix, P. Audebert, J. C. Gauthier, J. King, R. Snavely, R. R. Freeman, and T. Boehlly, “Proton radiography as an electromagnetic field and density perturbation diagnostic,” *Review of Scientific Instruments*, vol. 75, p. 3531, 2004.

[40] L. Romagnani, S. V. Bulanov, M. Borghesi, P. Audebert, J. C. Gauthier, K. Löwenbrück, A. J. Mackinnon, P. Patel, G. Pretzler, T. Toncian, and O. Willi, “Observation of collisionless shocks in laser-plasma experiments,” *Physical Review Letters*, vol. 101, p. 025004, 2008.

[41] G. Sarri, M. E. Dieckmann, C. R. D. Brown, C. A. Cecchetti, D. J. Hoarty, S. F. James, R. Jung, I. Kourakis, H. Schamel, O. Willi, and M. Borghesi, “Observation and characterization of laser-driven phase space electron holes,” *Physics of Plasmas*, vol. 17, p. 010701, 2010.

[42] G. Sarri, C. A. Cecchetti, L. Romagnani, C. M. Brown, D. J. Hoarty, S. James, J. Morton, M. E. Dieckmann, R. Jung, O. Willi, S. V. Bulanov, F. Pegoraro, and M. Borghesi, “The application of laser-driven proton beams to the radiography of intense laser-hohlraum interactions,” *New Journal of Physics*, vol. 12, p. 045006, 2010.

[43] M. Koenig, A. Benuzzi-Mounaix, A. Ravasio, T. Vinci, N. Ozaki, S. Lepape, D. Batani, G. Huser, T. Hall, D. Hicks, A. MacKinnon, P. Patel, H. S. Park, T. Boehly, M. Borghesi, S. Kar, and L. Romagnani, “Progress in the study of warm dense matter,” *Plasma Physics and Controlled Fusion*, vol. 47, p. B441, 2005.

[44] G. W. Collins, L. B. Da Silva, P. Celliers, D. M. Gold, M. E. Foord, R. J. Wallace, A. Ng, S. V. Weber, K. S. Budil, and R. Cauble, “Measurements of the equation of state of deuterium at the fluid insulator-metal transition,” *Science*, vol. 281, p. 1178, 1998.

[45] G. Huser, M. Koenig, A. Benuzzi-Mounaix, E. Henry, T. Vinci, B. Faral, M. Tomasini, B. Telaro, and D. Batani, “Temperature and melting of

laser-shocked iron releasing into an lif window," *Physics of Plasmas (1994-present)*, vol. 12, p. 060701, 2005.

[46] M. Koenig, A. Benuzzi, B. Faral, J. Krishnan, J. M. Boudenne, T. Jalinaud, C. Rémond, A. Decoster, D. Batani, D. Beretta, and T. A. Hall, "Brominated plastic equation of state measurements using laser driven shocks," *Applied Physics Letters*, vol. 72, p. 1033, 1998.

[47] R. W. Lee, S. J. Moon, H.-K. Chung, W. Rozmus, H. A. Baldis, G. Gregori, R. C. Cauble, O. L. Landen, J. S. Wark, A. Ng, S. J. Rose, C. L. Lewis, D. Riley, J.-C. Gauthier, and P. Audebert, "Finite temperature dense matter studies on next-generation light sources," *Journal of the Optical Society of America B*, vol. 20, p. 770, 2003.

[48] P. K. Patel, A. J. Mackinnon, M. H. Key, T. E. Cowan, M. E. Foord, M. Allen, D. F. Price, H. Ruhl, P. T. Springer, and R. Stephens, "Isochoric heating of solid-density matter with an ultrafast proton beam," *Physical Review Letters*, vol. 91, p. 125004, 2003.

[49] S. Atzeni and J. Meyer-ter-Vehn, *The physics of inertial fusion*. Oxford university press, 2004.

[50] M. Tabak, J. Hammer, M. E. Glinsky, W. L. Kruer, S. C. Wilks, J. Woodworth, E. M. Campbell, M. D. Perry, and R. J. Mason, "Ignition and high gain with ultrapowerful lasers," *Physics of Plasmas*, vol. 1, p. 1626, 1994.

[51] M. Roth, T. E. Cowan, M. H. Key, S. P. Hatchett, C. Brown, W. Fountain, J. Johnson, D. M. Pennington, R. A. Snavely, S. C. Wilks, K. Yasuike, H. Ruhl, F. Pegoraro, S. V. Bulanov, E. M. Campbell, M. D. Perry, and H. Powell, "Fast ignition by intense laser-accelerated proton beams," *Physical Review Letters*, vol. 86, p. 436, 2001.

[52] M. Temporal, J. J. Honrubia, and S. Atzeni, "Numerical study of fast ignition of ablatively imploded deuterium-tritium fusion capsules by ultra-intense proton beams," *Physics of Plasmas*, vol. 9, p. 3098, 2002.

[53] S. Atzeni, M. Temporal, and J. J. Honrubia, "A first analysis of fast ignition of precompressed icf fuel by laser-accelerated protons," *Nuclear Fusion*, vol. 42, p. L1, 2002.

[54] R. R. Wilson, "Radiological use of fast protons," *Radiology*, vol. 47, p. 487, 1946.

[55] J. H. Lawrence, “Proton irradiation of the pituitary,” *Cancer*, vol. 10, p. 795, 1957.

[56] S. V. Bulanov and V. S. Khoroshkov, “Feasibility of using laser ion accelerators in proton therapy,” *Plasma Physics Report*, vol. 28, p. 453, 2002.

[57] S. V. Bulanov, T. Z. Esirkepov, V. S. Khoroshkov, A. V. Kuznetsov, and F. Pegoraro, “Oncological hadrontherapy with laser ion accelerators,” *Physics Letters A*, vol. 299, p. 240, 2002.

[58] E. Fourkal, J. S. Li, W. Xiong, A. Nahum, and C.-M. Ma, “Intensity modulated radiation therapy using laser-accelerated protons: a Monte Carlo dosimetric study,” *Physics in Medicine and Biology*, vol. 48, p. 3977, 2003.

[59] V. Malka, S. Fritzler, E. Lefebvre, E. d,’Humières, R. Ferrand, G. Grillon, C. Albaret, S. Meyroneinc, J.-P. Chambaret, A. Antonetti, and D. Hulin, “Practicability of protontherapy using compact laser systems,” *Medical Physics*, vol. 31, p. 1587, 2004.

[60] P. Antici, M. Migliorati, A. Mostacci, L. Picardi, L. Palumbo, and C. Ronsivalle, “A compact post-acceleration scheme for laser-generated protons,” *Physics of Plasmas*, vol. 18, p. 073103, 2011.

[61] U. Linz and J. Alonso, “What will it take for laser driven proton accelerators to be applied to tumor therapy?,” *Physical Review ST Accelerators Beams*, vol. 10, p. 094801, 2007.

[62] S. Fritzler, V. Malka, G. Grillon, J.-P. Rousseau, F. Burgy, E. Lefebvre, E. d’Humieres, P. McKenna, and K. W. D. Ledingham, “Proton beams generated with high-intensity lasers: Applications to medical isotope production,” *Applied Physics Letters*, vol. 83, p. 3039, 2003.

[63] E. Lefebvre, E. d’Humières, S. Fritzler, and V. Malka, “Numerical simulation of isotope production for positron emission tomography with laser-accelerated ions,” *Journal of Applied Physics*, vol. 100, p. 113308, 2006.

[64] R. A. Fonseca, L. O. Silva, F. S. Tsung, V. K. Decyk, W. Lu, C. Ren, W. B. Mori, S. Deng, S. Lee, T. Katsouleas, and et al., “Osiris: a three-dimensional fully relativistic particle in cell code for modelling plasma based accelerators,” *Lecture Notes in Computer Science*, vol. 2331, p. 342, 2002.

[65] R. A. Fonseca, *Experimental and numerical study of laser-plasma electron accelerators*. PhD thesis, Instituto Superior Técnico, Lisbon, 2002.

[66] C. K. Birsdall and A. B. Langdon, *Plasma physics via computer simulation*. McGraw–Hill Book Company, 1985.

[67] R. Hockney and J. Eastwood, *Computer simulation using particles*. Taylor and Francis, 1988.

[68] J. M. Dawson, "Particle simulation of plasmas," *Reviews of Modern Physics*, vol. 55, p. 403, 1983.

[69] E. Boella, G. Coppa, A. D'Angola, F. Fiúza, and L. Silva, "Use of the shell model for plasma physics simulation." 64^{th} Gaseous Electronics Conference, Salt Lake City (Utah, USA), November 2011.

[70] A. D'Angola, E. Boella, and G. Coppa, "On the applicability of the collisionless kinetic theory to the study of nanoplasmas." Submitted to Physics of Plasmas, 2014.

[71] E. M. Lifshitz and L. P. Pitaevskii, *Physical kinetics*. Butterworth-Heinemann, 1998.

[72] J. Barnes and P. Hut, "A hierarchical O$(N \log N)$ force-calculation algorithm," *Nature*, vol. 324, p. 446, 1986.

[73] G. Lapenta, "Particle in cell methods with application to simulations in space weather," 2011. Katholieke Universiteit Leuven. Lecture notes.

[74] P. Gibbon, *Short pulse laser interactions with matter*. Imperial College Press, 2007.

[75] R. L. Morse and C. W. Nielson, "Numerical simulation of the Weibel instability in one and two dimensions," *The Physics of Fluids*, vol. 14, p. 830, 1971.

[76] "Open mpi: open source high performance computing." `http://www.open-mpi.org/`.

[77] "Hdf: Hierarchical data format." `http://www.hdfgroup.org/`.

[78] R. A. Fonseca, L. O. Silva, J. Tonge, R. G. Hemker, J. M. Dawson, and W. B. Mori, "Three-dimensional particle-in-cell simulations of the weibel instability in electron-positron plasmas," *Plasma Science, IEEE Transactions on*, vol. 30, p. 28, 2002.

[79] "Advanced simulation and computing." `https://asc.llnl.gov/`.

[80] "Top 500 supercomputer sites." `http://www.top500.org/`.

[81] J. Dawson, "One-dimensional plasma model," *The Physics of Fluids*, vol. 5, p. 445, 1962.

[82] O. Eldridge and M. Feix, "One-dimensional plasma model at thermodynamic equilibrium," *The Physics of Fluids*, vol. 5, p. 1076, 1962.

[83] J. Spanier and E. M. Gelbard, *Monte Carlo Principles and Neutron Transport Problems*. Dover Publications, Inc., 2008.

[84] F. F. Chen, *Introduction to plasma physics and controlled fusion*. Plenum Press, New York, 1984.

[85] R. Z. Sagdeev, *Review of plasma physics*, vol. 4. Consultans Bureau, 1966.

[86] D. W. Forslund and C. R. Shonk, "Formation and structure of electrostatic collisionless shocks," *Physycal Review Letters*, vol. 25, p. 1699, 1970.

[87] A. Stockem, E. Boella, F. Fiúza, and L. O. Silva, "Relativistic generalization of formation and ion-reflection condition in electrostatic shocks," *Physical Review E*, vol. 87, p. 043116, 2013.

[88] H. Schamel, "Stationary solitary, snoidal and sinusoidal ion acoustic waves," *Journal of Plasma Physics*, vol. 14, p. 905, 1972.

[89] D. Montgomery and G. Joyce, "Shock-like solutions of the electrostatic Vlasov equation," *Journal of Plasma Physics*, vol. 3, p. 1, 1969.

[90] M. Lazar, A. Stockem, and R. Schlickeiser, "Towards a relativistically correct characterization of counterstreaming plasmas. I. Distribution functions," *Open Plasma Physics Journal*, vol. 3, p. 138, 2010.

[91] J. E. Fahlen, "Exploring methods for producing relativistic protons and ions," Master's thesis, University of California, Los Angeles, 2005.

[92] R. Cairns, R. Bingham, P. Norreys, and R. Trines, "Laminar shocks in high power laser plasma interactions." private communication.

[93] H. Schamel, "Kinetic theory of phase space vortices and double layers," *Physica Scripta*, vol. 1982, p. 228, 1982.

[94] H. Schamel and S. Bujarbarua, "Analytical double layers," *Physics of Fluids*, vol. 26, p. 190, 1983.

[95] H. Schamel, "Electron holes, ion holes and double layers," *Physics Reports*, vol. 140, p. 161, 1986.

[96] F. Fiúza, A. Stockem, E. Boella, R. Fonseca, L. Silva, D. Haberberger, S. Tochitsky, C., W. Mori, and C. Joshi, "Ion acceleration from laser-driven electrostatic shocks," *Physics of Plasmas*, vol. 20, p. 056304, 2013.

[97] P. Mora, "Plasma expansion into a vacuum," *Physical Review Letters*, vol. 90, p. 185002, 2003.

[98] T. Grismayer and P. Mora, "Influence of a finite initial ion density gradient on plasma expansion into vacuum," *Physics of Plasmas*, vol. 13, p. 032103, 2006.

[99] F. Fiúza, A. Stockem, E. Boella, R. Fonseca, L. Silva, D. Haberberger, S. Tochitsky, C. Gong, W. Mori, and C. Joshi, "Laser-driven shock acceleration of mono-energetic ion beams," *Physical Review Letters*, vol. 109, p. 215001, 2012.

[100] A. Macchi, A. S. Nindrayog, and F. Pegoraro, "Solitary versus shock wave acceleration in laser-plasma interactions," *Physical Review E*, vol. 85, p. 046402, 2012.

[101] N. L. Tsintsadze, J. T. Mendonça, and L. O. Silva, "Propagation of relativistically intense laser pulses in nonuniform plasmas," *Physical Review E*, vol. 58, p. 4890, 1998.

[102] T. Nakamura, M. Tampo, R. Kodama, S. V. Bulanov, and M. Kando, "Interaction of high contrast laser pulse with foam-attached target," *Physics of Plasmas*, vol. 17, p. 113107, 2010.

[103] A. Sgattoni, P. Londrillo, A. Macchi, and M. Passoni, "Laser ion acceleration using solid target coupled with a low-density layer," *Physical Review E*, vol. 85, p. 036405, 2012.

[104] D. Haberberger, S. Tochitsky, and C. Joshi, "Fifteen terawatt picosecond CO_2 laser system," *Optics Express*, vol. 18, p. 17865, 2010.

[105] P. Kaw and J. Dawson, "Relativistic nonlinear propagation of laser beams in cold overdense plasmas," *Physics of Fluids*, vol. 13, p. 472, 1970.

[106] S. C. Wilks, "Simulations of ultraintense laser-plasma interactions," *Physics of Fluids B*, vol. 5, p. 2603, 1993.

[107] S. C. Wilks, W. L. Kruer, M. Tabak, and A. B. Langdon, "Absorption of Ultra-Intense Laser Pulses," *Physical Review Letters*, vol. 69, p. 1383, 1992.

[108] J. P. Freidberg, R. W. Mitchell, R. L. Morse, and L. I. Rudsinski, "Resonant absorption of laser light by plasma targets," *Physical Review Letters*, vol. 28, p. 795, 1972.

[109] F. Brunel, "Not-so-resonant, resonant absorption," *Physical Review Letters*, vol. 59, p. 52, 1987.

[110] R. L. Johnstonr, *Atomic and Molecular Clusters*. Taylor and Francis, 2002.

[111] M. Murakami and M. M. Basko, "Self-similar expansion of finite-size non-quasi-neutral plasmas into vacuum: Relation to the problem of ion acceleration," *Physics of Plasmas*, vol. 13, no. 1, p. 012105, 2006.

[112] N. Qi and M. Krishnan, "Experimental verification of a simple, one-dimensional model for the hydrodynamic expansion of a laser-produced plasma into vacuum," *Physics of Fluids B*, vol. 1, p. 1277, 1989.

[113] H. M. Milchberg, S. J. McNaught, and E. Parra, "Plasma hydrodynamics of the intense laser-cluster interaction," *Physical Review E*, vol. 64, p. 056402, 2001.

[114] T. Ditmire, E. Springate, J. W. G. Tisch, Y. L. Shao, M. B. Mason, N. Hay, J. P. Marangos, and M. H. R. Hutchinson, "Explosion of atomic clusters heated by high-intensity femtosecond laser pulses," *Physical Review A*, vol. 57, p. 369, 1998.

[115] F. Peano, J. L. Martins, R. A. Fonseca, F. Peinetti, R. Mulas, G. Coppa, I. Last, J. Jortner, and L. O. Silva, "Expansion of nanoplasmas and laser-driven nuclear fusion in single exploding clusters," *Plasma Physics and Controlled Fusion*, vol. 50, p. 124049, 2008.

[116] T. Ditmire, J. W. G. Tisch, E. Springate, M. B. Mason, N. Hay, R. A. Smith, J. Marangos, and M. H. R. Hutchinson, "High–energy ions produced in explosions of superheated atomic clusters," *Nature*, vol. 386, p. 54, 1997.

[117] J. C. H. Spence, U. Weierstall, and N. H. Chapman, "X-ray lasers for structural and dynamic biology," *Reports on Progress in Physics*, vol. 75, no. 10, p. 102601, 2012.

[118] H. Li, J. Liu, C. Wang, G. Ni, R. Li, and Z. Xu, "Coulomb explosion of hydrogen clusters irradiated by an ultrashort intense laser pulse," *Physical Review A*, vol. 74, p. 23201, 2006.

[119] V. P. Krainov and M. B. Smirnov, "Cluster beams in the super-intense femtosecond laser pulse," *Physics Reports*, vol. 370, p. 237, 2002.

[120] F. Peano, J. L. Martins, R. A. Fonseca, L. O. Silva, G. Coppa, F. Peinetti, and R. Mulas, "Dynamics and control of the expansion of finite-size plasmas produced in ultraintense laser-matter interactions," *Physics of Plasmas*, vol. 14, p. 056704, 2007.

[121] Y. Kishimoto, T. Masaki, and T. Tajima, "High energy ions and nuclear fusion in laser-cluster interaction," *Physics of Plasmas*, vol. 9, p. 589, 2002.

[122] A. E. Kaplan, B. Y. Dubetsky, and P. L. Shkolnikov, "Shock shells in Coulomb explosion of nanoclusters," *Physical Review Letters*, vol. 91, p. 143401, 2003.

[123] F. Peano, G. Coppa, and L. O. Silva, "Dimensional collapse in Coulomb explosions." 34^{th} European Physical Society, Conference on Plasma Physics, Warsaw (Poland), July 2007.

[124] F. Peano, R. Fonseca, and L. O. Silva, "Dynamics and control of shock shells in the Coulomb explosion of very large deuterium clusters," *Physical Review Letters*, vol. 94, p. 033401, 2005.

[125] F. Peano, R. A. Fonseca, J. L. Martins, and L. O. Silva, "Controlled shock shells and intracluster fusion reactions in the explosion of large clusters," *Physical Review A*, vol. 73, p. 053202, 2006.